Solar wind – influence on the magnetosphere and evolution to Earth

Doctoral thesis in physics

Malte S. Venzmer

University of Göttingen

Institute for Astrophysics

January 2012 – Jan? 2018

Supervisor:
Dr. Volker Bothmer

Referees:
Prof. Dr. Ansgar Reiners
Prof. ??

"Despite the 'Dr.' before his name, he had completed no course of study and received no degree. When people tried to pin him down about this, he would say that the letters were merely an abbreviation of his first name - Drummond - which he did not use. But it was as 'Dr.' Sam Laserowitz that he appeared in a number of science-fiction magazines; he was also known, in the circles of the fans of that genre, as a lecturer, and spoke on 'cosmic' themes at their many conferences and convention. Laserowitz's speciality was earthshaking discoveries, wich he happened upon two or three times a year. [...] We really have no idea what a multitude of con men and crackpots inhabit the domain that lies halfway between contemporary science and the insane asylum."

Excerpt from Stanisław Lem 1968, *His Master's Voice* (Lem & Kandel 1984, p. 38).

version log:
1 2013-11-06
2 2013-11-07 inserted lem excerpt
3 2014-09-01 outlined introduction structure and appendix key words
4 2014-09-11 bibtex included, lem excerpt citet
5 2014-09-12 included italic titles in bibliography
6 2015-01-12 worked on introduction structure and included magnetic butterfly diagram
7 2015-05-04 first printout, small additions
8 2015-07-03 coupling functions, content structure
9 2015-09-09 Alfvén wave velocity formula
10 2015-09-10 Appendix physics: Alfvén and compressional MHD waves, plasma beta; citation sources Cranmer2005, Kivelson1995
11 2015-09-15 CGAUSS work overview; DQCS model figure
12 2015-09-16 magnetic energy density is the same as magnetic pressure, abbreviations
13 2015-09-30 empirical solar-wind model plots in analyses, figure label [Figure 4.2 Text]
14 2015-10-02 table column decimal alignment; set caption width
15 2015-10-05 table units; radial parameter (N, T) profiles in literature
16 2015-10-06 literature radial electron density models; log-normal distribution
17 2015-10-07 log-normal formulae
18 2015-10-08 log-normal fit
19 2015-10-09 shape fit parameter table; radial variance fitting
20 2015-10-14 variance fit values; log-normal citation Bronstein
21 2015-10-19 radial distribution width fitting; clarifying of solar-wind model formulae structure and naming variables
22 2015-10-20 log-normal distribution width factor changes the shape!
23 2015-10-23 log-normal distributions mu and sigma plot
24 2015-10-30 new sigmafit2 figures implemented; formulae adaption
25 2015-11-02 reason for use of log-normal function
26 2015-11-20 single log-normal shape fit; not chisquare - SSR; R^2 in appendix
27 2015-11-26 reduced SSR into tables; table column aligning
28 2015-12-02 smoothing SSR integration
29 2015-12-07 integrating structure remarks from printout
30 2015-12-09 splitting analyses chapter into two; browsing folders for usable things for thesis
31 2015-12-10 integrating citations and references
32 2015-12-16 integrating citations and references
33 2015-12-18 solar-wind structures list of Richardson

34 2016-02-02 sws distributions
35 2016-02-11 basics structure
36 2016-02-12 analyses questions
37 2016-02-15 analyses structure; in situ, near-Sun
38 2016-02-16 Kp index internal resolution
39 2016-02-17 Bartels1962; non-breaking hyphen shorthand implemented
40 2016-02-18 analysesI structure
41 2016-02-25 abstract
42 2016-02-26 english comma
43 2016-03-01 Bartels Kp origin paper, bibtex reference
44 2016-03-02 abstract
45 2016-03-03 Planck paper
46 2016-03-07 formation of stars
47 2016-03-08 formation of stars
48 2016-03-16 solar interior structure
49 2016-03-17 solar interior structure
50 2016-03-18 solar surface
51 2016-03-22 Astronomical Almanac citation
52 2016-03-23 solar core definition
53 2016-03-26 sunspots
54 2016-03-29 Sun interior figure
55 2016-03-30 solar composition
56 2016-03-31 Sun interior figure finished; chromosphere
57 2016-04-01 Sun atmosphere figure finished
58 2016-04-03 chromosphere, corona, CV
59 2016-04-07 CV
60 2016-04-08 CV; heliosphere
61 2016-04-09 corona; heliosphere
62 2016-04-11 heliosheath magnetic bubbles; Opher2011
63 2016-04-12 heliosphere; voyagers; Gurnett2013
64 2016-04-13 solar-wind effects, solar rotation
65 2016-04-14 analysesI sws structure draft plots
66 2016-04-15 analysesI concept work
67 2016-04-19 incorporate annotations from processed printout
68 2016-04-21 incorporate annotations from processed printout II
69 2016-04-22 incorporate annotations from processed printout III
69 2016-04-23 updated .bst file (for displaying arXiv id); implemented optional url displaying for electronic version; Kp year variations
70 2016-04-24 Kp frequency by month statistics and plot; Sun and Earth tilt plot
71 2016-04-25 solar cycle extrema dates literature
72 2016-04-27 Kp semi annual variation, Rangarajan1997
73 2016-05-01 Kp frequency by year
74 2016-05-04 Kp + SSN plot; ACE data errors/gaps; log-normal plot; differential rotation plot
75 2016-05-05 aggregate correlation coefficient tables, CME fraction plot
76 2016-05-06 overall sws fractions
77 2016-05-17 figure sw frequencies by year; restructured solar-wind distributions section; formal cover page
78 2016-05-20 Earth-Sun distance; JPL web interface
79 2016-05-31 GSM system
80 2016-06-10 Offline Anmerkungen einarbeiten
81 2016-06-12 LaTeX Earth symbol package
82 2016-06-13 numbers=noenddot
83 2016-06-14 references removed comma before ampersand; offline Anmerkungen einarbeiten; thesis_raw version
84 2016-06-17 gnuplot figures and latex; latex document style options
85 2016-06-19 header implemented
86 2016-06-20 minor things; introduction
87 2016-06-23 solar tilt axis
88 2016-06-24 solar rotation
89 2016-07-12 magnetosphere temp figure; analyses: solar-wind model
90 2016-07-13 lognormal spelling

91 2016-07-14 constant mass flow rate
92 2016-07-18 line-up periods
93 2016-07-19 line-up periods table
94 2016-07-20 redone line-up analysis
95 2016-07-21 line-up tables
96 2016-07-22 line-up fit function plots; coefficient table
97 2016-07-22 line-up sw types and period plots; overview plot
98 2016-07-24 line-up averaging and justification
99 2016-07-29 line-up rework
100 2016-07-30 line-up structure
101 2016-07-31 line-up table
102 2016-08-02 line-up structure
103 2016-08-03 line-up fits and table
104 2016-08-04 insert offline comments
105 2016-08-15 literature radial sw functions
106 2016-08-18 work offline comments in
107 2016-08-19 work offline comments in
108 2016-08-28 analyses II rework structure
109 2016-08-31 analyses II rework structure
110 2016-09-01 analyses II rework figures
111 2016-09-02 analyses II rework structure
112 2016-09-03 Helios latitude dependency
113 2016-09-04 extrapolation model fit parameter table; Helios latitude dependence
114 2016-09-06 work in offline comments
115 2016-09-14 implement median and mean in composite fit table; create kile project for thesis; url and raw fork
116 2016-09-17 Ulysses polar plot; solar distance plots
117 2016-09-18 for solar distance and latitude -> 4-panel figures created and implemented; appendix figures
118 2016-09-20 latitude plots updated
119 2016-09-26 single lognormal fit figure
120 2016-09-27 minor tweaks in analyses II
121 2016-09-29 simple fit table errors; table style
122 2016-10-05 lognormal fit errors for tables
123 2016-10-10 line-up passing remarks from AP
124 2016-10-12 siunitx package incorporated
125 2017-01-04 package fancyhdr replaced with scrlayer-scrpage; offline comments for Basics + Data incorporated
126 2017-01-06 package floatrow included for figure side captions; some cites; magnetometer
127 2017-01-08 sun figure updates and new ion energy spectrum figure incorporated
128 2017-01-13 offline comments, new chapter order
129 2017-01-18 activated hyperref package; included autoref and eqref; adjusted link colors; header links
130 2017-02-02 offline commtents
131 2017-02-03 offline commtents II, eclipse image
132 2017-02-06 basics figures with floatrow; flow structure
133 2017-02-07 ion energy spectrum figure
134 2017-02-09 Helios mission ssn plot
135 2017-02-12 offline comments
136 2017-02-13 section number link to toc; offline comments
137 2017-02-14 eclipse and magbfly figure captions
138 2017-02-16 offline comments
139 2017-02-19 coronal heating and sw acceleration
140 2017-04-22 set up git repository
141 2017-04-23 incorporate offline comments
142 2017-04-26 bipolar region draft
143 2017-04-27 magnetic layer Ossendrijver2003
144 2017-06-29 magnetosphere figure drafts implemented
145 2017-07-16 streamlined content - including paper and chapter2
146 2017-07-22 streamlined duplicate content
147 2017-10-05 Kp index data
148 2017-10-28 geomagnetic indices; Kp index; Kp to ap table

149 2017-10-29 Kp index
150 2017-10-30 OMNI s/c coverage figure
151 2017-10-31 OMNI s/c coverage figure upgrade; data set timeline figure
152 2017-11-01 SSN prediction; omega-effect
153 2017-11-02 alpha-omega dynamo; magnetogram figure upgrade
154 2017-11-03 worked on figure permissions; alpha-omega-figure
155 2017-11-04 paperMVVB inserted; worked on compatibility
156 2017-11-12 paperMVVB: figure size, tablefoot, adjusted table width; included chapter2; ordered file implementing
157 2017-11-14 figure permission Babaszkiewicz1998
158 2017-11-15 poking around in image credits; solar activity cycle
159 2017-11-16 solar activity cycle; Zhao image permission
160 2017-11-17 Zhao copyright symbol included; solar-wind; commata and sentence wording
161 2017-11-22 notes from github paper folder
162 2017-11-23 Ulysses figure permission and caption; pdfpages package; paper included as is
163 2017-11-24 GUM reference; Helios data frequency figure
164 2017-11-25 intro to paper
165 2017-11-26 intro to paper
167 2017-11-27 Cranmer2005 fig1; Banaszkiewicz fig
168 2017-11-28 HCS and Parker spiral
169 2017-11-29 heliosheath; Cranmer2005 permission
170 2017-11-30 chapter2 updated
171 2017-12-06 upgraded: title, abstract, introduction, basics outline, notes to chapter2; worked in offline comments until HMF
172 2017-12-08 MBPs; Solar wind section structure
173 2017-12-10 solar wind basics, draft figs for CIR and CME
174 2017-12-11 draft figs for COR2 CME and ACE MC; solar wind history
175 2017-12-13 B-field improvement
176 2017-12-14 B-field improvement #2
177 2017-12-15 B-field improvement #3
178 2017-12-16 B-field angles plot

2017-12-16 14:03 – last save

Abstract

This thesis analyzes how strong the solar wind and its internal structures impact the terrestrial magnetosphere and how the solar wind evolves on its way from the Sun. In situ solar-wind measurements from the near-Earth OMNI data set are analyzed together with time series of the planetary geomagnetic disturbance indicator *Kp*. Correlation functions are compiled with regard to nowcast the magnitude of the geomagnetic disturbances from solar-wind measurements and to forecast them from remotely observed streams and CMEs. In situ data from the near-Earth OMNI data set and sunspot number data is used for deriving functional dependences with the state of the solar cycle for the solar-wind parameters magnetic field strength, proton velocity, density, and temperature. Data from the Helios 1 and 2 missions is analyzed and empirical solar-wind distance dependencies for 0.3–1.0 au are derived. Additionally, in view of the planned near-Sun spacecraft mission Parker Solar Probe (PSP), the solar-wind environment is estimated down to <10 solar radii.

catch from chapter abstracts...

Contents

1 Introduction

Introductory text -> motivation
- *Kp* impact analysis
- solar activity analysis
- distance analysis

thesis goal: finding more precise relationships between parameters/quantities for being able to make better forecasts

This thesis merges the solar-wind analyses of its impact on the magnetosphere, its variation with solar activity, and its evolution to Earth. This work is structured as follows. In chapter 2 the fundamentals about the Sun, its activity, solar wind, and space weather are laid. The instruments and data are described in chapter 3. The influences on the *Kp* index from solar activity, solar wind, its streams, and CMEs are analyzed in autorefchap:chapter2. In chapter 6, which includes the published paper on the same topic (chapter 7), an empirical solar-wind model for the inner heliosphere is developed and used to estimate the near-Sun solar-wind environment for the planned PSP mission. chapter 9 summarizes the results and gives an outlook for further studies. Useful equations, constants, and abbreviations are located in the Appendix A, B, and C.

2 Basics

This chapter sketches the basics for the analyses performed in this work. First, the Sun's origin, inner structure, atmosphere and heliosphere are described. Then, the Sun's dynamics with its differential rotation and magnetic field generation are outlined. Further, the solar activity cycle is described, including the meridional flow circulation, appearance of active regions, the surface magnetic field change, and sunspot cycles. The heliospheric magnetic field is pictured from its photospheric emergence in magnetic bright points and coronal superradial expansion, through the formation of the heliospheric current sheet and the Parker spiral to the heliosheath. The solar wind and its properties, the origin of slow and fast streams, stream interaction regions, and coronal mass ejections are described. Furthermore, the space weather, the solar influence on Earth, the magnetosphere, solar wind-magnetosphere coupling, and geomagnetic indices are portrayed.

2.1 Solar composition

13.8 billion years ago the Big Bang formed our universe. The energy density of our universe consists of 69.1 % dark energy, 25.9 % dark matter and 4.9 % baryonic matter, according to calculations using the inflationary ΛCDM cosmology together with the latest CMB temperature measurements (Planck Collaboration et al. 2016). After a few minutes the primordial nucleosynthesis left the universe in a state where the baryonic matter was composed of 75.33 %[1] hydrogen, 24.67 % helium and traces of deuterium, tritium and lithium (Planck Collaboration et al. 2016).

Over the years this gas cooled down and gravitationally accreted into molecular clouds and formed stars. The first generations of stars (Population III) fused this gas to heavier elements (metals) and supernovae distributed them into space as a foundation for the formation of new stars of low and high metallicity (Population II and I). Likewise, supernovae of these stars constantly enriched the interstellar medium with metals. Now, the interstellar medium in the Milky Way consists of about 32 % helium and traces of other metals (Danziger 1970).

Our Sun, a metal-rich Population I yellow dwarf star, emerged 4.6 billion years ago (Bahcall et al. 1995) from an accretion disk, formed by a collapsing rotating cloud. The compression within its center resulted in high temperatures, which initiated the fusion of hydrogen to helium (primarily pp chain reaction). The fusion reactions produce huge amounts of energy and heat the solar center to a temperature of 15.7 million kelvins (Christensen-Dalsgaard et al. 1996). The generated energy is transported through the solar body to its surface and eventually into space. The core region extends to about 0.25 solar radii ($R_\odot$), where the declining temperature becomes insufficient for fusion reactions. The energy transport is dominated by thermal radiation until, because of declining ionization and density, at 0.71 $R_\odot$ up to the surface convective motion takes over (Christensen-Dalsgaard et al. 1991).

The temperature at this transition region (tachocline) is about 2 million kelvins and decreases up to the solar surface to between 4400–6600 K (cite?). Here at the photosphere, the energy is radiated away with an effective black body temperature of 5772 K (Mamajek et al. 2015), classifying the Sun as a spectral type G2V star. At this surface layer granules, the tops of convection cells, and temporary sunspots are visible. Strong magnetic flux inhibits the convection at sunspots, leading to lower temperature and brightness (for more details on sunspots see the next section 2.2). Figure 2.1 illustrates these photospheric features along with the inner solar structure.

Above the photosphere at the base of the chromosphere, the temperature declines to its solar minimum of 3800 K until it raises to 2–3 million kelvins in the corona (Billings 1959; Liebenberg et al. 1975). Up to now it is not fully understood why the corona is so much hotter than the underlying chromosphere – this question is known as the coronal heating problem. The energy transfer mechanisms of choice are magnetic reconnections, wave heating and type II spicules or a combination of these (cite?).

The chromosphere is a 2000 km thick region whose features (numerous spicules, filaments and prominences) can reach far into the corona. They consist of chromospheric material channeled by the solar magnetic field, which is enveloped by a thin transition region where the temperature jumps up from ?20 000–35 000 K to coronal temperatures (cite?). Reconnection of magnetic field lines can result in the eruption of filaments into the

[1] Percentages by mass.

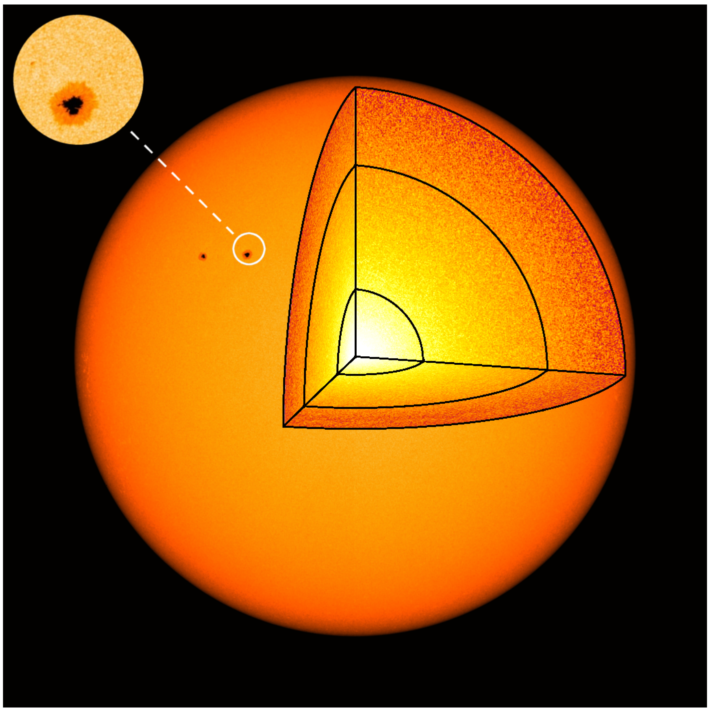

Figure 2.1 Image of the photosphere together with a schema of the solar interior structure. The inset shows the granular surface with a sunspot. The figure is based on a SDO/HMI continuum image from 20 March 2016, credit: NASA/SDO and the AIA, EVE and HMI science teams.

corona and beyond, termed coronal mass ejections (CMEs) (see also Section XX...). Details of chromospheric features are shown in Figure 2.2.

The Sun's atmosphere is dominated by the varying small- and large-scale solar magnetic field configuration. There are regions where the magnetic field lines arc back to the surface and regions with open field lines. In the latter areas the coronal plasma can – guided by the field – escape into space. Thus these coronal areas are less dense, cooler and therefore appear darker in extreme ultraviolet (EUV) and are called coronal holes (more in Section XX...). In Figure 2.2 a coronal hole is located at the solar south pole.

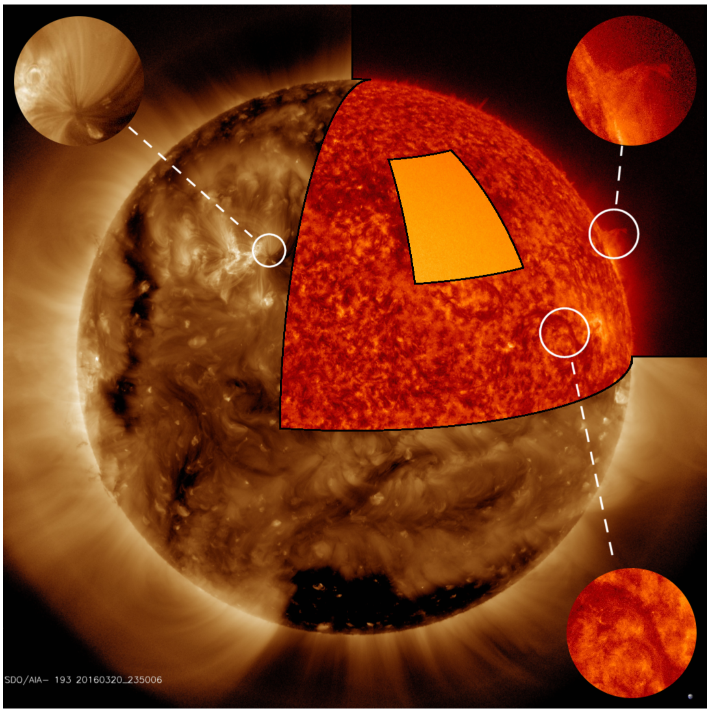

Figure 2.2 Composite image of the solar atmosphere and some of its features. Corona, chromosphere and photosphere are seen in wavelengths of 193 Å, 304 Å and continuum. Chromospheric spicules are visible on the northern limb. The enlargements on the right show a prominence and a filament. The dark region at the south pole is a coronal hole. The left inset shows details of the active region belonging to the sunspots in Figure 2.1. The figure is based on SDO/AIA images from 20 March 2016, credit: NASA/SDO and the AIA, EVE and HMI science teams.

From Earth, the faint corona and chromosphere can only be observed during eclipses, because of the brightness of the solar disk. There are three effects contributing to the visibility of the corona: photon scattering off free electrons and dust particles, and ion spectral emission lines (termed K-, F- and E-corona). The image of a solar eclipse reveals the coronal plasma, shaped by the magnetic field, and features of the red chromosphere, pictured in Figure 2.3.

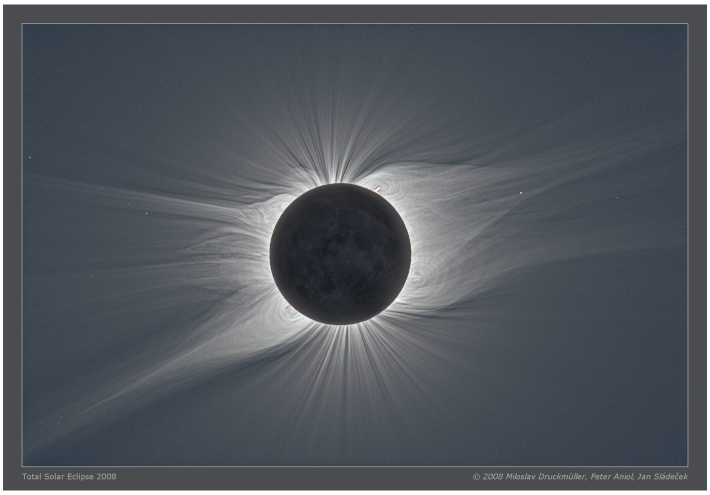

Figure 2.3 Total solar eclipse image of the inner corona up to 5 solar radii. The picture was taken in Mongolia, 1 August 2008 and is processed from multiple images. The magnetic field's dipole structure and the equatorial streamer belt, typical for a quiet Sun in cycle minimum, are visible. Credit: Miloslav Druckmüller, Peter Aniol, Jan Sládeček, 2008, reproduced with permission.

Due to the high coronal temperatures, plasma escapes from the solar gravitational field (Parker 1958) with velocities of 200–800 km s^{-1}. Its acceleration is linked to the coronal heating, however the exact location and process remain an open question (cite?). The magnetic field becomes too weak to guide the coronal plasma at a distance of a few solar radii (?4–20). From this source surface, the solar wind flows radially outward into space until it reaches the termination shock. Eventually it collides with the local interstellar medium, creating the boundary of the heliosphere, the heliopause, which is expected to be a bubble of either teardrop or croissant shape (and may be led by a bow shock), caused by the Sun's relative velocity of 23 km s^{-1} to the local interstellar medium (Owens & Forsyth 2013; Opher et al. 2015). Measurements of the Voyager 1 and 2 spacecraft indicate their passage of the termination shock at about 94 au and 84 au, entering the heliosheath region (Owens & Forsyth 2013). Gurnett et al. (2013) report that in 2012 Voyager 1 actually crossed the heliopause into interstellar space at a solar distance of 121 au. Figure 2.4 illustrates the heliosphere and its surrounding flow structure.

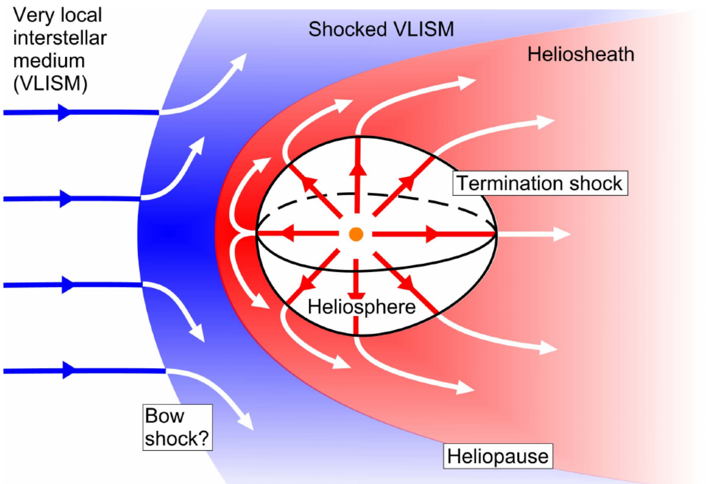

Figure 2.4 Schema of the heliosphere and its surrounding flow structure. The heliosphere is formed by the interaction of the solar wind with the local interstellar medium at the heliopause. Credit: Owens & Forsyth (2013, Fig. 9), licensed under CC BY-NC 3.0 DE.

On its way outwards through the solar system, the solar wind – carrying the solar magnetic field – interacts with the planets, their magnetic fields and other solar system bodies. These interactions have various effects, for instance disturbances in planetary magnetic fields with appearance of aurorae and enhanced radiation, atmospheric losses and stripping of cometary tails. Some of these effects can have disruptive consequences for humans and their technology. The topic of space weather effects is further addressed in section 2.6. The magnitude of these effects depends highly on spatial and temporal variations in the solar wind, which are rooted in the dynamics of the solar magnetic field.

2.2 Solar dynamics

The spin conservation of the contracting molecular cloud led to a rotation of the Sun with a current average period of about 25 days. The radial convective motion within the solar interior above the tachocline leads to a transport of momentum away from the rotation axis and therefore to a slower polar and faster equatorial rotation in the convection zone (Miesch 2005). This differential rotation is visible on the surface and was first discovered from sunspot observations. With a rotation period of about 34 days the poles have a lag of almost 9 days (for further information on solar rotation see appendix section A.5). The differential rotation in the solar interior can be inferred from helioseismological observations, see Figure 2.5.

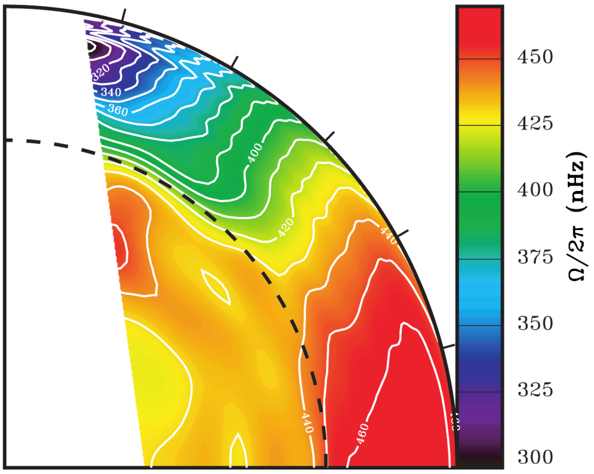

Figure 2.5 Angular rotation velocity in the solar interior. The radiation zone has a nearly solid rotation. Above the tachocline (dashed line) begins the differential rotation of the convection zone. The angular velocity is inferred from helioseismology via observations from the Michelson Doppler Imager (MDI) at the Solar and Heliospheric Observatory (SOHO) spacecraft. Credit: Thompson et al. (2003, Fig. 3), reproduced with permission, © Annual Reviews.

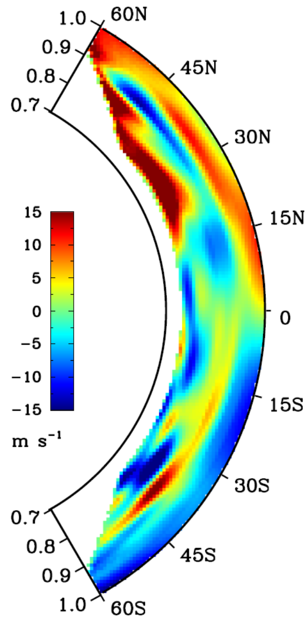

Figure 2.6 Meridional flow velocity profile in part of the convection zone. Positive values are directed towards north. The velocity is inferred from helioseismology via observations from the Helioseismic Magnetic Imager (HMI) at the Solar Dynamics Observatory (SDO) spacecraft. Credit: Zhao et al. (2013, Fig. 4, panel a), reproduced with permission, © AAS.

Turbulent plasma motions from convective flows in the convection zone generate and carry magnetic flux. The large rotational shear at the tachocline stretches and amplifies the disorganized magnetic fields (ω-effect) to strong coherent toroidal flux with intensities of the order 1–10 T. These toroidal fields, generated near the bottom of the convection zone, can be stored in a deep magnetic layer located in the stably stratified region below the convection zone (Ossendrijver 2003). The stronger flux ropes become buoyant and raise to the surface. The Coriolis force twists them systematically, the twist is stronger at higher latitudes (Joy's law), on their way through the convection zone (α-effect). They emerge then on the photosphere as bipolar active regions – the stronger ones forming pairs of sunspots, see Figure 2.7. Turbulent convective diffusion of this surface flux contributes to the build-up of poloidal fields. Their resulting polarity is opposite to the prevailing global field, due to the directional way the rotational shear at the tachocline and the Coriolis force in the convection zone act. Fluctuating motions further amplify the mean fields in these processes. This solar α-ω-dynamo is thought to create the major part of the solar magnetic field. Still, with regard to the magnetic field's high variability, the long-term mean fields are governed by intermittent localized structures, that is, active regions, filaments and coronal loops (Miesch 2005).

the α-ω-dynamo, see Figure 2.8

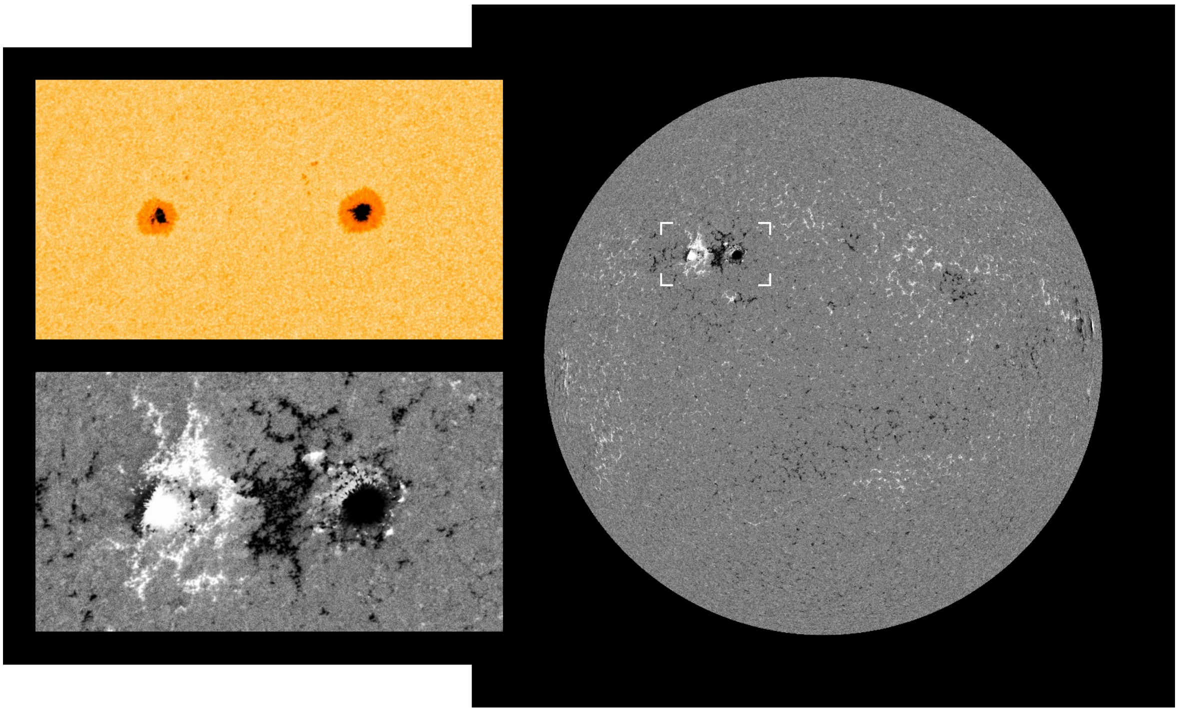

Figure 2.7 Continuum image of both sunspots from Figure 2.1, magnetogram from the same region and from the whole solar disk. The magnetogram shows the polarity of the line-of-sight magnetic field component at the photosphere (black/white: inward/outward polarity). The highly concentrated magnetic flux at the sunspots is clearly visible in the magnetogram as well as the extended bipolar magnetic field structure of the whole active region. The solar disk is scaled to the same size as in Figure 2.1. The figure is based on SDO/HMI continuum and magnetogram images from 20 March 2016, credit: NASA/SDO and the AIA, EVE and HMI science teams.

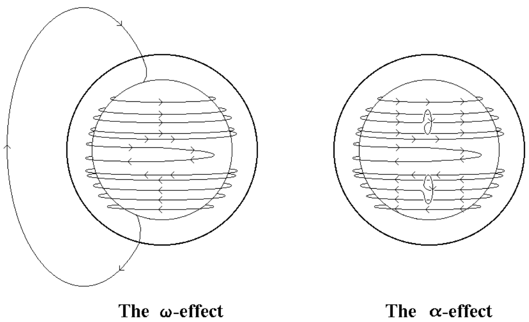

Figure 2.8 Schemata of the ω and the α-effects. figure really necessary? get permission...

2.3 Solar activity cycle

Helioseismic measurements reveal that the large-scale convective flow is agglomerated into large convection cells with slow meridional flows of a few $\mathrm{m\,s^{-1}}$, see Figure 2.6. A poleward subsurface flow and equatorward backflow beneath with a further poleward flow below are detected within each hemisphere, comprising a stacked double-cell profile. The meridional circulation flow speed has a major influence on the average 22-year period of the emerging magnetic flux at the solar surface. This period varies and is influenced by the stochastic emergence rate and tilts of active regions and the diffusion from random convective motions (Hathaway & Upton 2016). Within one period, the surface magnetic field configuration changes from a dipole structure to a reversed dipole structure with opposite polarity, thus the transition time from one dipole state to the next lasts about 11 years, this period is termed solar cycle.

In the transition phase, magnetic flux emerges in belts above and below the solar equator, manifesting as bipolar active regions with sunspots, resulting in a toroidal/multipolar structured magnetic field. Sunspots appear at about $\pm 20°$ latitude at the beginning of a cycle, this shifts towards lower latitudes at the end of a cycle. Thus the plot of sunspots over latitude and time reveals a butterfly pattern (Maunder 1904). This butterfly pattern appears in surface radial magnetic field observations as well, see Figure 2.9. The leading polarity of bipolar regions is opposite in both hemispheres and the leading polarity changes with each cycle

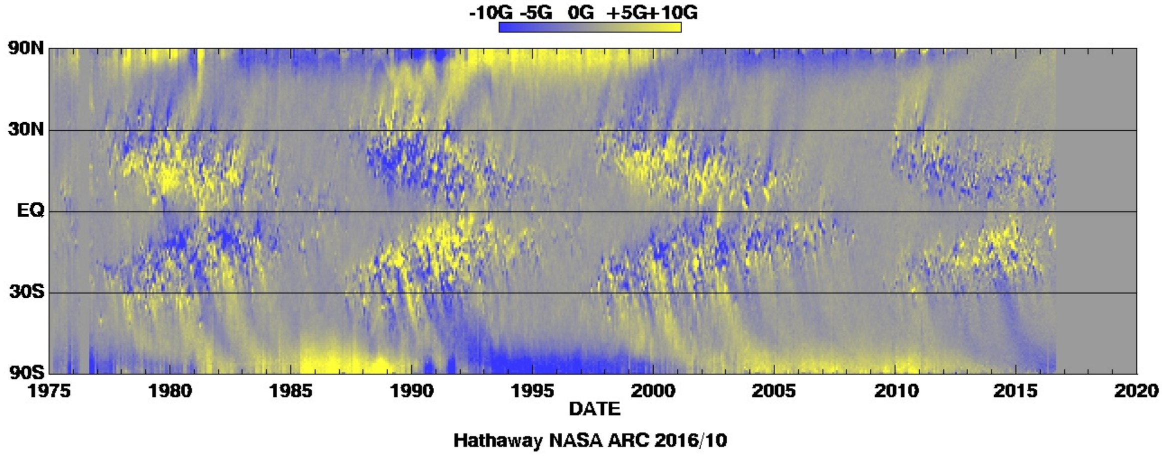

Figure 2.9 Magnetic butterfly diagram of the synoptic radial magnetic field on the solar surface. Yellow represents an outward directed magnetic field (positive), blue inward (negative). The data is obtained from instruments on Kitt Peak National Observatory and from the MDI at the SOHO spacecraft. Credit: David Hathaway, NASA Marshall Space Flight Center (updated version of Hathaway 2015, Fig. 17). Update this figure before printing!

(Hale's polarity law). The emerging flux is carried by the slow meridional surface flow poleward, canceling the current dominating polar field polarity and eventually resulting in the polar field switch (Hathaway 2015).

Since regions of strong magnetic flux are visible as sunspots on the photosphere, they were known well before the common era by greek and chinese scholars (Vaquero 2007; Clark & Stephenson 1978). Systematic sunspot observations exist since 1610, shortly after the invention of the telescope. In 1843 Schwabe discovered the 11-year periodicity in the sunspot occurence (Schröder 2004, p. 124). In 1848 Wolf introduced the sunspot number (SSN), see Figure 2.10, and the solar cycle number (the zeroth in 1749) to record these cycles (Hathaway 2015). The SSN observations show large variations in cycle length (9–14 years) and cycle amplitude, with

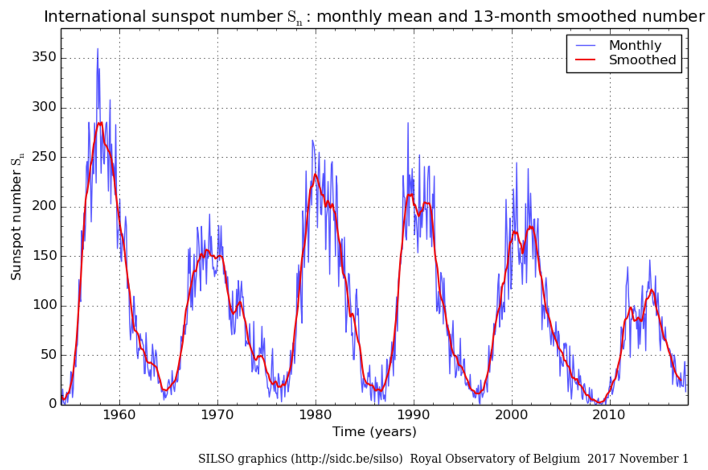

Figure 2.10 Monthly mean sunspot number (blue) and 13-month smoothed monthly sunspot number (red) since 1954. Credit: SILSO data/image, Royal Observatory of Belgium, Brussels, 2017. Update this figure before printing!!!

peak SSNs in the range 0–300, (Hathaway 2015). There also exist long-term variations, such as the 70-year Maunder Minimum, during which from 1645 on almost no sunspots were observed, (Maunder 1890). The source of the variations in the solar cycle periods and amplitudes are variations in the meridional circulation, because their fluctuations are larger than those found in the differential rotation and in the convective motions (Hathaway 2015).

As the SSN is commonly used as an indicator for solar activity, there exists interest in its prediction for the course of the actual and upcoming solar cycles. The continuing prediction of an already commenced activity cycle is reliable, but then the prediction of a cycle before it began is more difficult. Though, there are indications that the polar magnetic field strength during the preceding activity minimum is correlated to the strenght of the next solar cycle (Schatten & Sofia 1987). However, Hathaway & Upton (2016) suggest that the predictability of solar cycles is generally limited – accumulated uncertainty produced by stochastic motions in the convection zone makes predicitons further than the next solar cycle very unreliable.

2.4 Heliospheric magnetic field

In the quiet Sun during solar cycle minimum, open coronal regions are the photospheric sources of the heliospheric magnetic field (HMF). Bright points between the granules on the photosphere are detected in G-band (430 nm) images. They are identified as magnetic flux tubes with field strenghts of 100–200 mT (Cranmer & van Ballegooijen 2005). Together these magnetic bright points (MBPs) cover around 1–2 % of the solar surface and carry many times the flux that active regions do (Sánchez Almeida et al. 2010). These thin flux tubes expand laterally in the low chromosphere and merge to homogeneous network fields, which expand and merge again to a large-scale canopy below the transition region (see Figure 2.11).

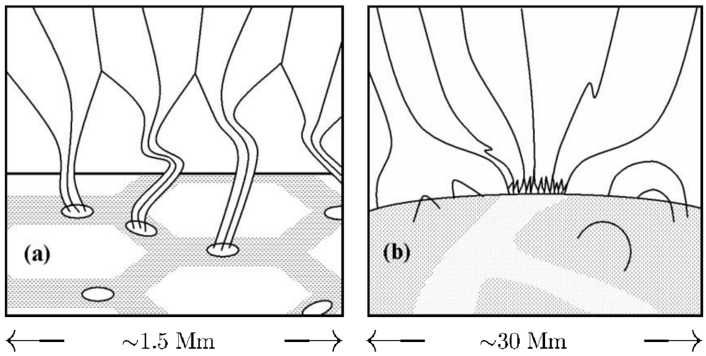

Figure 2.11 Schemata of superradially expanding magnetic flux. MBPs between granules on the photosphere are thin magnetic flux tubes that merge to a homogeneous network field (a). The network field expands again to the large-scale canopy field of the lower corona (b). Credit: Cranmer & van Ballegooijen (2005, Fig. 1), reproduced with permission, © AAS.

The MBP's convective appearance and stochastic motions result in wavelike fluctuations that propagate upward from the photosphere through the superradially expanding flux tube – leading to incompressible waves leaking into the solar wind (Cranmer & van Ballegooijen 2005). These Alfvén waves propagate with a characteristic speed along the magnetic field lines – for more details about Alfvén waves and Alfvén speed see appendix section A.4. The local Alfvén speed equals the solar wind speed at around 17 $R_\odot$ (Sittler & Guhathakurta 1999; Exarhos & Moussas 2000). It is believed that the solar wind is accelerated until this so-called Alfvén critical surface (cite?).

The coronal plasma expands superradially, following the magnetic field lines. However, the field strength decreases with increasing solar distance and at a distance of about XX Rs, the thermal pressure becomes larger than the magnetic pressure. Thereby the magnetic field gets frozen within the plasma and is carried by the solar wind radially outwards into the heliosphere. The distance from which the solar wind propagation uncouples from the magnetic field lines is called the source surface and the thermal to magnetic pressure ratio is called plasma beta – for more details on plasma beta see appendix section A.3. The magnetic field changes from superradial expansion below the source surface to a radial configuration above it, this field geometry is also visible in the total eclipse image Figure 2.3.

Under solar cycle minimum conditions, a heliospheric current sheet (HCS) separates the two different magnetic polarities originating from both polar coronal holes. The HCS is roughly located in the equatorial plane, dividing both hemispheres. The analytical solar magnetic field model for solar minimum conditions, constructed by Banaszkiewicz et al. (1998), shows this field geometry as seen in Figure 2.12. The quadrupole part of their dipole plus quadrupole plus current sheet (DQCS) model considers the closed equatorial fields and allows equatorial outflows along the current sheet.

The solar-wind source surface rotates with the Sun and thus shears the HMF into an Archimedean spiral pattern, adding an azimuthal component to the radial HMF. This geometry was anticipated by Parker (1958) and is today called Parker spiral. Commonly the HCS looks more like a ballerina skirt, due to magnetic field variations, and thus the Parker spiral has sectors of different magnetic polarity, whose boundaries are separated by the HCSs. Figure 2.13 shows the Parker spiral viewed in the ecliptic plane, where the solar rotation axis tilt of up to 7.25° leads to a slight diving into both hemispheres of opposite polarity.

That way the HMF is carried out to the termination shock by the solar wind. MHD simulations, based on Voyager 1 and 2 measurements within the heliosheath, provide indications about the outer structure of the heliosheath. After the termination shock, the magnetic sector boundaries are compressed and they reconnect, forming magnetic bubbles (Opher et al. 2011). These bubbles – unconnected to the HMF – flow away to the heliosheath tail region. Even beyond the termination shock, the solar wind plasma is confined and collimated by the twisted solar magnetic field and driven into a northern and a southern jet (Opher et al. 2015). Hence, the

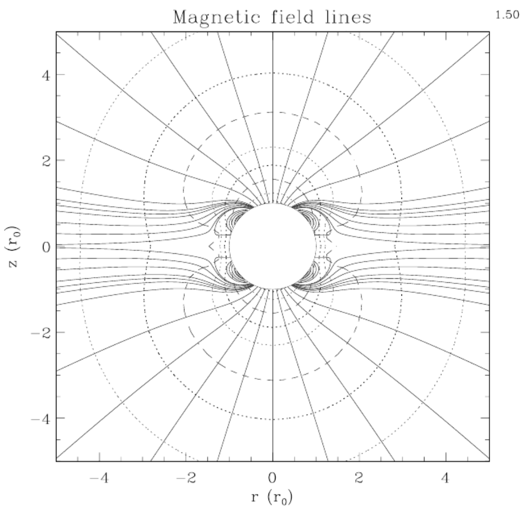

Figure 2.12 Model of the solar magnetic field geometry in the polar plane for solar cycle minimum. Magnetic field lines (solid) and constant field strength surfaces (dashed) from the DQCS model are plotted. The field line spacing does not represent the field strength but provides better detail where needed. The HCS forms a few solar radii distance at $z = 0$. Credit: Banaszkiewicz et al. (1998, Fig. 3), reproduced with permission, © ESO.

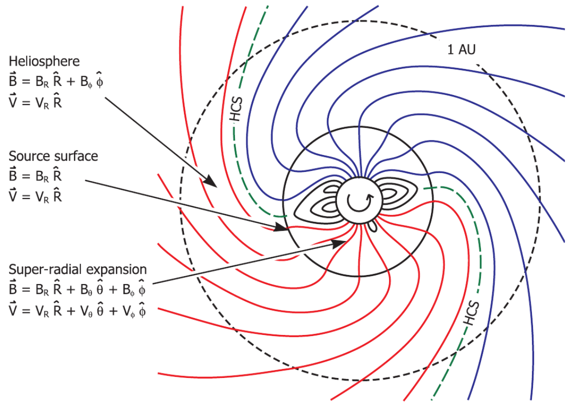

Figure 2.13 Illustration of the Parker spiral formation in the ecliptic plane outside the source surface. The HCS (green) forms between solar-wind flows of opposite magnetic field polarity (red/blue). Credit: Owens & Forsyth (2013, Fig. 1), adapted from Schatten et al. (1969, Fig. 1), licensed under CC BY-NC 3.0 DE.

Sun's magnetosphere has likely a croissant-like shape with two turbulent tail-lobes, where eventually the solar wind and the HMF are mixed into the interstellar medium.

2.5 Solar wind

It is observed that cometary tails lag a few degrees from the radial direction away from the Sun, sometimes they also show fluctuations and become kinked. As such behavior could not be explained by interaction with sunlight pressure, eventually Biermann (1951) concluded that cometary ion tails are influenced by a continuous flow of particles from the Sun.

Parker (1958) considered the consequences of Biermann's conclusions and built a solar-wind model, adopting an expanding isothermal solar atmosphere. Parker also incorporated the implications for the solar magnetic field in his model and hence he laid the theoretical foundations for a continuous supersonic radial outflow of magnetized plasma.

Thus, the existence of the solar wind was postulated before the first satellites measured it in situ in 1959 (Gringauz et al. 1960; Neugebauer & Snyder 1966). Since that time spacecraft are able to measure the solar wind almost continuously with in situ magnetometer and plasma instruments (see section 3.1).

From Earth, the outflow of near-Sun solar wind can be observed during solar eclipses, see the eclipse photo in Figure 2.3.

The solar wind is a magnetized plasma mainly composed of hydrogen and a small percentage of helium (protons and alphas).

Its properties are highly variable in time and space and the average parameter magnitudes scale with solar activity and solar distance.

sw quantities, such as flux densities, mass flux and plasma beta are derived from 4 parameters
proton plasma – the average helium abundance is about 4.5 % and in slow wind at minimum even less than 2 % Feldman1978,Schwenn1983,Kasper2012.

the parameter ranges at Earth distance:
The plasma properties are determined by the values of the solar-wind parameters magnetic field strength, pro-

ton velocity, density, and temperature. Mots of the time their typical values lie in the ranges 3–8 nT, 300–500 km s^{-1}, 2–8 cm^{-3}, and 10^4–10^5 K (cite?, Venzmer2017?).

having these parameter ranges the sw is a plasma with a beta in the range xx–xx

Plasma in general; properties (H/He/metal composition; see paper...), Plasma-beta...

sw density considerations, see presi S³

Solar-wind structures

MHD waves (Alfvén waves)
in HSSs (cite?)

prepare following subsections:
slow/fast wind
-> following event/structure types
special events/configurations, which can appear (CIRs, HCS/HPS, etc.)
HSS, sector boundaries, CIRs, CMEs

prepare next subsection:
different source regions: sunspots/active regions, coronal holes, and filaments.

sonic and Alfvénic critical point positions (see Sittler & Guhathakurta (1999))
sonic point and slow solar wind origin (Sheeley et al. 1997)

2.5.1 Slow and fast streams

The ordered dipole structure in solar cycle minimum leads to open polar field regions with large coronal holes and a closed equatorial field belt/streamer belt (clearly visible in Figure 2.3).

sw in minimum: streamer belt and polar HSSs
active regions forming equatorial streamer belt

minimum: polar coronal holes
fast solar wind emerges from CHs
slow from closed field streamers; different sources...
open field lines (coronal holes) -> HSSs

cycle maximum:
This leads to the chaotic appearance of closed field lines even at higher latitudes/poles and coronal holes covering equatorial regions.

trapped plasma, slow solar wind from streamers
regions with closed lines

regions with open lines
coronal holes as sources of fast sw
high speed streams

sw plot of HSS with CIR to refer to

Schwenn (1983): "During the Skylab era in 1973/74 we learned that these high speed streams emerge from coronal holes (Hundhausen, 1977 and references therein)."

This is confirmed by the Ulysses spacecraft, which measured the solar-wind speed in a polar orbit covering more than one solar cycle (Figure 2.14).

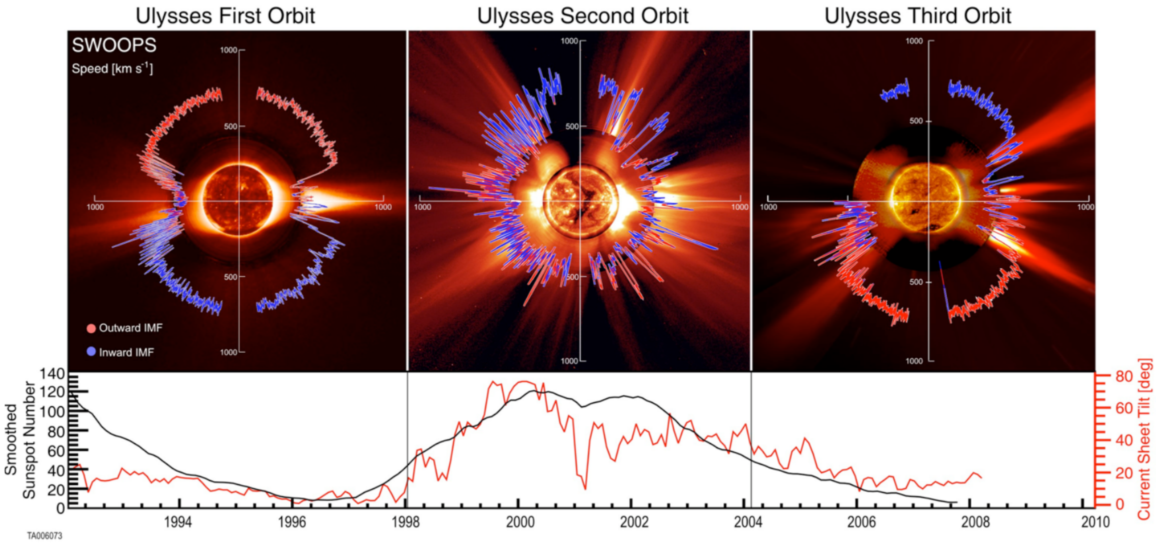

Figure 2.14 Solar-wind velocity and magnetic field polarity (red/blue) with respect to heliographic latitude for the three orbits of the Ulysses spacecraft during low and high solar activity (upper panels). The data starts left and couterclockwise. The corresponding smoothed SSN (black) and HCS tilt angle (red) are plotted beneath. The background consists of solar images for solar cycle 22 minimum (1996-08-17), solar cycle 23 maximum (2000-07-12), and solar cycle 23 minimum (2006-03-28). The solar disk, inner corona, and outer corona images are from SOHO/EIT (Fe XII at 1950 nm), Mauna Loa K coronameter (700–950 nm), and SOHO/C2 white light coronagraph. Credit: McComas et al. (2008, Fig. 1), reproduced with permission, © American Geophysical Union. ...ask for high res. image?

visible solar-wind structures (coronagraph image; with CME and streamer)

2.5.2 Stream interaction regions

in-situ measurements (example in situ CIR/HSS plot)
stream interfaces (figure and link to previous CIR plot) -> HCS/HPS
equatorial ballerina model -> CIRs (figure?)

reviews: Balogh & Jokipii (2009) (for heliosheath), Owens & Forsyth (2013)

heliospheric current sheet (HCS)
heliospheric plasma sheet (HPS)

Winterhalter1994 The heliospheric plasma sheet:
"the narrow heliospheric current sheet (ca. 3000–10 000 km thick), together with the heliospheric plasma sheet in which it is embedded. The heliospheric plasma sheet region is identified by a significantly enhanced plasma beta caused by density enhancements and diminished magnetic field strength and is about 20 to 30 times the thickness of the current sheet."

Corotating interaction regions (CIRs)
Stream interaction regions (SIRs)

Streams of fast wind catch slow wind
-> compressions, shocks, deflections

formation of stream interface and stream deflection, see Figure 2.15

HCS/HPS

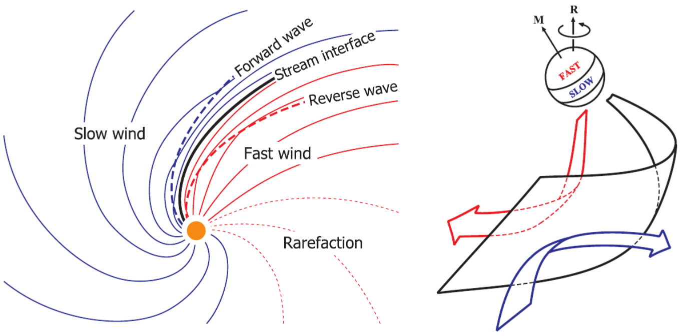

Figure 2.15 Schema of the formation of a stream interface (left) and deflection of streams (right), both generated from interactions between slow and fast solar wind. Credit: Owens & Forsyth (2013, Fig. 7); right panel adapted from Pizzo (1991, Fig. 2), licensed under CC BY-NC 3.0 DE.

from sector boundaries (ballerina skirt)

CIR and HSS, see Figure 2.16

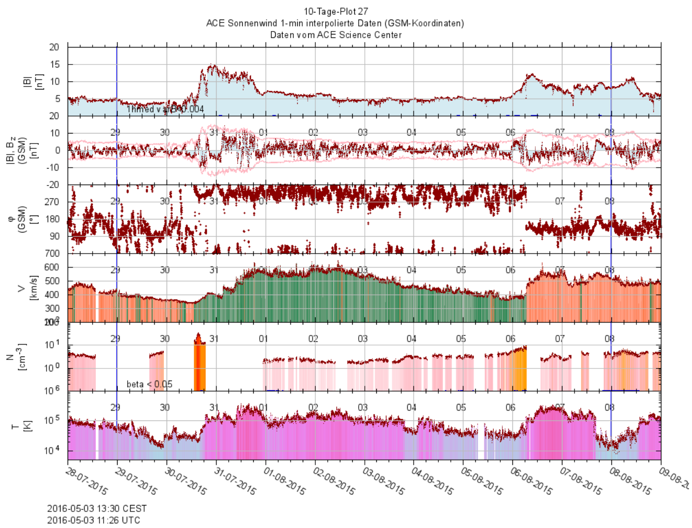

Figure 2.16 HSS with CIR?. ACE data find optimal event + remake figure...

2.5.3 Coronal mass ejections

Embedded in the solar-wind streams are CMEs. Their frequency in near 1 au measurements varies between almost zero during solar cycle minima up to a daily rate of about 0.5 during times of solar maximum (Richardson & Cane 2012).

CMEs (link to previous coronagraph image; in situ CME/MC plot)

flares + CMEs

The solar differential rotation wraps the magnetic field lines, accumulating tension, leading eventually to relief with a magnetic reconfiguration by field line reconnections.
–> release of much energy –> flares, CMEs

Coronal mass ejections (CMEs) (discovery (Carrington), definition (Hundthausen?), models, GCS (conception of 3-dim CME shape –> enables Earth arrival time forecast from modeled direction and velocity))

active regions:
sunspots, magnetic reconnections, flares, post-eruptive arcades

coronagraph figure of CME (COR2 image, SECCHI/STEREO), see Figure 2.17

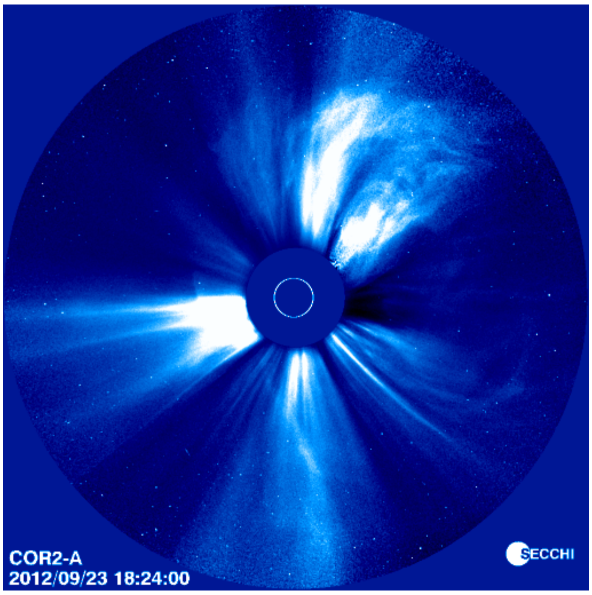

Figure 2.17 Coronagraph image of a CME. STEREO A, SECCHI-A COR2, COR2-A, date 0120923-182400. Credit: NASA/STEREO... find optimal event...

in-situ solar wind figure of same CME (recent one from 2016)

CME-plasma properties
+ flares and SEPs often accompany CMEs

magnetic clouds
magnetic cloud (MC); see in-situ plot Figure 2.18
See BS magnetic cloud model in analyses methods chapter MVA...

CME with MC, see Figure 2.18

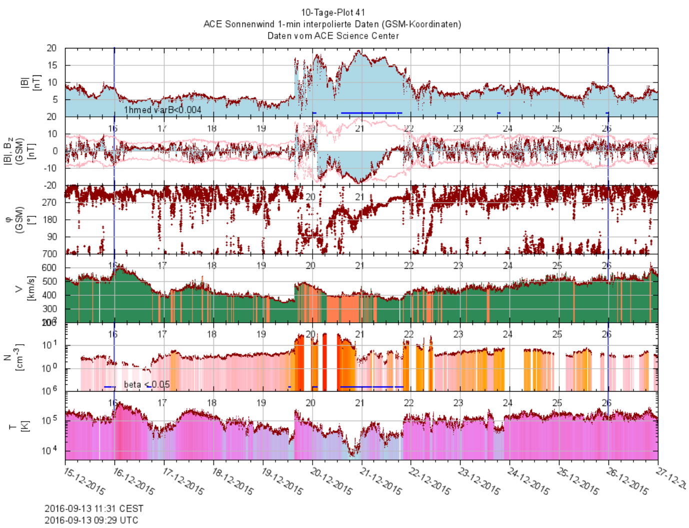

Figure 2.18 Solar-wind in-situ measurements wich show a CME with a MC. B, v, n, and T. ACE data. find optimal event + remake figure...

the CME's MC and its impact on the magnetosphere (Kp), see Figure 2.18

history (paper); properties -> CHs and streamers; fast/slow; Ulysses -> SIRs; in situ fig -> CMEs; coronagraph fig; in situ fig

keywords:
SSN -> poloidal/toroidal field -> magnetic surface activity (butterfly diagram) -> min/max polar CHs (quiet/active Sun figure) -> HMF (quiet B-field figure) -> quiet HMF Parker spiral (figure) -> solar wind -> slow/fast sw

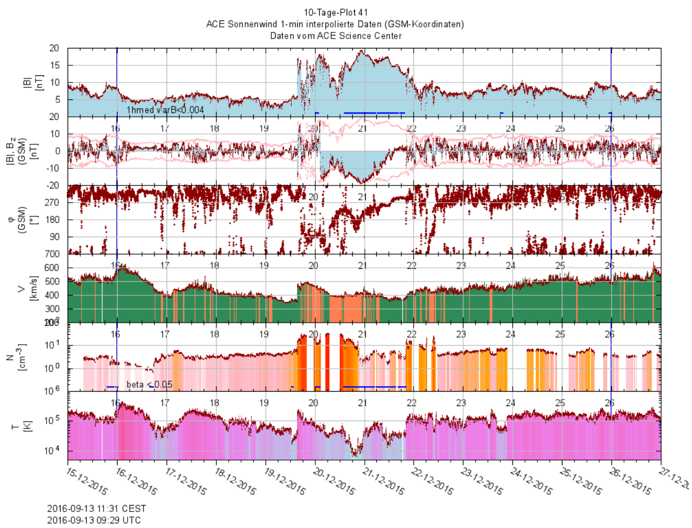

Figure 2.19 Solar-wind in-situ measurements wich show the MC of the CME. B, Bz (GSM), Bphi (GSM, and Kp. ACE and Kp data. find optimal event + remake figure...

pattern (Ulysses figure))

2.6 Space weather

Solar wind influences the terrestrial magnetosphere and can disturb sensitive technical systems
understanding its properties helps with prediction of events

various space weather effects, for instance disturbances in magnetic fields, aurorae, episodes of enhanced radiation, atmospheric losses and stripping of cometary tails. figures of these effects?

influences on human infrastructure/technical systems/animals (such as birds and whales -> Vanselow2017 10.1017/S147355041700026X)

reference to Bothmer & Daglis (2007), maybe images

2.6.1 Solar influence on Earth

solar wind's impact on Earth

Carrington made first connection between terrestrial magnetic field and solar flares. correct?

there are several types of solar-terrestrial relations, Bartels (1962) listed:
a) irregular flare and CME effects (Carrington)
b) 11-year solar cycle effects
c) 27-day solar rotation effects
d) daily effects (x-ray and light)

seasonal effects from Earth orbital distance, inclination (solar rotation axis angle) and Earth tilt (see Figure 2.20)

solar wind and its structures
solar radiation
solar energetic particles (SEPs)
gravitation

magnetosphere
ionosphere?

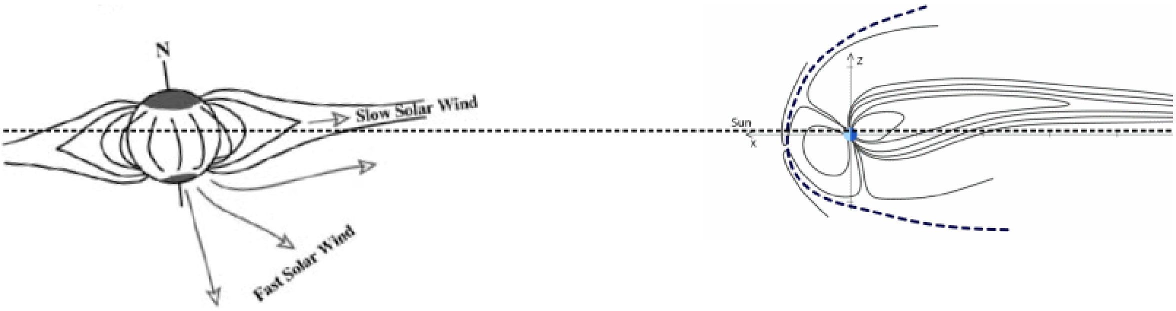

Figure 2.20 Sun-Earth geometry in the plane orthogonal to the ecliptic (not to scale); Solar magnetic field-magnetosphere geometry. Seasonal effects are: solar tilt, Earth distance and Earth tilt. make new figure...

aurorae
geomagnetic storms (several days, from CMEs)
substorms (few hours, from CIRs??)

for humans and their technology important effects: enhanced radiation, geomagnetic storms
lovely, disruptive, dangerous consequences <– read in VBbook

at Earth the solar wind total energy flux (1.45 mW/m^2) is only about one millionth of the solar radiation flux (see Schwenn (1990, p. 153))

"The principal users affected by geomagnetic storms are the electrical power grid, spacecraft operations, users of radio signals that reflect off of or pass through the ionosphere, and observers of the aurora."NOAA cite

2.6.2 Magnetosphere

The magnetosphere's shape is formed by the dynamic pressure balance. The structure is similar to the heliosphere in the ISM.

bow shock, magnetotail, magnetosheath, magnetopause
add ecliptic and terrestrial tilt angle; with plasmoid?
see Figure 2.21

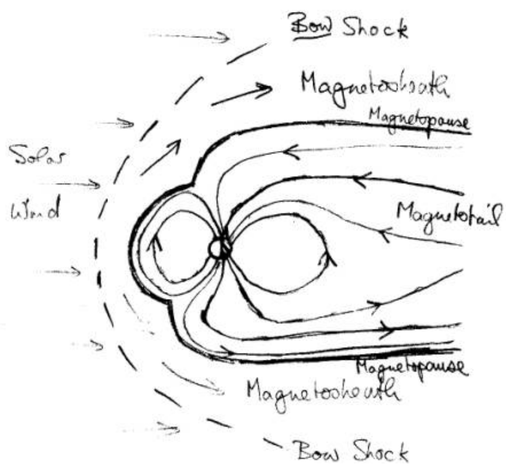

Figure 2.21 temp figure "The cavity is called the magnetosphere. It has a relatively well-defined outer boundary, the magnetopause."

turbulence with sw (KH or RT instabilities)

Earth magnetic field strength at a height of 36 000 km (geostationary): ≈100 nT
Earth magnetic field strength at the surface - equator: ≈30 000 nT - poles: ≈60 000 nT (cite?)

magnetopause = current layer??

two extreme cases of Bz orientation: parallel/antiparallel
compression/reconnection (see Figure 2.22)

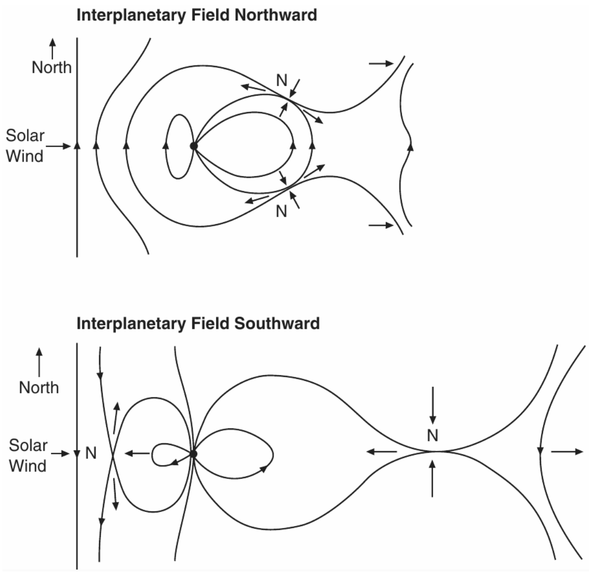

Figure 2.22 reconnection and compression depending on the interplanetary magnetic field orientation. Credit: Bothmer & Daglis (2007, p. 116, Fig. 4.8), adapted from Dungey1961, 1963. get permission... accelerated flows are arrowed; N points are X points...

standoff distance: (Bothmer & Daglis 2007, p. 112)

$$d = \frac{107.4}{1R_\mathrm{E}}(NV^2)^{-1/6} \tag{2.1}$$

Even in "ancient" times (when?) a correlation between solar particles and disturbances in the magnetosphere were known of (Bartels1962).

magnetosphere variations due to solar wind
magnetosphere protects from radiation (maybe from solar wind stripping atmosphere away?)

effects: aurorae, ...

ring current systems

definition of:
magnetic storm...
substorm...

subsection Ionosphere?
its variations due to solar radiation (day/night cycle and flares)
ionosphere -> TEC -> GNSS error

Solar wind interaction processes with the magnetosphere:
there are several underlying physical mechanisms, whose contribution is not yet quantified'?'
physical mechanisms:
- reconnection
- compression
- turbulence
- induction?

three ways for solar wind momentum and energy transfer into magnetosphere:
- sw entering sphere
- waves/eddies

- reconnection

2.6.3 Solar wind–magnetosphere coupling

E-field produced by solar wind: acts on magnetospheric plasma

$$\mathbf{E}_{\mathrm{IMF}} = -\mathbf{V} \times \mathbf{B}_{\mathrm{IMF}} \tag{2.2}$$

from Lorentz force F = -e vxB
E = -F/e
Because of high plasma conductivity the E-field is not existent.

Axford1964 viscous interaction (of turbulent nature, KH/RT instabilities, KH instabilities at the flanks of the magnetosphere) is a viable source of drag force/solar storm energy input into magnetosphere

Otto&Nykyri1982 KH instabilities/vortices force magnetic reconnection even at northern IMF and are able to account for observed mass flux

Newell et al. (2007) and Newell et al. (2008): coupling consists of merging and viscous part (reconnection and turbulence)
merging part: universal sw-magnetosphere coupling function; rate magnetic flux is opened at the magnetopause ($d\Phi_{\mathrm{MP}}/dt$)
viscous part: reconnection due to Kelvin-Helmholtz instabilies at the boundary ($n^{1/2}v^2$)
equation for the least variance linear prediction of Kp: $Kp = 0.05 + 2.244 \times 10^{-4} d\Phi_{\mathrm{MP}}/dt + 2.844 \times 10^{-6} n^{1/2} v^2$
combination of both terms works best (r = 0.866)

Merkin2013 MHD simulation of velocity shear at magnetosphere boundary with northern IMF; KH instabilities; double-vortex sheet structure

2.6.4 Geomagnetic indices

Geomagnetic observatories are distributed widely over the globe, measuring the local magnetic field at their position. Several sets of stations, covering specific regions, are defined to monitor the state of different parts of the magnetospheric system. Magnetic measurements from these sets define several geomagnetic indices. The International Association of Geomagnetism and Aeronomy (IAGA) supports the following global geomagnetic indices which are serviced by the International Service of Geomagnetic Indices (ISGI)[2]: The *aa* index is designed to represent the amplitude of the global geomagnetic activity, normalized to a geomagnetic latitude of ±50°. The *am* index characterizes the global geomagnetic activity. The *Kp* index is designed to measure geomagnetic disturbances from solar particle radiation [reword...]. The *Kp* index is described in more detail in subsection 3.2.2. The *Dst* index monitors the intensity of the magnetospheric ring current. The *PC* index monitors the polar cap magnetic activity – it approximates the amount of energy which entered the magnetosphere through solar-wind coupling. The *AE* index and its relatives *AU*, *AL* and *AO* measure the magnetic effects of the northern auroral electrojet. The first three listed indices (*aa*, *am* and *Kp*) are calculated from different sets of local 3-hourly *K* indices, which measure the local magnetic disturbances at the observatories. There exist several more indices that are based on some of those listed above.

[for *Kp*, *AA* and *Dst* read Section 7.4 in book Bothmer & Daglis (2007)...
Dst (read book Jursa1985 p. 4-31)]

Lockwood et al. (2014) even used geomagnetic indices to reconstruct the near-Earth solar wind magnetic field strength and velocity back to 1845.

[2]ISGI website: http://isgi.unistra.fr/

3 Data

3.1 Instruments

For analyzing the solar wind and related effects on the Sun there are remote instruments (solar imager and coronagraphs) and in-situ instruments (magnetometer and plasma detector).
Here the basic principles of the latter are described, because the analyses performed in this thesis are based on in-situ solar-wind measurements.

3.1.1 Magnetometer

Spacecraft nowadays carry two different magnetometer types, one for measuring the magnetic field direction and its strength and the other for observing the magnetic flux and detecting waves.

A flux gate magnetometer consists of two coils around a core – one coil with alternating current, wich is compared with the induced current signal from the other. Without external magnetic field both patterns match. The core is easier magnetized in direction of an existing external magnetic field, in which case the patterns differ. It measures...
In a search coil magnetometer one coil is placed around a core; measures plasma waves - where?

Because these magnetometer types are directional, they often are placed in two sets of triaxial configurations, attached on booms to minimize the influence of the spacecraft's own magnetic field.
L-> which is generated by surface charges?/electrons?/ionization?/the instruments?

examples:
ACE/MAG – fluxgate magnetometer

3.1.2 Plasma detector

several spectrometers with different energy ranges

isotope spectrometer - isotopic abundances of SEPs
ionic charge analyzer - charge state of SEPs
sw ion mass spectrometer -
sw ion composition spectrometer -
radio burst tracker

A plasma detector measures the ion energy frequency distribution, which consists basically only of protons and alphas in solar wind (see Figure 3.1). see also section 2.5

From the energy spectrum the velocity, density and temperature can be derived.

The bulk velocity is derived from the distribution's average energy.
The number density is the area of the distribution.
The temperature scales with the distribution's width.

ACE/SWEPAM

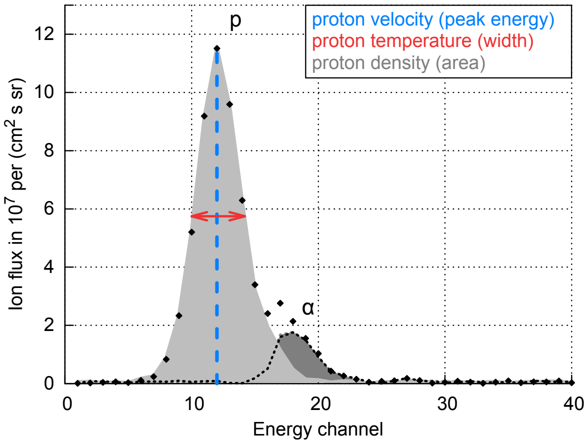

Figure 3.1 Example of an ion energy spectrum with synthetic data. Here proton and helium (alpha) peaks are distinguishable...

3.2 Data sources

Different kind of data are used for the investigations in this thesis – collected from observatories at various locations.

Spacecraft / data sets

Positions:
Earth:
imager, magnetosphere
L1 - first Lagrangian point:
ACE (siehe auch space weather spacecraft Liste)
Wind etc. (OMNI)
DSCOVR
1 au orbit
STEREO A and B
inner heliosphere:
Helios 1 and 2
PSP
outer heliosphere:
Voyager 1 and 2
Ulysses

A time coverage overview of the data sets used in the analyses of this thesis (SSN, *Kp* index, LRO, HRO, Helios 1 and 2) is plotted in Figure 3.2.

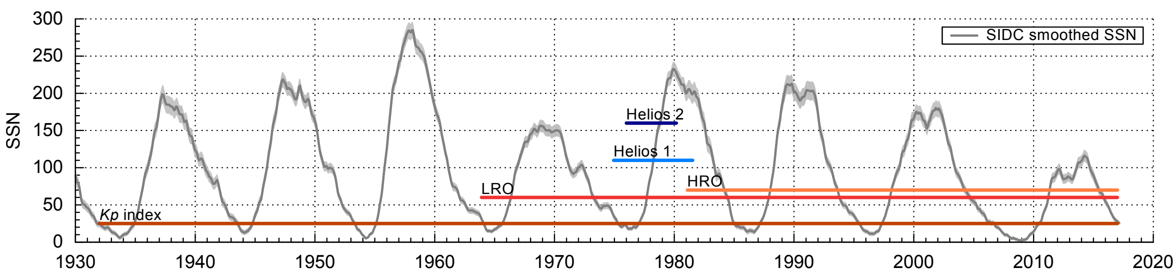

Figure 3.2 Time coverage of the *Kp* index, low and high resolution OMNI, Helios 1 and Helios 2 data sets until end of 2016. The SIDC 13-month smoothed monthly SSN is plotted in the background. add cycle number...

3.2.1 Sunspot number

SSN history in section basics
add SSN figure of history incl. Maunder minimum?

Table 3.1 Defined table for the conversion from the *Kp* index to the equivalent *ap* index, which represents the magnetic field strength in units of 2 nT.

Kp	0o	0+	1−	1o	1+	2−	2o	2+	3−	3o	3+	4−	4o	4+
ap	0	2	3	4	5	6	7	9	12	15	18	22	27	32
Kp	5−	5o	5+	6−	6o	6+	7−	7o	7+	8−	8o	8+	9−	9o
ap	39	48	56	67	80	94	111	132	154	179	207	236	300	400

SIDC/SILSO... see paper...
SSN Version 2.0
WDC-SILSO – World Data Center-Sunspot Index and Long-term Solar Observations

3.2.2 *Kp* index

Julius Bartels introduced the *K* index in 1938 and designed it to measure the intensity of geomagnetic disturbances (Bartels et al. 1939). Its name originates from 'Kennziffer' – the german word for characteristic digit. The *K* index is a measure for the maximal variation of the surface magnetic field, observed in a magnetogram within 3-hour intervals. Its scale in the range 0–9 is a quasi-logarithmic representation of the actual magnetic field strength's variations.

The Planetary *K* index (*Kp*) is a planetary geomagnetic disturbance index, introduced by Bartels in 1949 at the Institute for Geophysics, University of Göttingen (Bartels & Veldkamp 1949). *Kp* is the weighted average of 13 *Ks* indices, which are the standardized versions of the local *K* indices measured at 13 observatories. These contributing observatories are located around ±50° geomagnetic latitude and their distribution is biased towards Europe (see Figure 3.3).

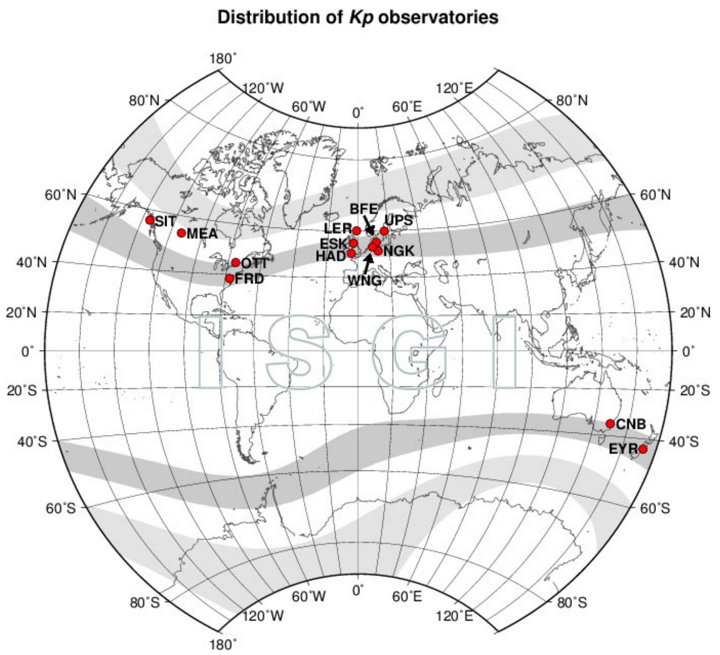

Figure 3.3 Distribution of the 13 *Kp* observatories. Courtesy of International Service of Geomagnetic Indices (ISGI), 2013.

To benefit from its higher precision, its scale, in the range 0–9 as well, is further divided into thirds, represented by the suffixes '+', 'o' and '−' (e.g., 3o, 3+, 4−, 4o). The *Kp* indices are often visualized in musical diagrams, where they are stacked into periods of 27 days to enable the detection of recurrent activities, as seen in Figure 3.4.

The *Kp* index can be converted to the 3-hour equivalent *ap* index, which represents the magnetic field strength at a surface position of about 50° dipole latitude. The conversion is done via a table defined by Bartels, in which the value of the *ap* index is scaled in units of 2 nT (see Table 3.1). There are further geomagnetic indices which are derived from the *Kp* index. They include Ap, the daily *ap* average, Cp, the daily *ap* sum mapped via a defined table to the range 0–2.5, and $C9$, a mapping of Cp via a defined table to the range 0–9. The definitions of Q-days (quiet days) and D-days (disturbed days) are also obtained from the *Kp* index.

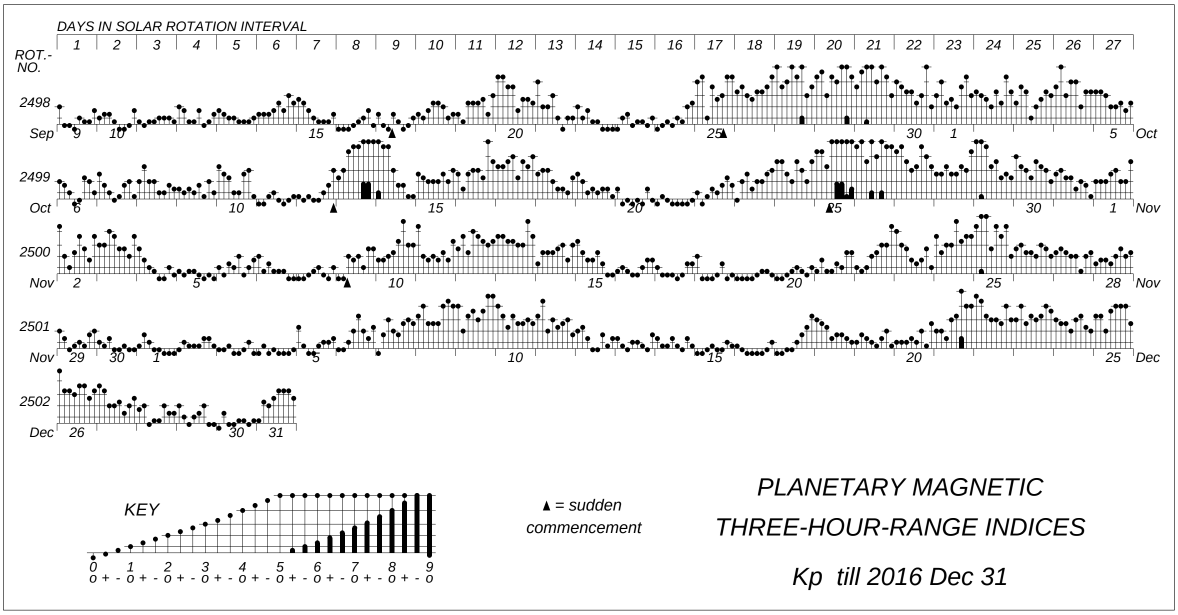

Figure 3.4 Bartels musical *Kp* diagram for the time period from September until end of December 2016. Two sudden commencements with following geomagnetic storms, having a maximal *Kp* of 6+, can be seen in October. Credit: GFZ Potsdam, 2017, licensed under CC BY 4.0.

The International Association of Geomagnetism and Aeronomy (IAGA) adopted the *Kp* index in 1954. The *Kp* index was maintained in Göttingen until January 1997 – now the German Research Centre for Geosciences (GFZ) in Potsdam supplies the *Kp* index and thereof derived indices. The GFZ provides historical and quick-look data of the indices via their website[1]. The data was extended backwards and is available from 1932 onwards.

Several indicators/quantities are based on the *Kp* index:
The NOAA G-Scale for geomagnetic storms (G 1 to G 5) is based on the *Kp* index[2].
The equatorward auroral boundary position correlates with the *Kp* index (cite?).
The variation of the total electron content (TEC) of the ionosphere correlates with the *Kp* index (cite?). The TEC has influence on global navigation satellite systems (GNSS). A part of their positional error scales directly with TEC (in extreme cases up to about 30 m).

Ït is designed to measure solar particle radiation by its magnetic effects."

Because of the effects on sensitive technical systems, methods for *Kp* forecasting are developed.
- Wing *Kp* model (link)
- Potsdam quicklook data (link)
- Alexej *Kp* correlation forecast model (link)
- In this work we derive relations for *Kp* nowcast from in-situ solar-wind measurements and *Kp* forecast from remote solar-wind stream/CME observations.

3.2.3 OMNI data set

see paper...

a data set merged from different sources
The OMNI data (King & Papitashvili 2005) were obtained from the GSFC/SPDF OMNIWeb interface.

from spacecraft located near the Lagrange point L1 upstream of Earth
time-shifted to the bow shock of the magnetosphere

[1]GFZ website for geomagnetic indices: `http://www.gfz-potsdam.de/de/kp-index/` (existent in 2017-10-29)
[2]NOAA Space Weather Scales website: `http://www.swpc.noaa.gov/noaa-scales-explanation` (existent in 2017-10-29)

OMNI2 H0 MRG1HR (1963–201308) Cite from CDAweb: Hourly near-Earth solar-wind magnetic field and plasma data, energetic proton fluxes (> 1 to > 60 MeV), and geomagnetic and solar activity indices.
NASA, Goddard Space Flight Center (GSFC), Space Physics Data Facility (SPDF): http://spdf.gsfc.nasa.gov/
- Coordinated Data Analysis Web (CDAWeb): http://cdaweb.gsfc.nasa.gov/
- OMNIWeb Plus: http://omniweb.gsfc.nasa.gov/

intercalibrated multi-spacecraft solar-wind data
Various spacecraft contribute to the interplanetary magnetic field (IMF) and solar-wind plasma OMNI data, as seen in Figure 3.5.

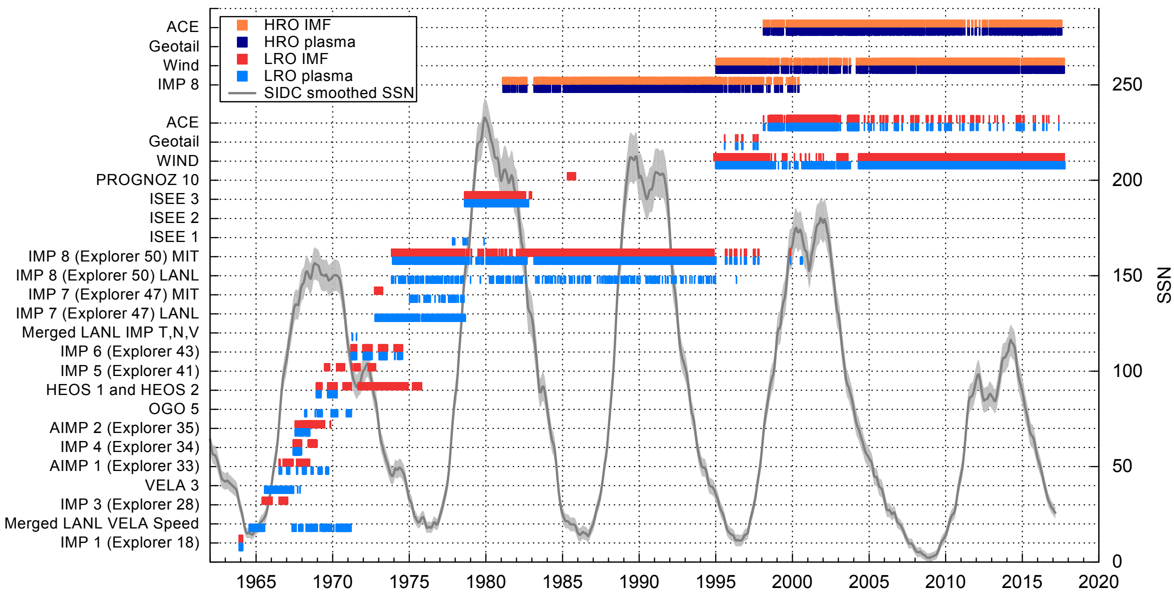

Figure 3.5 IMF and solar-wind plasma data source spacecraft for the high and the low resolution OMNI (HRO, LRO) data sets until end of 2016. The SIDC 13-month smoothed monthly SSN is plotted in the background. add cycle number...

Solar Wind Structures

Solar Wind Structures (SWS) list
derived by Richardson.... from OMNI data (only?) see chapter2...

permission received.

characterization of near-Earth solar-wind structures since 1963
SWS lists (Richardson et al. 2000) and (Richardson & Cane 2012)

3.2.4 Helios probes

see Helios data readme.txt
see paper

two different fluxgate magnetometers and a search coil magnetometer

see Figure 3.6
solar distance, HGI latitude and sunspot number during the Helios missions; see Figure 3.7

Helios 1 and 2 orbits in the ecliptic plane and in the latitude polar plane (see Figure 3.8)

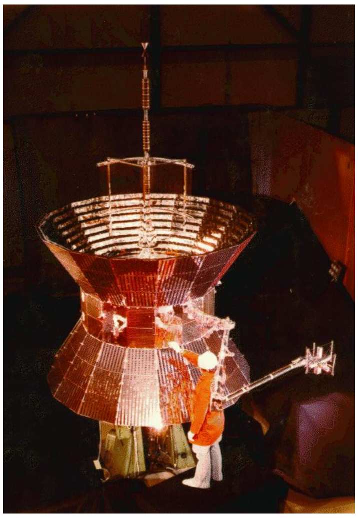

Figure 3.6 One of the nearly identical twin Helios spacecraft. Credit: NASA/Max Planck Institute for Solar System Research.

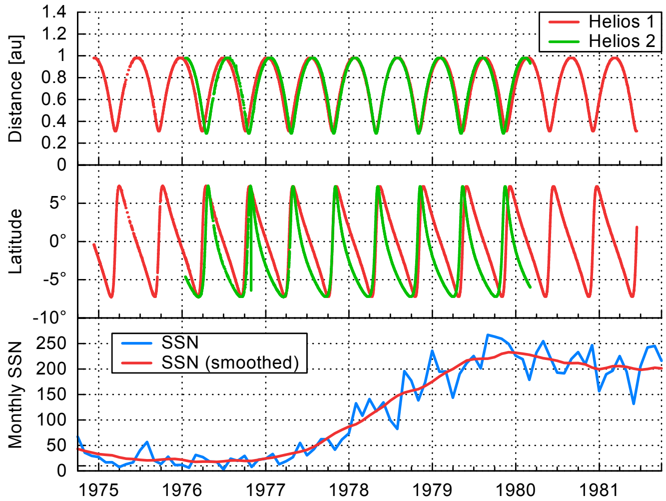

Figure 3.7 Plot of the Helios probes' solar distance and HGI latitude over their mission time, together with the monthly SSN and 13-month smoothed monthly SSN.

The Helios magnetic field and plasma data frequency over heliocentric distance and over heliographic latitude are plotted in Figure 3.9.

Solar wind data courtesy of R. Schwenn, Max-Planck-Institut für Aeronomie, Lindau, magnetic field data courtesy of F. Neubauer, Universität zu Köln. (see paper; into acknowledgements...)

data sources – see paper for replacing the following data
solar-wind parameters: ACE, Helios, OMNI
geomagnetic indices: Kp, OMNI

Space Physics Data Facility (SPDF)

HELIOS 1 and 2 - orbital Parameters
`http://spdf.sci.gsfc.nasa.gov/pub/data/helios/helios1/traj/`
`http://spdf.sci.gsfc.nasa.gov/pub/data/helios/helios2/traj/`

Helios hourly merged mag & plasma data:
HELIOS1_COHO1HR_MERGED_MAG_PLASMA_2965.txt
HELIOS2_COHO1HR_MERGED_MAG_PLASMA_3096.txt
`http://cdaweb.gsfc.nasa.gov`
temporal coverage of merged data
Helios 1: 1974-12-10 - 1981-06-14
Mag data availability: 42.6 %
Plasma & orbit data availability: 76.4 %
Helios 2: 1976-01-01 - 1980-03-04
Mag data availability: 54.4 %
Plasma & orbit data availability: 91.8 %

3.2.5 Real-time solar-wind data

Advanced Composition Explorer (ACE)
s/c figure, launch date was 25 August 1997

Wind, STEREO, SOHO, CELIAS

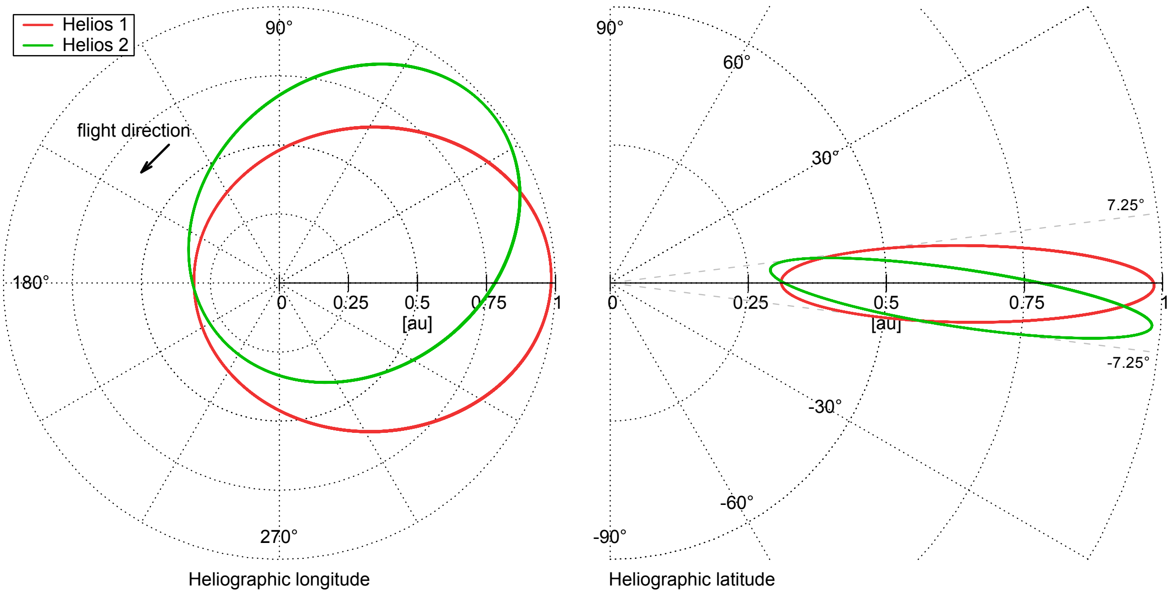

Figure 3.8 Orbits of the Helios 1 (red) and Helios 2 (green) spacecraft in the solar equatorial plane (left) and polar plane (right) (HGI-coordinates). change colors?

data errors/gaps...
Several services/alerts are based on the data streams from real-time measurements. (L1 alerts, etc.)

DSCOVR as replacement was launched on 11 Februar 2015. It is NOAA's SWPC real-time solar-wind prime source since 27 July 2016.[3]

[3] http://www.swpc.noaa.gov/products/real-time-solar-wind

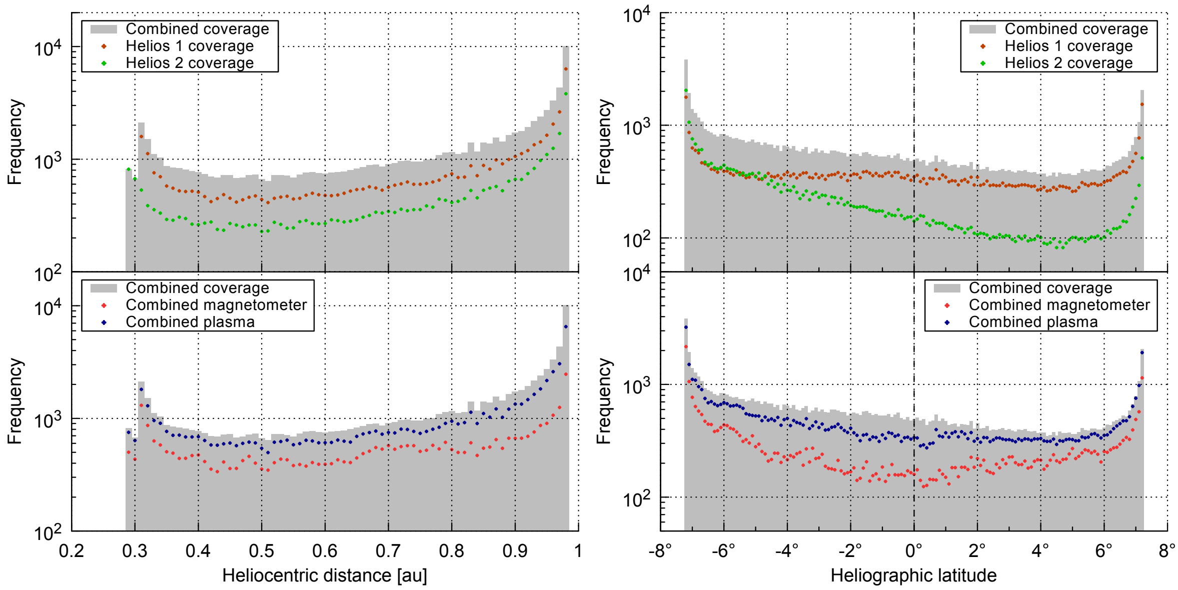

Figure 3.9 Helios data frequency over heliocentric distance with bins of 0.01 au (left panels) and over heliographic latitude with bins of 0.1° (right panels). The frequency data is based on the hourly merged magnetometer and plasma data sets for Helios 1 and Helios 2. The top panels show the frequencies for Helios 1 and Helios 2 individually and the bottom panels those for the magnetometer and plasma data. avoid white lines...

4 Solar wind and CME influence on the magnetosphere

Impact estimations derived from empirical correlations between in situ solar-wind measurements and the geomagnetic *Kp* index

Variations in the Earth's magnetosphere are largely evoked by influence through the solar wind. These magnetospheric disturbances have diverse effects on the terrestrial environment. Especially the effects of severe geomagnetic storms created by coronal mass ejections (CMEs) pose various threats to sensitive technical systems and exposed humans. Thus, the development of quantitative forecasts for magnetospheric impacts caused by solar wind and CMEs is very important.
This study's goals are to estimate the magnetospheric impact from solar activity in general, from solar wind and also to predict it for CMEs in particular. We present empirical dependencies between specific solar-wind parameters and the magnetospheric disturbance index *Kp*. These dependencies allow to nowcast the *Kp* index from upstream (L1) solar-wind in situ measurements. Hence, also the magnetospheric impact of CMEs is estimated solely based on their arrival velocities, predicted from coronagraphic observations. The prediction of solar-wind stream velocities from coronal hole (CH) observations, enables to estimate their impact as well.
First, we estimate the long-term variations of the yearly average *Kp* values, which are contributed by solar activity. This is achieved via logarithmic fitting of a yearly sunspot number (SSN) dependency. For the *Kp* nowcast from general solar-wind conditions, we use a correlation with the product of the parameters velocity and magnetic field z̃component in GSM coordinates (vB_z). For the *Kp* forecast from estimated CME and stream velocities, we furthermore filter the solar-wind data using flagged CME times from the solar-wind structures (SWS) list provided by Richardson & Cane (2012). The solar-wind data considered in our analyses consists of 35 years (1981–2016) of high-resolution minutely OMNI data, which is composed of multi-spacecraft intercalibrated in situ measurements from 1 au. We evaluate various data processing methods and choose the methods resulting in the highest correlation coefficients with *Kp*. We analyze the *Kp* frequency distributions with respect to the depending parameters vB_z and velocity, derive their mean *Kp* per interval and further compile functional dependencies via logarithmic fitting.
The obtained functional relations enable us to empirically estimate the mean *Kp* impact from measured solar activity, in situ solar wind, and remotely observed CHs and CMEs.

4.1 Introduction

It is long known (since the early 19th century) that variations in the solar wind evoke disturbances in the magnetosphere (Bartels 1962). Especially strong disturbances, called geomagnetic storms, can be provoked by coronal mass ejections (CMEs), which are embedded within the solar wind. The causes of the strongest geomagnetic storms are the compression of the solar-wind magnetic field lines within the CME shock front and the enhanced field strenghts of magnetic clouds, which are enclosed in CMEs (Bothmer 1993).

These strong geomagnetic disturbances are a threat to sensitive technical systems and exposed humans. Therefore it is important to know when magnetospheric disturbances will occur and how large they will become.

which index to use? - the *Kp* index is designed for...
More detailed information on the *Kp* index can be found in Section basics kp...

current comparable *Kp* forecast models take into account...
Elliott et al. (2013): The *Kp* index and solar-wind speed relationship: Insights for improving space weather forecasts

differences to existing studies:
here we show...
With our results presented here, we elaborate the step from the predicted CME and stream velocities to the forecast of the possible impact strength on the Earth's magnetosphere.
We make an empirical correlation of the solar-wind speed with the geomagnetic *Kp* index to obtain the capability to forecast *Kp* values solely based on the predicted CME and stream velocities.

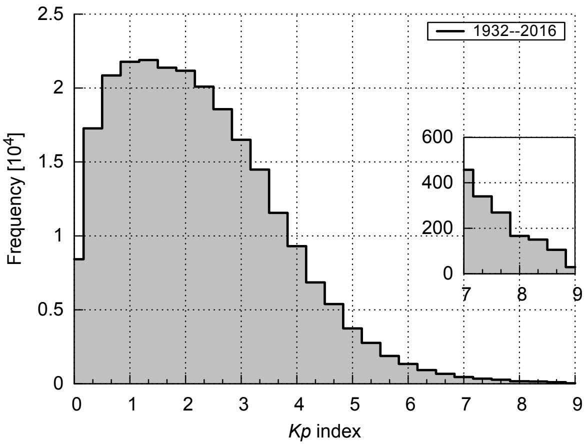

Figure 4.1 *Kp* frequency distribution for the time period 1932–2016. *Kp* data from the GFZ Potsdam.

The derived functional dependencies can be used to nowcast/forecast the *Kp* index.

In situ measurements of solar wind are made almost continuously (e.g., at the first Lagrange point (L1)) in front of the magnetosphere. Since 1963 several spacecraft collected more than 50 years of data. The latest spacecraft, e.g., Wind, ACE and DSCOVR (launched in early 2015), provide real-time solar-wind data online[1] [2] [3]. These solar-wind real-time data are used to nowcast various effects on the Earth's magnetosphere, e.g., the position of the magnetospheric bow shock in front of the Earth, the magnitude of geomagnetic disturbances (e.g., *Kp* index), the positions of the polar auroral ovals, the variation of the total electron content (TEC) of the ionosphere, and the positional error of global navigation satellite systems (GNSS).

Coronal holes are the origin of the fast solar wind; their area on the solar disk, seen in EUV wavelengths, correlates with the measured velocity of solar-wind streams (Vršnak et al. 2007). This relation is used to predict the Earth-arrival velocity of solar-wind streams about 4 days in advance (Rotter et al. 2012), as is done in real-time within the empirical solar wind forecast (ESWF) at the University of Graz[4].

The velocity and the direction of CMEs can be determined in their early near-Sun stages via remote tracking with coronagraph white-light observations. Using these parameters as input for CME propagation models, their possible arrival time and arrival velocity at Earth can be derived.

For the analyses performed and found in this paper, our objectives are to estimate the magnetospheric impact of solar wind and to predict it for CMEs in particular. In Sect. 4.2 we determine the magnitudes of the long-time *Kp* changes due to solar activity and measure the extent of seasonal variations stemming from the Earth's orbit. To nowcast the *Kp* index, we quantify the solar-wind influence on *Kp* by deriving a functional relation with the product of solar-wind velocity and magnetic field z-component (Sect. 4.3). Finally, to enable *Kp* forecasts from remote observations, we estimate the *Kp* impact coming from solar wind and CMEs separately by deriving functional dependencies with their velocities (Sect. 4.4).

4.2 Long-term variations of the *Kp* index

4.2.1 *Kp* data

The *Kp* data is obtained from the GFZ Potsdam[5], where the index is now maintained. The data used in this analysis covers the time period 1932–2016.

The *Kp* frequency distribution for the time period 1932–2016 shows that the highest frequencies occur around low *Kp* values of 1+ and to higher *Kp* values the frequencies seem to decline exponentially (see Fig. 4.1). A *Kp* value of 9o occurred only 29 times in this time interval.

[1]Wind real-time data website: https://pwg.gsfc.nasa.gov/windnrt/
[2]ACE real-time data website: http://www.swpc.noaa.gov/products/ace-real-time-solar-wind
[3]DSCOVR real-time data website: http://www.swpc.noaa.gov/products/real-time-solar-wind
[4]ESWF website: http://swe.uni-graz.at/index.php/services/solar-wind-forecast
[5]GFZ Potsdam website: http://www.gfz-potsdam.de/de/kp-index/

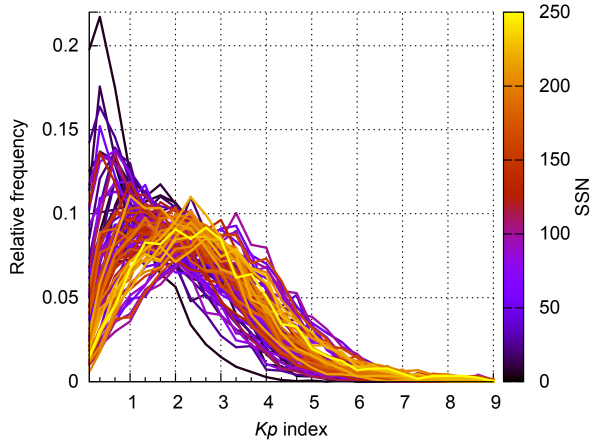

Figure 4.2 Yearly *Kp* frequency distributions of the period 1932–2016 sorted and colored by SSN. *Kp* data from the GFZ Potsdam and the yearly SSN from the SILSO World Data Center.

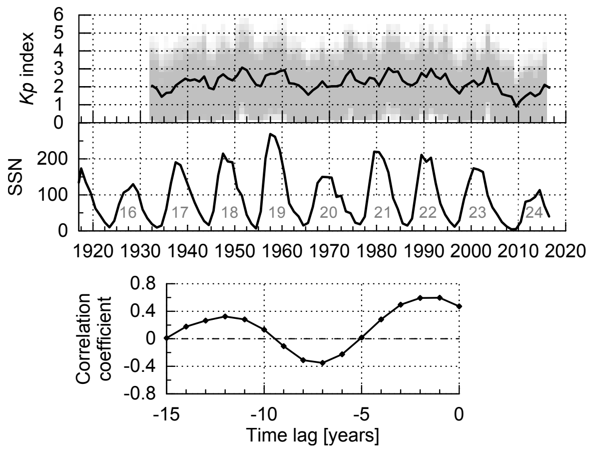

Figure 4.3 Yearly *Kp* index from GFZ Potsdam and yearly SSN from the SILSO World Data Center (1932–2016) with cycle number (top). The correlation coefficients with the yearly SSN are calculated for time lags back to -15 years (bottom).

4.2.2 *Kp* variations with solar activity

solar activity is tracked with the sunspot number (SSN); SSN data
The general *Kp* distribution, seen before in Fig. 4.1, averages over solar activity. With different states of solar activity the *Kp* frequency distributions' shape varies. This can be seen from the yearly distributions, sorted and colored by yearly SSN (see Fig. 4.2). The distribution's peak position scales with SSN, that is, a high yearly SSN results also in more large *Kp* values.

The time series of yearly average *Kp* values in the time span 1932–2016 shows an imprint of the solar cycles (see the top graphs in Fig. 4.3). The *Kp* pattern follows the solar cycle minima and maxima as well as the changes in magnitude between solar cycles. The yearly mean *Kp* shifts about 1 unit for both variations.

As expected, the *Kp* index correlation with solar activity shows an 11-year period (see bottom graph in Fig. 4.3). The highest correlation coefficient 0.60 is found with a time lag of -1 year, that is, the yearly average *Kp* follows the SSN of the previous year.

cause are CHs, see paper...

The yearly mean *Kp* indices with respect to the 1-year lagged SSN show a raise in *Kp* with increasing SSN, which is seen in Fig. 4.4.

We perform a fit to obtain an analytical relation for this dependency. *Kp* itself is a quasi-logarithmic index, so it is apparent to use a logarithmic fit function:

$$f(x) = a \cdot \ln(x) + b\,. \tag{4.1}$$

The fitted parameter values are $a = 0.281(43)$ and $b = 1.05(19)$ and lead to the relation

$$Kp(ssn) = 0.28 \cdot \ln(ssn) + 1.1\,. \tag{4.2}$$

In the fit result, plotted in Fig. 4.4, the mean *Kp* is 1.05(19) for a SSN of 1 and 2.53(30) for a SSN of 200. The fit error band has a width of about half a *Kp* unit.

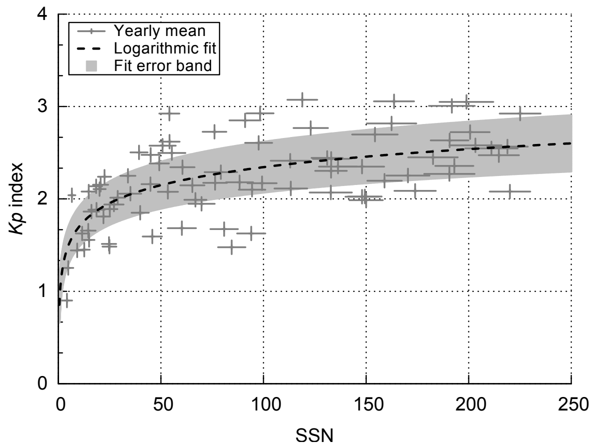

Figure 4.4 Yearly mean *Kp* index over 1-year lagged SSN (+) with the weighted logarithmic fit (dashed). The error bars denote the SSN standard deviation and the relative weight from the yearly data coverage. The shaded area represents the fit error band derived from the estimated standard deviations of the fit parameters. The function (4.1) is used for the weighted fit. The yearly *Kp* mean values are obtained from GFZ Potsdam data and the yearly SSN from the SILSO World Data Center.

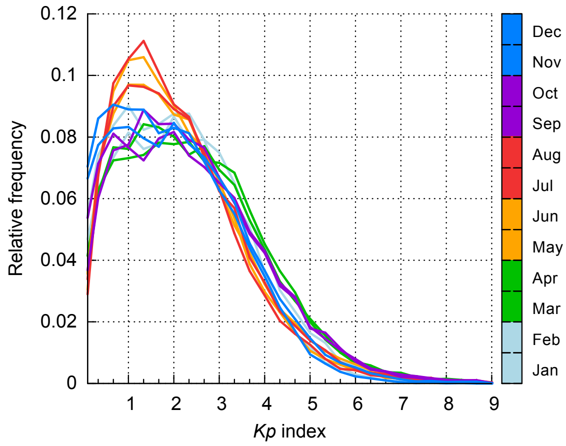

Figure 4.5 Monthly *Kp* frequency distributions colored by months of the year. *Kp* data of the time period 1932–2016 from the GFZ Potsdam.

4.2.3 Seasonal *Kp* variations

There also are seasonal variations in the magnetospheric disturbances. Looking at the monthly *Kp* frequency distributions for different seasons of the year, it is apparent that in the months May–August the *Kp* peak frequency is higher than in the rest of the year (see Fig. 4.5). In March/April and September/October the *Kp* values > 3 are more abundant.

These seasonal *Kp* changes arise from seasonal variations of the solar-wind parameters at Earth, which stem from Earth's yearly changes in orbital distance and heliographic latitude (as discussed in Sect. XX of MVVB-Paper). Another seasonal effect comes from the Earth's rotation axis tilt ($\pm 23.44°$) (obliquity to the ecliptic), which changes the direction of the Earth's magnetic dipole axis to the Sun over the year (see bottom panel of Fig. 4.6). The rate of magnetic reconnection between solar wind and magnetosphere depends on both fields' direction to each other (parallel/antiparallel) (see Figure in Basics...).

Kp seasonal variation effects from seasonal changing Sun tilt, Earth tilt and Earth distance.
causes (see citetRangarajan1997 p. 1282 and mention Bartels1963 too):
- Earth's rotation axis tilt ($\pm 23.44°$) (obliquity to orbit/inclination of equator)
- solar rotation axis tilt ($\pm 7.25°$) (cite 'NASA Earth fact sheet')
- Earth's varying solar distance of ± 1.67 %
read Bothmer1998 Ch 3...

We quantify the magnitude of these effects. *Kp* frequency distributions by month, see Fig. 4.6.
for high *Kp* values (> 4?) there are yearly frequency maxima at the equinoxes and minima at the solstices. this variation amounts to more than 1? *Kp* unit...

The magnitudes of the SSN variation $Kp(ssn)$ and the seasonal variation $Kp(\text{month})$ are of a similar order...?

Both variations are an indirect influence through solar wind (see paper).

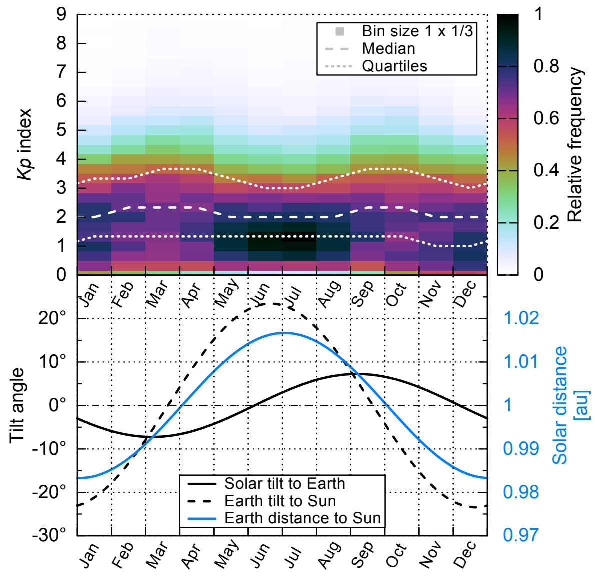

Figure 4.6 *Kp* frequency distributions by month for the time period 1932–2016 with median and quartile values (top). Solar tilt angle to Earth, Earth tilt angle to Sun and Earth distance to Sun are approximated with trigonometric fuctions (bottom). switch panels...

4.3 *Kp* nowcast from in situ solar-wind measurements

4.3.1 Solar wind-magnetosphere coupling

The coupling between the solar wind and the magnetosphere is governed by reconnection and compression of the magnetic field lines (see Basics...).

the dayside reconnection is asymmetric

To describe this, some coupling functions with different complexity were proposed (Newell, cites? and list).

dayside reconnection:
"E_y is the rate at which southward magnetic flux is convected to the magnetosphere by the solar wind ($-v_x \cdot B_z$) in GSM coordinates," (Russell 2007)

the product of the proton velocity v and the magnetic field z-component in geocentric solar magnetospheric (GSM) coordinates B_z:

$$?checkvectors E_y = -v_x \times B_z \,(\mathrm{GSM}) \tag{4.3}$$

If not specified otherwise, B_z is always meant to be in GSM coordinates hereafter.

argue for vB_z:
- 3hmin(vB_z) performs in rank correlation slightly better than the sophisticated Newell formula. really?
- simple to calculate
- ...

We settle for vB_z as the coupling function to analyze.

It also is known that the solar-wind velocity itself already correlates strongly with the *Kp* index. In fact Machol et al. (2013) even proposed a linear function of the *Kp* index as a best proxy for corrupted real-time velocity measurements made by the Advanced Composition Explorer (ACE) spacecraft.

4.3.2 Data set, data processing and correlation

The *Kp* time series started in 1932 when there were no spacecraft to measure in situ solar wind. Thus, the surveyed time range is defined by the available in situ solar-wind data. The OMNI data set collects the longest continuous solar-wind measurements at 1 au, it covers hourly data since 1963; 5-minute and minutely data

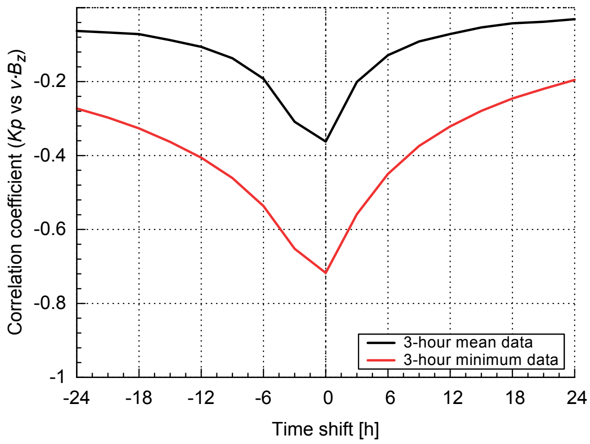

Figure 4.7 Kp-vB_z correlation coefficients for different time shifts. Minutely OMNI data from 1981–2016 processed with mean (black) and minimum (red) 3-hour averaging.

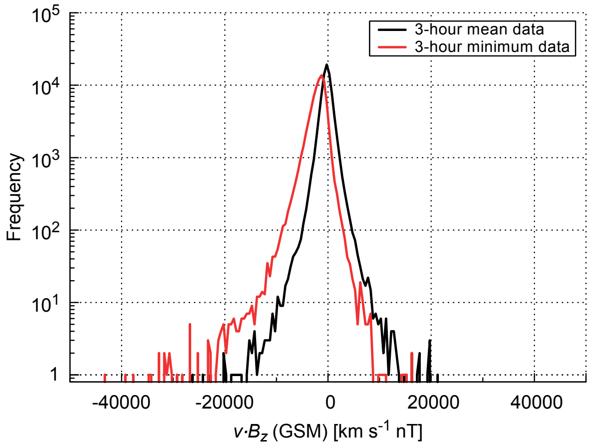

Figure 4.8 Frequency distributions of vB_z for 3-hour mean (black) and minimum (red) minutely OMNI data from 1981–2016.

since 1981.

why this data set? - because of long time coverage, to magnetospheric bow shock calculated solar wind and integrated geomagnetic indices (see Paper...)

The Kp index represents maximal variations within 3-hour time intervals. Any solar-wind parameter that will be correlated with it also has to have the same time resolution. Additionally to adapting the time resolution, we have to consider by which means it should be done. Simple 3-hour average values should have a lower correlation coefficient than the solar-wind parameter's 3-hourly maximal variation.

The 3-hour maximal variations are obviously higher when using high resolution data. Thus, to be able to correlate Kp with solar-wind data, high resolution data (e.g., 1 min) is needed to determine the maximal solar-wind variations within each 3-hour interval.

The longest time coverage has the hourly OMNI data set (since 1963), however we prefer to use the minutely OMNI data with the time range 1981–2016, to benefit from higer correlation coefficients (see Figs?).

Pearson correlation coefficients; use Spearman rank instead?
correlate positive and negative values separately?

Kp-vB_z Pearson correlation coefficients for mean and minimum, see Fig. 4.7.
The largest correlation is found for the 3-hour minimum data without time shift. It is a negative correlation with a coefficient of -0.72.

We use vB_z 3-hour minimum values, as a result their frequency distribution and its peak is asymmetrically shifted to negative values, as seen in Fig. 4.8.
even the 3-hour mean shows a slight offset in position (why?)

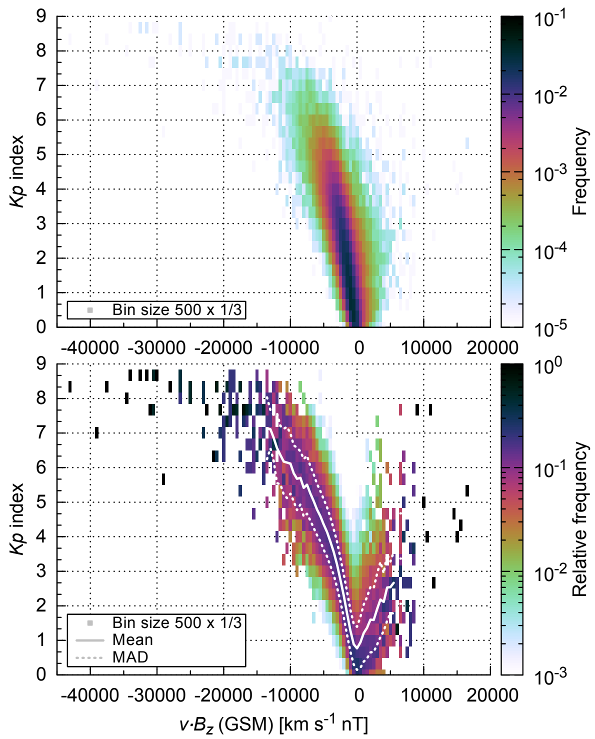

Figure 4.9 *Kp* versus vB_z frequency distribution (top) and its relative distribution (bottom) with the mean *Kp* values (solid) and their mean absolute deviation (dotted). It is 3-hour minimum data from the minutely OMNI data set (1981–2016). The bin size is 500 km s^{-1} nT and 1/3 *Kp* unit respectively.

4.3.3 Functional dependency

The frequency distribution over the *Kp*-vB_z space is shaped like a candle flame inclined to negative values by a light breeze, see top panel in Fig. 4.9.

To determine a functional dependency we look at the relative frequencies per vB_z-interval and their mean *Kp* values, which are plotted in the bottom panel of Fig. 4.9. The mean absolute deviation (MAD) of the mean has a mean size of 0.7 *Kp* units. This probability distribution is asymmetrically V-shaped around zero, having a larger and steeper negative arm. This effect is not a result of the data reducing method (3-hour minimum), because for 3-hour mean data the asymmetry also exists (fig...?). Rather the steeper negative arm is a consequence of the half-wave rectifier coupling of the solar-wind magnetic field direction to the magnetosphere as described in Sect (coupling section...).

Since the *Kp* index has a quasi-logarithmic scaling (see Basics...), a logarithmic function is the obvious choice as a fit function. Furthermore, the depending argument consists of a product of two solar-wind parameters which individually scale logarithmically with *Kp*. These reasons are why we use the logarithm of a parabola for the fitting approach:

$$f(x) = \ln(x^2)\,. \tag{4.4}$$

We introduce a horizontal shifting parameter $x2$ because the distribution's center is slightly offset. To be able to replicate the asymmetry in both arms, we split the fit function into a negative and a positive part:

$$f(x) = \begin{cases} f_-(x) & \text{for } x < 0\,, \\ f_+(x) & \text{for } x \geq 0\,. \end{cases} \tag{4.5}$$

This way both arms can be scaled individually with the scaling factors for the negative and positive parts a and c. The resulting logarithmic fit functions are

$$f_-(x) = a \cdot \ln((x + x2)^2 + d) + b\,, \tag{4.6}$$
$$f_+(x) = c \cdot (f_-(x) - f_-(-x2)) + f_-(-x2)\,, \tag{4.7}$$

with the vertical shifting parameter b and the depth parameter d.

The resulting fit is plotted in Fig. 4.10 with the fit coefficients $a = 1.258(19)$, $b = -17.04(33)$, $c = 0.467(20)$, $d = 1.416(68) \times 10^6$ and $x2 = 163(20)$ for units of [km s^{-1} nT].

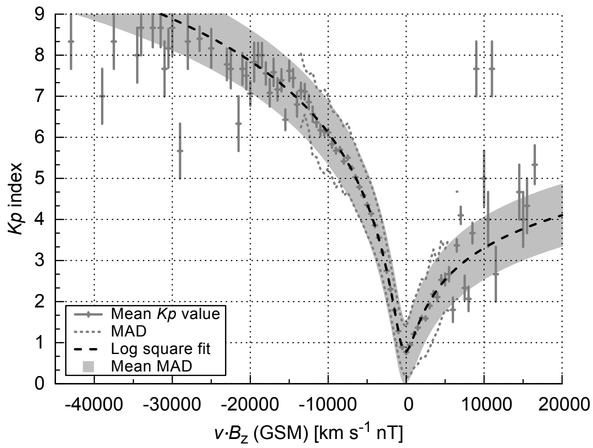

Figure 4.10 Mean *Kp* values (+) and MAD values (dotted) per vB_z interval. The error bars represent the relative data count. The logarithmic fit (dashed) is plotted with a mean MAD band (shaded area). The splitted function (4.5) is used for the weighted fit. OMNI data from the time period 1981–2016 is used.

Thus, the solar-wind dependency relation condenses to:

$$Kp_{-}(vB_z) = 1.26 \cdot \ln((vB_z + 160)^2 + 1.42 \times 10^6) - 17.0\,, \quad (4.8)$$

$$Kp_{+}(vB_z) = 0.47 \cdot (Kp_{-}(vB_z) - Kp_{-}(-160)) + Kp_{-}(-160)\,. \quad (4.9)$$

This relation can be used together with real-time in situ measurements from spacecraft located at L1 to nowcast the actual *Kp* index.

4.4 *Kp* forecast from remote CME observations

Compared to the steady solar wind, which can be measured reliably only from in situ measurements, CMEs can already be sighted raising from their source region on the solar surface. From remote coronagraph observations, some CME properties can be estimated and modeled to Earth, such as its propagation direction and its arrival time and arrival velocity (cites?). Thus, early observations enable a heads-up time only depending on the CME's propagation speed to Earth. This travel duration can be more than 4 days for slow events with average solar-wind speeds, about 40 hours for fast events with average speeds of 1000 km s^{-1}, and down to 20 hours and even below for the rare extreme cases, e.g., about 21 hours for the event on 23 July 2012 (Russell et al. 2013; Temmer & Nitta 2015) and about 19 hours for the event observed by Carrington (1859) on 1 September 1859.

To make use of the heads-up time for CMEs, we simplify the coupling relation (4.3) from before by neglecting its magnetic field part, which can hardly be determined from remote observations. Therefore, the only coupling parameter left is the solar-wind velocity.

4.4.1 CME velocity estimation

methods and modeling...?
GCS, CAD modeling -> propagation direction and apex height-time profile -> acceleration and velocity kinematics...
-> example event CME?

4.4.2 SWS CME list

For the following analysis we use the list of solar-wind structures (SWS) created and updated by Richardson et al. (2000); Richardson & Cane (2012), who characterized the near-Earth solar-wind structures since 1963. All periods related to ICMEs in the OMNI solar-wind data set were identified and flagged.

The SWS list for 1963–2016 was kindly provided by Ian Richardson (private communication). into acknowledgments...

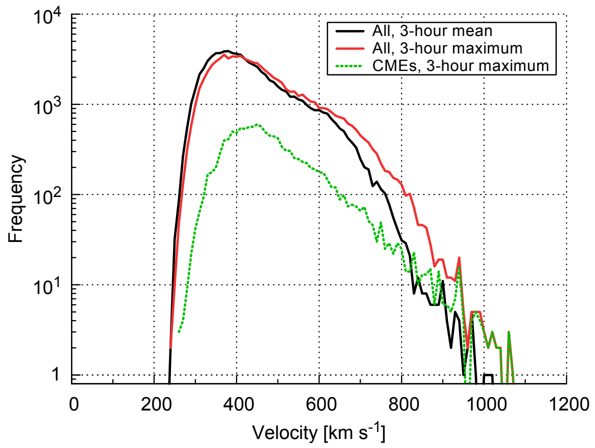

Figure 4.11 Solar wind velocity frequency distributions for 3-hour mean (black), maximum (red) and maximum of the CME part (green). Minutely OMNI data from the period 1981–2016 is used.

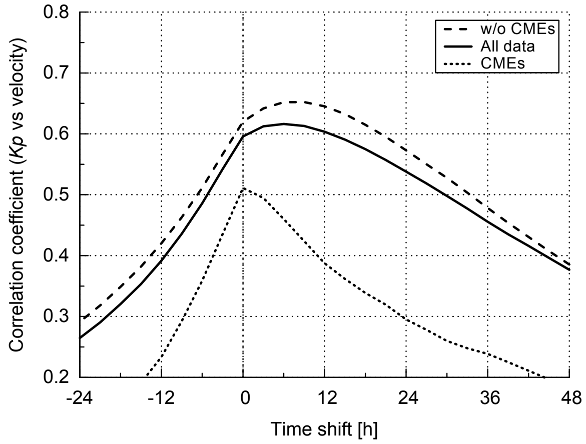

Figure 4.12 *Kp*-velocity correlation coefficients for different time shifts. The correlations for the whole solar-wind data (solid), for solar wind without CMEs (dashed) and for CMEs only (dotted) are plotted. The used data is the 3-hour maximum of the minutely high resolution OMNI data.

SWS list for 1963–2015 by (Richardson et al. 2000; Richardson & Cane 2012) is available via registration at CEDARweb[6].
List of near-Earth ICMEs since January 1996 by Cane & Richardson (2003); Richardson & Cane (2010). Available as ACE Level 3 data for the period 1995–mid2016[7].

The CME fraction of the OMNI time series for the period 1981–2016 is 15.8 % (5.53 years) and that for the period 1963–2016 is 17.0 % (9.01 years).

4.4.3 Data processing and correlation

Again we calculate 3-hour extreme values using the minutely OMNI data to profit from higher correlation coefficients, like done for the data processing of the vB_z analysis in Sect. 4.3.2. For the velocity these are 3-hour maximum values. The comparison between the 3-hour maximum and the 3-hour mean frequency distributions show that their mean position raises from 405 to 425 $\mathrm{km\,s^{-1}}$, see Fig. 4.11.

Using the CME periods from the SWS list as a filter, the CME part and non-CME part of the data can be examined separately. Their frequency distributions show that in faster solar wind the CME share is rising until eventually in the region above about 900 $\mathrm{km\,s^{-1}}$ there exist only CMEs, see Fig. 4.11.

The CME part of the data is correlated with the *Kp* index independently from the remaining solar wind, see Fig. 4.12. The correlation for CME related data is smaller than that for the regular solar wind. Its maximal correlation coefficient with a value of 0.51 is without time shift, see Table 4.1. The regular solar wind without CMEs shows a higher correlation with *Kp* and its maximal coefficient of 0.66 is at a positive time shift of 9 hours, that is, the *Kp* index forecasts the velocity of regular solar wind 9 hours in advance.

[6]CEDARweb website for Solar Wind Structures: http://cedarweb.vsp.ucar.edu/wiki/index.php/Tools_and_Models:Solar_Wind_Structures (existent in 2017-10-29)
[7]ACE Level 3 data website – list of near-Earth ICMEs: http://www.srl.caltech.edu/ACE/ASC/DATA/level3/icmetable2.htm (existent in 2017-10-29)

Table 4.1 Time lags with the highest correlation coefficients for the *Kp*-velocity relation. The used data is the 3-hour maximum of the minutely high resolution OMNI data.

Data	Time lag [hours]	Correlation coefficient
All data	6	0.622
w/o CMEs	9	0.661
CMEs	0	0.511

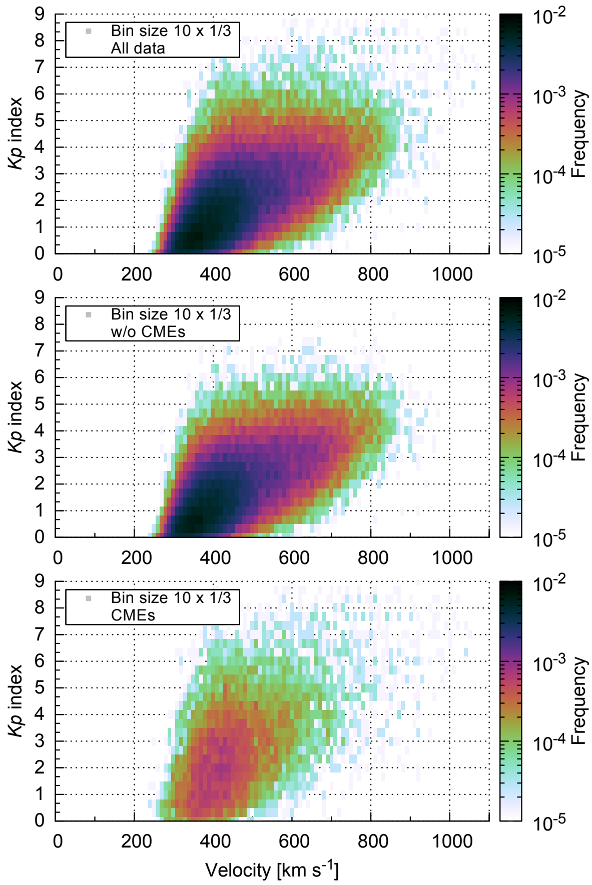

Figure 4.13 *Kp*-velocity distributions for the whole solar-wind data, for solar wind without CMEs and for CMEs only. The used data is the 3-hour maximum of the minutely high resolution OMNI data. For the CME separation the SWS list from Richardson & Cane (2012) is used. The bin size is $10\,\mathrm{km\,s^{-1}}$ and $1/3\,Kp$ unit respectively.

The positive time shift can be explained with the occurence of interaction regions followed by high speed streams (HSS). When a slow solar-wind stream is followed by a fast one, the compression at their interface leads to enhanced solar-wind densities and magnetic field strengths. The peak velocity of a HSS naturally appears after the interaction region. Therefore the *Kp*-impact of the enhanced magnetic field is correlated with the higher velocity of the HSS, yielding the observed positive time shift.

4.4.4 Functional dependency for CMEs

The general *Kp*-velocity dependency is apparent in the tilt of its distribution, see top panel of Fig. 4.13. The comparison with the CME data shows that *Kp* values > 7 and velocities $> 900\,\mathrm{km\,s^{-1}}$ are almost always associated with CME related periods, see middle and bottom panel of Fig. 4.13.

To find a functional dependency for the mean *Kp* value we look at the relative frequencies per velocity interval, which are plotted in the bottom panel of Fig. 4.14. The mean *Kp* value seems to scale almost linear with the solar-wind velocity. The mean absolute deviation of the mean has a mean size of about 1.1 *Kp* units.

Again, as the *Kp* index has a quasi-logarithmic scaling, a logarithmic function is the obvious choice for the fitting process, for which thus the logarithmic function

$$f(x) = a \cdot \ln(x + x1) + b \tag{4.10}$$

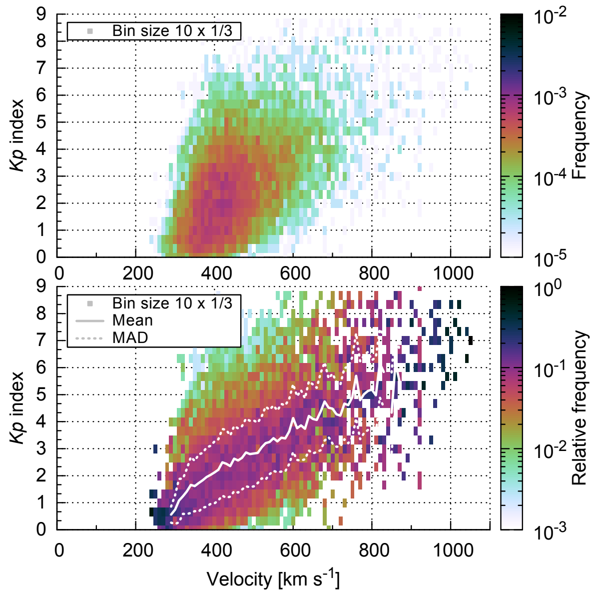

Figure 4.14 CME part of the *Kp*-velocity distribution (same as third panel of Fig. 4.13) and its relative distribution per velocity interval with the mean *Kp* values (solid) and their mean absolute deviation (dotted). The bin size is $10\,\mathrm{km\,s^{-1}}$ and $1/3\,Kp$ unit respectively.

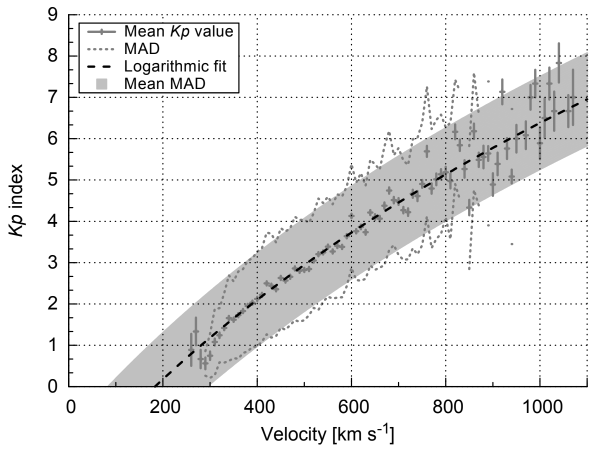

Figure 4.15 Mean *Kp* values (+) and MAD values (dotted) per velocity interval for the CME part of the data. The error bars represent the relative data count. The logarithmic fit (dashed) is plotted with a mean MAD band (shaded area). The function (4.10) is used for the weighted fit. The CME part of the OMNI data from the period 1981–2016 is obtained using the SWS list from Richardson & Cane (2012).

is used, with the scaling factor a, the location parameter $x1$ and the vertical shifting parameter b.

The resulting fit is plotted in Fig. 4.15, with velocity in units of $[\mathrm{km\,s^{-1}}]$ its parameters are $a = 10.6(34)$, $b = -73(28)$ and $x1 = 8.1(43) \times 10^2$.
This leads to the CME dependency function

$$Kp(v) = 11 \cdot \ln(v + 800) - 70\,, \tag{4.11}$$

which can be used to forecast the *Kp* index from the estimated CME arrival velocity.

4.4.5 Functional dependency for non-CMEs

use of by 9-hours shifted data..., see Fig. 4.12

To find a functional dependency for the mean *Kp* value we look at the relative frequencies per velocity interval, which are plotted in the bottom panel of Fig. 4.16. The mean *Kp* value seems to scale almost linear with the solar-wind velocity. The mean absolute deviation of the mean has a mean size of about 0.7 *Kp* units.

Again, as the *Kp* index has a quasi-logarithmic scaling, a logarithmic function is the obvious choice for the fitting process, for which thus the logarithmic function (4.10) is used.

The resulting fit is plotted in Fig. 4.17 and the fit parameters are $a = 5.88(38)$, $b = -3.70(29) \times 10^1$ and $x1 = 2.99(49) \times 10^2$, with velocity in units of $[\mathrm{km\,s^{-1}}]$.
This leads to the non-CME dependency function

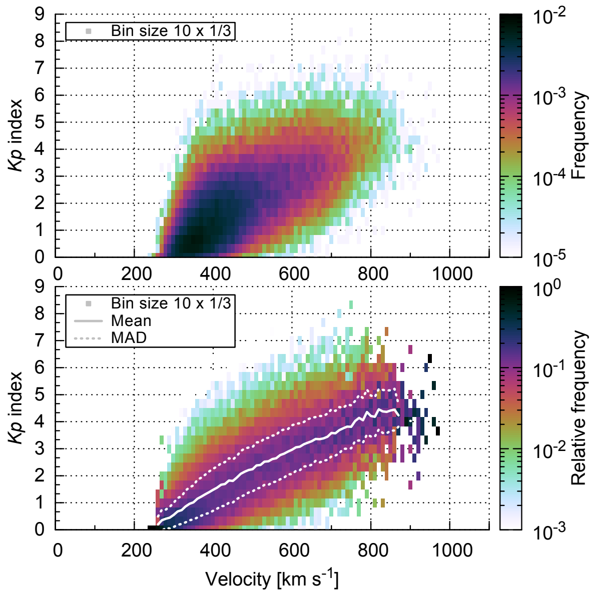

Figure 4.16 Non-CME part of the *Kp*-velocity distribution (similar to second panel of Fig. 4.13, but with the by 9-hours shifted data) and its relative distribution per velocity interval with the mean *Kp* values (solid) and their mean absolute deviation (dotted). The bin size is $10\,\mathrm{km\,s^{-1}}$ and $1/3\,Kp$ unit respectively.

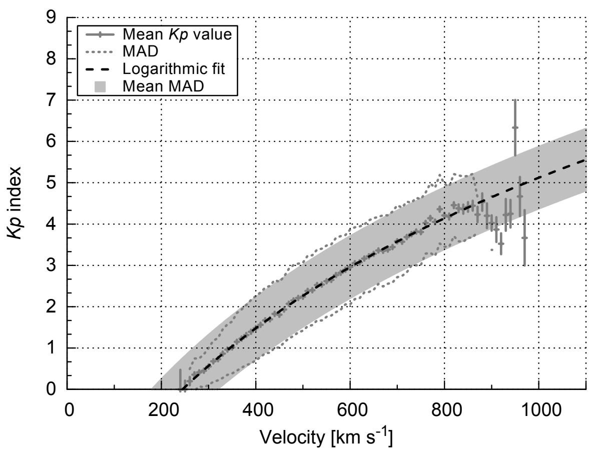

Figure 4.17 Mean *Kp* values (+) and MAD values (dotted) per velocity interval for the non-CME part of the data, shifted by 9-hours. The error bars represent the relative data count. The logarithmic fit (dashed) is plotted with a mean MAD band (shaded area). The function (4.10) is used for the weighted fit. The non-CME part of the OMNI data from the period 1981–2016 is obtained using the SWS list from Richardson & Cane (2012).

$$Kp(v) = 5.9 \cdot \ln(v + 300) - 37\,, \tag{4.12}$$

which can be used to forecast the Kp index from the estimated velocity coming from coronal hole analysis.

4.5 Results and discussion

solar activity: Kp-ssn relation
seasonal changes: Kp-month relation
solar-wind nowcast: Kp-vB_z relation (average and worst case)
CME forecast: Kp-velocity relation (average and worst case)
non-CME forecast: Kp-velocity relation (average and worst case)

Kp-velocity correlation
similar to Elliott et al. (2013); different data time period, resolution and averaging method (3-hour maximum of 1 min data)

4.6 Outlook

Applications:
Kp-rssfeed, realtime solar-wind and Kp plot
CME Kp impact (part of UGOE DDC)

scientists develop an advanced prototype space weather warning system to ensure the operation of telecommunication and navigation systems on Earth to the threat of solar storms

The prototype/precursor relations are integrated into applications developed within the Advanced Forecast For Ensuring Communications Through Space (AFFECTS) project which ran from 2011 to 2013. There are services accessible via the AFFECTS website[8].

list of services with Kp developed applications/implementations (all links existent in 2017-11-19):

- DSCOVR real-time solar-wind plot http://www.affects-fp7.eu/rssfeeds/ace_ap_plot/ace_realtime_ap_plot.png
- DSCOVR real-time solar-wind with Kp plot http://www.affects-fp7.eu/rssfeeds/ace_ap_plot/ace_realtime_ap_plot.png
- DSCOVR real-time solar-wind plot Kp forecast http://www.affects-fp7.eu/rssfeeds/ace_ap_forecast_plot/ace_realtime_ap_CH_GFT_plot.png
- RSS L1 SW Alert: http://www.affects-fp7.eu/rssfeeds/rssfeed_sw/rssfeed_sw.xml
- RSS L1 Kp Alert: http://www.affects-fp7.eu/rssfeeds/rssfeed_kp/rssfeed_kp.xml
- RSS L1 GNSS Alert: http://www.affects-fp7.eu/rssfeeds/rssfeed_gnss/rssfeed_gnss.xml
- RSS L1 Aurora Alert: http://www.affects-fp7.eu/rssfeeds/rssfeed_aurora/rssfeed_aurora.xml
- RSS L1 Aurora Alert (Kp 9): http://www.affects-fp7.eu/rssfeeds/rssfeed_aurora_kp9/rssfeed_aurora.xml
- iPhone app L1 Alerts (Solar wind latest 2-hour extreme values and derived forecast values): http://www.affects-fp7.eu/app-services/L1-Alerts/dataL1Alerts.txt
- Android app L1 Alerts...

[8] AFFECTS website (existent in 2017-11-19): http://www.affects-fp7.eu

- has SW-Display Kp forecast?
- CME *Kp* impact (part of UGOE DDC)
- Kp forecast calculation: http://www.astro.physik.uni-goettingen.de/~mvenzmer/kp_forecast_calculation/kp_forecast_calculation.php

mobile apps app store links?

reduce list to Kp-related apps...

4.7 Acknowledgments

The research leading to these results has received funding from the European Union's Seventh Framework Programme (FP7/2007-2013) under the grant agreement number 263506 (AFFECTS).
The authors thank the Helios and OMNI PIs/teams for creating and making available the solar wind in situ data. The OMNI data are supplied by the NASA Space Science Data Coordinated Archive (NSSDCA) and the Space Physics Data Facility (SPDF) at NASA's Goddard Space Flight Center (GSFC).
Additional thanks for maintaining and providing the international sunspot number series goes to the World Data Center – Sunspot Index and Long-term Solar Observations (WDC-SILSO) at the Solar Influences Data Analysis Center (SIDC), Royal Observatory of Belgium (ROB).
The hourly solar wind structure list was kindly provided by Ian Richardson of the NASA Goddard Space Flight Center and CRESST/University of Maryland via the CEDAR Database at the National Center for Atmospheric Research, which is supported by the National Science Foundation.
The results presented in this paper rely on the *Kp* index, calculated and made available by the German Research Centre for Geosciences in Potsdam from data collected at magnetic observatories. We thank the involved national institutes, the INTERMAGNET network and ISGI (isgi.unistra.fr).

5 notes to chapter2...

-> example events CIR/HSS and CME

5.1 Solar wind structure analyses

How strong do different structure types influence the terrestrial magnetosphere?
What kind of solar wind structures create the individual regions in this distribution?
What is their individual contribution to the Kp ranges (e.g. high Kp: CMEs 70% and CIRs 30%)?

ACE solar wind time series and event list
sw-timeseries ACE OPTIMAP "Zeitreihe"-events
method: automatic list creation by event detection via parameter thresholds...

sample CME analyses (MVA -> Kp)

5.2 Forecast

How can the impact field strength of CMEs be forecasted (V->B correlation for CMEs)?
Internal solar wind correlations:
B-V correlation
ACE MAGSWE 64 s data -> yearly overlay plot

applications:
rssfeeds, rtsw plots
CME Kp impact as part of DDC
- *Kp* nowcast with L1 solar wind measurements (L1 alerts, disseminated as RSS feeds; integrated in smartphone app and space weather display)
- Forecast of the possible CME impact on the Earth's magnetosphere (*Kp* index) from the predicted CME arrival velocity (integrated in UGOE CME forecast chain (aka DDC))

6 Empirical solar-wind model for the inner heliosphere

This chapter is constructed as follows, the PSP mission, scientific goals, and spacecraft are described, I introduce the analyses done in the publication Venzmer & Bothmer (2017), which belongs to this chapter, an improvement to the magnetic field solar distance dependency is derived, which deprecates that from the paper, other things, and further an outlook is given.

paper introduction and context of motivation in thesis and context of results in thesis

We obtained lognormal representations of the frequency distributions' shapes of the four key solar wind parameters magnetic field strength, proton velocity, density and temperature. We derived analytical relations for the parameters' solar activity dependencies and for their solar distance scaling. An empirical solar wind model was build from the combination of the obtained frequency distributions, SSN dependence relations and solar distance dependence functions, representing the solar wind's solar activity and distance behavior. This empirical model was fed with SSN predictions and extrapolated to the orbit of PSP. We estimated solar wind median values during PSP's first perihelion and modeled the values for PSP's closest perihelia.
- further investigations should be done into structure extrapolations
- outward extension of model seems feasable (e.g., to Mars)

In order to derive the solar wind environment for the PSP orbit, finally the general solar wind model derived in the previous sections will be extrapolated to the PSP orbit, taking into account predictions of the SSN.
varying shape with distance is indicator for internal physical processes (mixing/turbulence...)

The major part of this chapter is published in Venzmer & Bothmer (2017) ((replace arXiv cite with aanda's)). The paper, published in Astronomy and Astrophysics (A&A), is included following this chapter and **not yet** reproduced with permission © ESO.

The analyses described in the paper were entirely done by me, as well as the tables, figures and equations. My coauthor Volker Bothmer contributed to the text and the anonymous referee helped clarifying a few aspects. The text was further improved by the A&A language editor Joshua Neve.

6.1 Parker Solar Probe mission

include photo/picture
Sun angular diameter comparison, see presi S³

6.2 Solar distance dependency—theory

B-field radial profile: $B \propto r^{-1.5?}$
Magnetic field magnitude model (Kivelson 1995):
Br(r) = B0 / r²
Bphi(r) = -B0 omega / (Vr * r) (shear effect from solar rotation omega)
Btheta(r) = 0
B(r) = (Br² + Bphi² + Btheta²)**1/2
B(r) = sqrt((B0 / r²)² + (-B0 omega / (Vr * r))²) –> expected r dependency: B propto a*r**-2 + b*r**-1
Parker references
velocity radial profile: $V \propto r^{0?}$
model based on LeBlanc1998 electron density with flux conservation: Zic2015(Temmer)
density radial profile: $N \propto r^{-2}$
simple view: for a spherical constant velocity mass outflow a one over distance squared law is expected, because of the mass flux conservation per solid angle for different distances. measurements up to the outer heliosphere confirm the $1/r^2$ dependency (1–38 au by Voyager 2, (Belcher et al. 1993) newer paper?)

in an ideal neutral plasma the electron and proton number density have the same values (neutral plasma) (reference?)
ca. 10 % more electrons than protons (due to alphas) cite?
temperature radial profile: $T \propto r^{-1?}$
at larger distances heating outbalances the adiabatic temperature part (adiabatic cooling vs. pickup proton and stream–interaction heating; 1–68 au by Voyager 2; Richardson & Smith (2003)
solar wind ram pressure $p_{\mathrm{ram}} = \rho V^2$

6.3 Magnetic field strength solar distance dependency improvement

In our paper we scaled the magnetic field strength via a power-law function, obtaining a solar-distance dependency proportional to $r^{-1.662}$. We also noted there that the model's near-Sun field magnitude, extrapolated to PSP's closest perihelion, will be lower than the actual values to be found. However, this was a simplified approach – in the following I present a procedure leading to a distance dependency, which also accounts for the contributions of the individual vector components.

The coronal magnetic field near the Sun rigidly rotates, holding on to the coronal plasma. At the solar wind source surface (at around XX Rs), where the thermal plasma pressure overcomes the magnetic pressure, the magnetic field gets radially transported outwards, maintaining only its radial vector component $\boldsymbol{B}_r$. From there on, the solar rotation begins to shear the magnetic field, building up a longitudinal component $\boldsymbol{B}_\phi$ as well. The solar-wind magnetic field model, formulated by Parker (1958), has the following components in spherical coordinates (θ is the colatitude):

$$\boldsymbol{B}_r(r) = B_0 \left(\frac{r_0}{r}\right)^2 \cdot \boldsymbol{e}_r \,, \tag{6.1}$$

$$\boldsymbol{B}_\phi(r) = -B_0 \left(\frac{r_0}{r}\right)^2 \cdot \frac{\omega\, r\, \sin\theta}{v_{\mathrm{sw}}} \cdot \boldsymbol{e}_\phi \,, \tag{6.2}$$

$$\boldsymbol{B}_\theta(r) = 0 \cdot \boldsymbol{e}_\theta \,. \tag{6.3}$$

B_0 represents the radial field component at the solar distance r_0. The solar surface equatorial angular rotation rate ω and the solar wind velocity v_{sw} are involved as well.

From these equations it can be seen that $\boldsymbol{B}_r$ scales with r^{-2} with increasing solar distance, as it is expected for a spherical source and $\boldsymbol{B}_\phi$ scales with r^{-1}. From its absolute value

$$B(r) = \sqrt{\boldsymbol{B}_r^2 + \boldsymbol{B}_\phi^2 + \boldsymbol{B}_\theta^2}\,, \tag{6.4}$$

$$B(r) = \sqrt{\left(B_0 \left(\frac{r_0}{r}\right)^2\right)^2 + \left(-B_0 \left(\frac{r_0}{r}\right)^2 \cdot \frac{\omega\, r\, \sin\theta}{v_{\mathrm{sw}}}\right)^2}\,, \tag{6.5}$$

it is apparent that the magnetic field strength does not scale with a simple power law. A more accurate distance dependency for the model is derived in the following.

If the solar rotation axis tilt to the ecliptic normal is neglected and the radial field component B_0 is set to be in the ecliptic at $r_0 = 1$ au, then $\theta = 90°$ and

$$B(r) = B_0 \cdot \sqrt{r^{-4} + \left(\frac{\omega\, r}{v_{\mathrm{sw}}}\right)^2 r^{-4}}\,, \tag{6.6}$$

with the distance r in units of [au].

In the ecliptic at a distance of $r = 1$ au, the Parker spiral's observed magnetic field angle ϕ_B is centered most of the time at $-45°$ or in the opposite direction at $135°$. This is apparent from its frequency distribution, using OMNI data of the time period 1963–2016, see Figure 6.1.
The angle can be calculated via

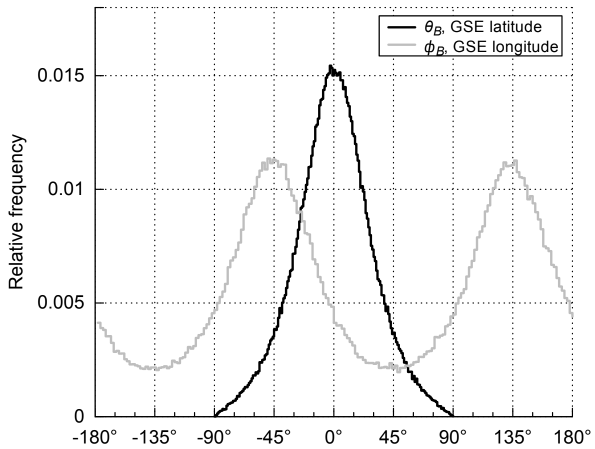

Figure 6.1 Frequency distributions of the magnetic field angles θ_B and ϕ_B in GSE coordinates. The frequencies are based on the hourly OMNI data during the period 1963–2016.

$$\phi_B(1\,\mathrm{au}) = \arctan\left(-\frac{\omega \cdot 1\,\mathrm{au}}{v_{\mathrm{sw}}} + 180°\right) . \tag{6.7}$$

With the mean values $\omega = 14.37\,°\,\mathrm{d}^{-1}$ (see appendix XX) and $v_{\mathrm{sw}} = 420\,\mathrm{km\,s^{-1}}$ (see paper) its value is: XX. use differential rotation rate $\omega_{\mathrm{d}}(\theta) =$ and assume equatorial field line origin at polar regions of ±60° heliolatitude (only valid at cycle minimum...).
This leads to an underwound Parker spiral (Banaszkiewicz et al. 1998).

For ϕ_B having these angles, both vector components B_r and B_ϕ have to be of equal length. We see from Equation 6.6 that it leads to

$$B(1\,\mathrm{au}) = B_0 \cdot \sqrt{2} \qquad \text{with} \qquad \left(\frac{\omega \cdot 1\,\mathrm{au}}{v_{\mathrm{sw}}}\right) = 1 . \tag{6.8}$$

This way, ω and v_{sw} are assumed to be constants - their time dependency is neglected.

$$B(r) = B_0 \cdot \sqrt{r^{-4} + r^{-2}} \text{ , for } \left(\frac{\omega}{v_{\mathrm{sw}}}\right) = 1 \tag{6.9}$$

$$B(1\,\mathrm{au}) = B_0 \cdot \sqrt{2} \tag{6.10}$$

fit function: $f(r) = a \cdot \sqrt{(r^{e_1})^2 + (r^{e_2})^2}$
expected r-dependency: $a \approx B(1au)/\sqrt{2}$, $e_1 \approx -2$, and $e_2 \approx -1$
fit function in Figure 6.2 and resulting fit parameters in Table 6.1

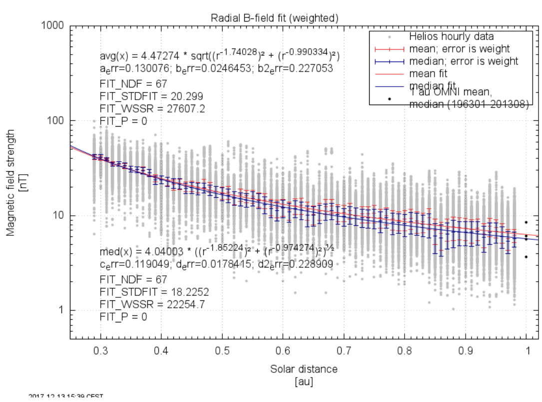

Figure 6.2 Helios hourly data plot of the magnetic field strength with respect to solar distance. The mean and median per 0.01 au data bin and their fit curves are plotted as well. The Helios data has a native distance resolution of 0.01 au, thus, to make the distribution visible in these plots, we added a random distance value of up to ±0.005 au.

Here, the WSSR is 6 %/9 % lower compared to the simple power law function a*r**b in Venzmer & Bothmer (2017).

we make a distribution fit. see fit distribution in Figure 6.3 and resulting fit parameters in table X.

Table 6.1 Fit parameters for the median and mean magnetic field strength solar distance relations and their crossing distance.

Fit		Factor a	Exponents e_1	Exponents e_2	Crossing distance [au]
Curve	Median	4.04(13)	-1.852(25)	-0.97(23)	0.33625(??)
	Mean	4.47(12)	-1.740(18)	-0.99(23)	
Distribution	Median	3.833(27)	-1.858(42)	-1.32(12)	–
	Mean	4.081(29)			

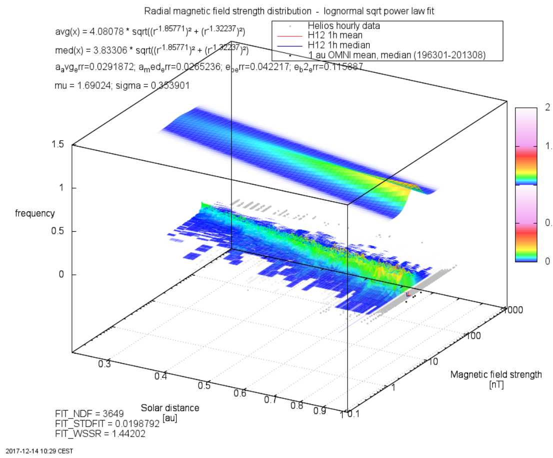

Figure 6.3 Frequency distribution of the solar wind magnetic field strength with respect to solar distance. Plotted are the binned Helios data and the square-root power-law lognormal fit model with its median value (white line). replace figure...

At 0.046 au the median value is 1267 nT – this is 33 % higher than the value in the paper.

scaling SSN-relation with the fit result: $B(ssn, r) = \frac{B(ssn)}{\sqrt{2}} \cdot \sqrt{(r^{e_1})^2 + (r^{e_2})^2}$

This result combined with the values obtained from the solar activity analysis in the paper is

$$B_{\text{med}}(ssn, r) = (0.0131\,\text{nT} \cdot ssn + 4.29\,\text{nT}) \cdot \sqrt{(r^{-1.86})^2 + (r^{-1.3})^2}\,, \tag{6.11}$$

$$B_{\text{avg}}(ssn, r) = 1.0879 \cdot B_{\text{med}}(ssn, r)\,. \tag{6.12}$$

extrapolation to the PSP orbital range, see Figure 6.4

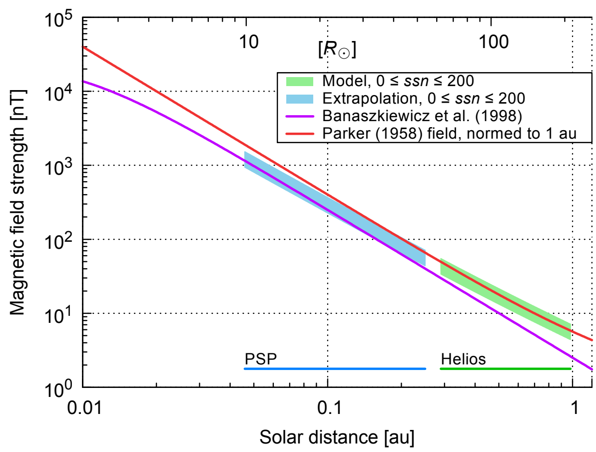

Figure 6.4 Radial extrapolation of the solar-wind magnetic field strength to the PSP orbit region. The median value from the model, obtained from Helios and OMNI measurements, is extrapolated to the PSP region for SSN values between solar minimum and maximum, that is, $0 \leq ssn \leq 200$. The lower edges of the shaded areas correspond to solar minimum, the upper edges to solar maximum. Also plotted are the radial dependencies of the analytic DQCS magnetic field model for solar minimum (violet) from Banaszkiewicz et al. (1998) and the Parker field model (red).

forecast to PSP orbit and mission time, see autoreffig:
extrapolation to the PSP orbital range, see Figure 6.5

The estimated magnetic field strength median value of 94 nT for the first perihelion is 8 % higher than that in the paper. However, the median value of 1241 nT for the first closest perihelion is 32 % higher.

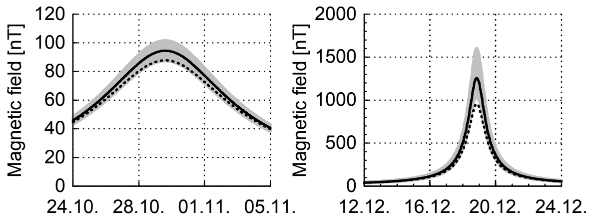

Figure 6.5 Estimated solar-wind parameter medians (solid) and their error bands (gray area) during 12 days in 2018 and 2024 with PSP's first perihelion at about 0.16 au and PSP's 22nd (the first closest) perihelion at 0.046 au. The prediction from Venzmer & Bothmer (2017) is indicated as well (dotted).

The estimated frequency distributions of the solar-wind magnetic field strength at PSP's 1st and 22nd (first closest) perihelion are plotted in Figure 6.6.

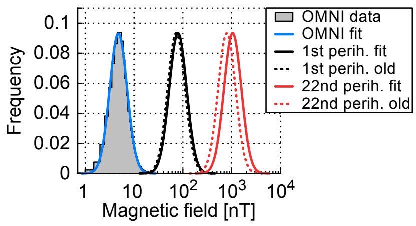

Figure 6.6 Frequency distributions of the solar-wind magnetic field strength (OMNI data) and those estimated with the solar-wind model for PSP's 1st and 22nd (first closest) perihelion. In these Figures the frequencies of both extrapolated curves are scaled for visibility to the same height as the 1 au distribution. The predictions from Venzmer & Bothmer (2017) are indicated as well (dotted).

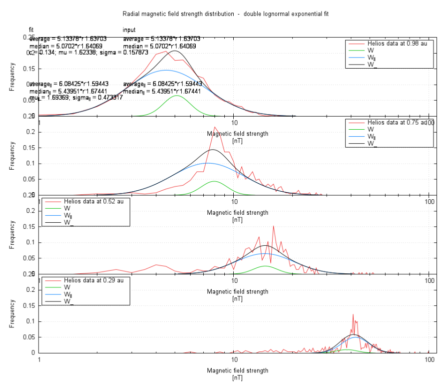

Figure 6.7 Plot of the magnetic field strength's frequency distribution at different solar distances (0.29, 0.52, 0.75 and 0.98 au). The Helios data, the composed fit model and both its components are plotted. 0.23 au steps, lw 2, stepfunction

=> what kind of distribution has the B-field near the Sun?

The result of this analysis is that the newly derived dependency relation can be used to replace and deprecate that found in the paper.

6.4 Outlook

Currently, the solar-wind model described in this chapter is purely empirical and its four solar-wind quantities are characterized independent from each other. Now in further steps, theoretical relations connecting the parameters could be introduced to make the model self-consistent. For example, flux conservation could be implemented into the radial distance dependencies, relating the two parameters density and velocity (see section XX), and also the velocity within the magnetic field's $\boldsymbol{B}_\phi$-component could be respected (not as a constant as is done in equation XX).

6.4.1 flux conservation

conserved quantities:
- momentum conservation... VBbookp112
- flux conservation...

With consideration of continuity the mass flux per solid angle has to be constant: $\dot{m}$ = const
conserved quantities:
- mass flux: $\dot{m} = \rho v A$ (with mass density ρ, velocity v and [cross-sectional area A] or solid angle?...)
- particle fluxes (proton flux, electron flux, etc.)
- proton flux: $j_\mathrm{p} = n_\mathrm{p} v_\mathrm{p} A$ (with proton density n_p and proton velocity v_p)

(with proton mass density $\rho = n_\mathrm{p} m_\mathrm{p}$ (with proton number density n_p and proton mass m_p).)

the individual radial dependencies for a spherical radial outflow are:
$A(r) \propto r^2$ –> A/r^2 = const
and assuming an exponential dependency,
$n_\mathrm{p}(r) = n_0 r^{c_n}$,
$v(r) = v_0 r^{c_v}$

$$
\begin{aligned}
j_\mathrm{p} &= \mathrm{const} && (6.13)\\
n_\mathrm{p} v_\mathrm{p} A &= \mathrm{const} && (6.14)\\
n_0 r^{c_n} v_0 r^{c_v} r^2 &= \mathrm{const} && (6.15)\\
r^{c_n} r^{c_v} r^2 &= \mathrm{const} && (6.16)\\
\Rightarrow c_n + c_v + 2 &= 0 && (6.17)\\
c_n + c_v &= -2 && (6.18)
\end{aligned}
$$

an increasing velocity should result in a steeper density...

validity of mass flux continuity: within the heliosphere mass to energy conversion and vice versa is negligible, but there can be flux from and to higher latitudes as the Helios data is localized to a small latitude range in the ecliptic plane.
estimate the error from that... (if error is too big => drop continuity condition)
larger errors should be located near CMEs and CIRs (nonradial flows from interactions)
there is a proton flux difference between slow and fast solar wind streams (see book Schwenn1990 p. 146)
estimate the possible size of error:
mean:
$c_n = -2.010$
$c_v = 0.049$
$c_n + c_v = -1.961$
difference to -2 is 0.039

6.5 Literature

Schwenn1983 intro -> sw-averaging comment (beer and wine)
see Hellinger2013 p.1353
see astro70/CGAUSS/dropbox_presis/... (presi 1.07 Inside Helios-Origins and Evolution-Salem.ppt -> Helios reloaded; radial functions for all parameters)
see Balogh1999 from p. 162 (Helios CIR results)

see Marsch1999... (model constraints)
model boundary condition: continuity of mass flux
On solar wind acceleration and SPP proposition: McComas2007
Parker1963 book, p. 75 -> isothermal expansion figure

Motivational question: What is the evolution of the solar wind parameters/structures before arriving at Earth? what is meant by the term evolution?

6.6 Seasonal solar wind variations

seasonal variation by month
quantify variation amplitudes

see Figure 6.8

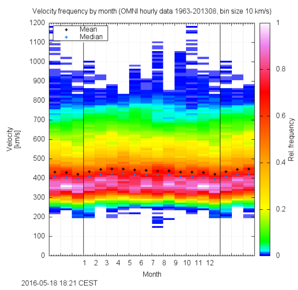

Figure 6.8 Diagram of the velocity frequency by month for the period 1963/01–2013/08. Mean and median values are shown as well.

see Figure 6.9

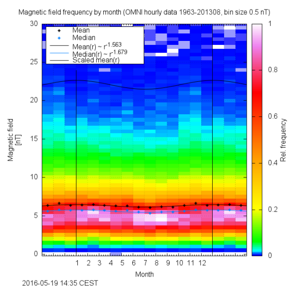

Figure 6.9 Diagram of magnetic field frequency by month for the period 1963/01–2013/08. Mean and median values are shown as well as the expected course from the solar distance variation (obtained from Helios data).

derived exponent values from simple trigonometric fit on monthly values:
$c_N = -2.234$
maybe figure?

expected influence from Earth's perihelion/aphelion (see Appendix...) distance vs observations
we expect for the proton density (scaling law $N(r) = 7.6\ \text{cm}^{-3} \cdot r^{-2}$):
N(0.983 au) = 7.9 cm^{-3}
N(1 au) = 7.6 cm^{-3}
N(1.017 au) = 7.3 cm^{-3}
we expect for the magnetic field strength (scaling law $\propto r^{-1.6}$):

B(0.983 au) = 6.3 nT
B(1 au) = 6.1 nT
B(1.017 au) = 5.9 nT

6.7 Latitude dependency

refer to Ulysses Figure 2.14
Ulysses swoops polar plots...

see Schwenn1990's Fig. 3.14
see also Schwenn (1990) p. 127
see also Richardson et al. (1995)
Balogh et al. (1999) p. 162 ff (origin and formation of CIRs in inner heliosphere with Helios data; latitude V dependence)

latitude; see Figure 6.10

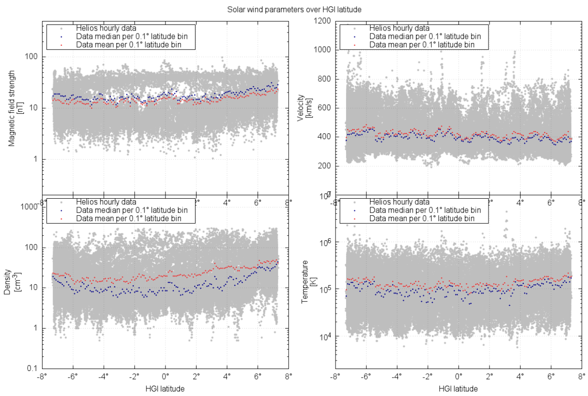

Figure 6.10 The four solar wind parameter's HGI latitude dependency. Their mean values per 0.1° bin are plotted as well. make figure same dimensions as projected figure in analysis part...

with the exponential dependencies to 1 au projected solar wind parameters; there are only small changes with latitude in the range −7.25–7.25°
have a look on distribution widths...

dependence from latitude in interval -7.25°–7.25° in Helios data negligible?, see Figure 6.11. estimate error

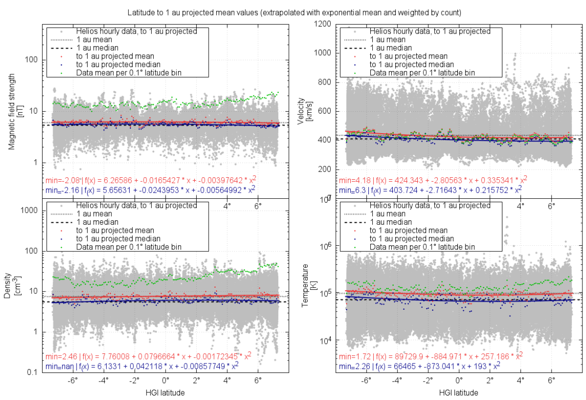

Figure 6.11 Plot of the to 1 au projected solar wind parameters over latitude. And their mean values, including weighted fit. add projected median...

ranges...

...plot Ulysses data into plot?

influence from latitude variation in data negligible? (see Ulysses Figure 2.14 in introduction). Helios probes within ecliptic => variation span equal to solar tilt: -7.25° to 7.25°; solar tilt/obliquity to ecliptic: $i_\odot = 7.25°$ (Sun fact sheet: `http://nssdc.gsfc.nasa.gov/planetary/factsheet/sunfact.html)`
big part of Helios data is from latitudes > ±5°, see Figure XX (data count over latitude) and see Figure 3.8 (Helios orbit polar plane in data section)

6.8 Radial evolution of solar wind structures

Helios event lists HSSs, SLOWs, CIRs, CMEs...; event lists for all Helios data
see Liu2004 for Helios ICME list and radial dependencies of B, n, T and v...

200 km s^{-1} slow solar wind at 10 $R_\odot$ is in agreement with blob measurements from Wang2000

very slow sw (VSSW) gets accelerated; see Sanchez-Diaz2016:

radial diameter of MCs increase between 0.3 au and 4.3 au proportional to the distance as $r^{0.8}$ (Bothmer & Schwenn 1998)
MC central axial magnetic field strength radial density dependence $B = 18.1\, r^{-1.64}$ Leitner et al. (2007)
MC average diameter $D = 0.23\, r^{1.14}$ Leitner et al. (2007)
sw structure marked plots

structure extrapolations

6.9 sw parameters and precision

definition of 'the four solar wind parameters':
magnetic field strength, aka magnetic field, B, usually measured in nT, in the order of 0–35 nT at 1 au
proton bulk velocity, aka velocity, v, usually measured in km/s, in the order of 200–900 km/s at 1 au
proton number density, aka density, n, usually measured in cm^{-3}, in the order of 1–60 at 1 au
proton temperature, aka temperature, T, usually measured in K, in the order of 10 000–1 000 000 K at 1 au
sentence about ordering of the parameters...

hourly OMNI data
measurement precision:
B: 0.01 nT
v: 1 km/s
n: 0.1 cm^{-3}
T: 1 K ? (smallest found: 7 K)

error discussion:
OMNI hourly data mean:
B: bin size 0.5 nT, median 5.6, mean 6.30056(18)
v: bin size 10 km/s, median 414, mean 437.6700(18)
n: bin size 1 cm^{-3}, median 5.3, mean 6.831410(18)
T: bin size 10 000 K, median 80 751, mean 112 219.0(19) (with 1000 K as precision)

empirical data; Helios; hourly
why hourly and not higher resolution data?
measurement precision:
B: 0.01 nT
v: 0.1 km/s
n: 0.1 cm^{-3}
T: 100–1000 K (3 digits)

r: 0.01 au

error discussion:
Helios hourly data mean:
B: min 337, precision: 0.000545; 18.3x better
v: min 497, precision: 0.00449; 22.2x
n: min 497, precision: 0.00449; 22.2x
T: min 497, precision: 4.49–44.49 22.2x
=> so we use 1/10 the measurement precicion for the mean.

median precision same as data precision

Helios histogram bin size for mean of frequency distribution (at specific solar distance)
B: bin size 0.5 nT, min 337, mean precision: 0.000545
v: bin size 1 cm^{-3}, min 497, mean precision: 0.00449
n: bin size 10 km/s, min 497, mean precision: 0.00449
T: bin size 10 000 K, min 497, mean precision: 4.49–44.49

6.10 other

McGregor2011 analyzed the empirical magnetic topology–velocity relationship, using Helios perihelion data with the Wang-Sheeley-Arge (WSA) coronal model, and found indications, that the fast and slow solar wind are generated from distinct sources. (not only superradial expansion)

Concerning the error notation I adhere to the parentheses notation documented in the “Guide to the expression of uncertainty in measurement” (GUM) published by Joint Committee for Guides in Metrology (2008), where the numbers in parentheses are the errors on the corresponding last digits of the quoted value.

For more on lognormal distributions see appendix section B.2

The extrapolation distance is only about one third of the model range, but as the parameters follow exponential change, one has to look at the logarithmic distance which is indeed one and a half times the model range.

replace paper with actual published A&A version...

Solar-wind predictions for the Parker Solar Probe orbit

Near-Sun extrapolations derived from an empirical solar-wind model based on Helios and OMNI observations

M. S. Venzmer and V. Bothmer

University of Goettingen, Institute for Astrophysics, Friedrich-Hund-Platz 1, 37077 Göttingen, Germany

Received 25 August 2017; accepted 10 November 2017

ABSTRACT

Context. The Parker Solar Probe (PSP) (formerly Solar Probe Plus) mission will be humanity's first in situ exploration of the solar corona with closest perihelia at 9.86 solar radii ($R_\odot$) distance to the Sun. It will help answer hitherto unresolved questions on the heating of the solar corona and the source and acceleration of the solar wind and solar energetic particles. The scope of this study is to model the solar-wind environment for PSP's unprecedented distances in its prime mission phase during the years 2018–2025. The study is performed within the Coronagraphic German And US SolarProbePlus Survey (CGAUSS) which is the German contribution to the PSP mission as part of the Wide-field Imager for Solar PRobe (WISPR).

Aims. We present an empirical solar-wind model for the inner heliosphere which is derived from OMNI and Helios data. The German-US space probes Helios 1 and Helios 2 flew in the 1970s and observed solar wind in the ecliptic within heliocentric distances of 0.29–0.98 au. The OMNI database consists of multi-spacecraft intercalibrated in situ data obtained near 1 au over more than five solar cycles. The international sunspot number (SSN) and its predictions are used to derive dependencies of the major solar-wind parameters on solar activity and to forecast their properties for the PSP mission.

Methods. The frequency distributions for the solar-wind key parameters, magnetic field strength, proton velocity, density, and temperature, are represented by lognormal functions. In addition, we consider the velocity distribution's bi-componental shape, consisting of a slower and a faster part. Functional relations to solar activity are compiled with use of the OMNI data by correlating and fitting the frequency distributions with the SSN. Further, based on the combined data set from both Helios probes, the parameters' frequency distributions are fitted with respect to solar distance to obtain power law dependencies. Thus an empirical solar-wind model for the inner heliosphere confined to the ecliptic region is derived, accounting for solar activity and for solar distance through adequate shifts of the lognormal distributions. Finally, the inclusion of SSN predictions and the extrapolation down to PSP's perihelion region enables us to estimate the solar-wind environment for PSP's planned trajectory during its mission duration.

Results. The CGAUSS empirical solar-wind model for PSP yields dependencies on solar activity and solar distance for the solar-wind parameters' frequency distributions. The estimated solar-wind median values for PSP's first perihelion in 2018 at a solar distance of 0.16 au are 87 nT, 340 km s^{-1}, 214 cm^{-3} and 503 000 K. The estimates for PSP's first closest perihelion, occurring in 2024 at 0.046 au (9.86 $R_\odot$), are 943 nT, 290 km s^{-1}, 2951 cm^{-3}, and 1 930 000 K. Since the modeled velocity and temperature values below approximately 20 $R_\odot$ appear overestimated in comparison with existing observations, this suggests that PSP will directly measure solar-wind acceleration and heating processes below 20 $R_\odot$ as planned.

Key words. solar wind – sun: heliosphere – sun: corona

1. Introduction

From observations of cometary tail fluctuations, Biermann (1951) inferred the presence of a continuous flow of particles from the Sun. With his theoretical solar-wind model, Parker (1958) formulated the existence of the solar wind even before the first satellites measured it in situ in 1959 (Gringauz et al. 1960; Neugebauer & Snyder 1966). The idea of a space mission flying through the solar corona dates back to the founding year of NASA in 1958 (McComas et al. 2008). Since then several space missions have measured the solar wind in situ at a wide range of heliocentric distances. In the case of Voyager 1, this was as far away as 140 au[1] in October 2017, having crossed the heliospause into interstellar space at a distance of 121 au (Gurnett et al. 2013). Various spacecraft have provided a wealth of solar-wind measurements near Earth's orbit, with WIND (Lepping et al. 1995; Ogilvie et al. 1995), SOHO (Domingo et al. 1995), ACE (Stone et al. 1998) and DSCOVR (Burt & Smith 2012) currently providing observations while orbiting around the L1 point 1.5 million km ahead of Earth in the sunward direction. Additional measurements at other solar distances were provided by planetary missions to Venus and Mercury, such as PVO (Colin 1980) or MESSENGER (Belcher et al. 1991). Ulysses was the first probe that orbited the Sun out of the ecliptic plane and thus could measure solar wind even at polar latitudes (McComas et al. 1998). The in situ solar-wind measurements closest to the Sun to date were made by the Helios missions. Helios 1, launched in 1974, reached distances of 0.31 au. Helios 2, launched two years later, approached the Sun as close as 0.29 au (Rosenbauer et al. 1977). The NASA Parker Solar Probe[2] (PSP), formerly Solar Probe Plus, six years after its planned launch date in mid 2018, will reach its closest perihelia at a distance of 9.86 solar radii ($R_\odot$), that is, 0.0459 au (Fox et al. 2015). This distance will

[1] https://voyager.jpl.nasa.gov/

[2] http://parkersolarprobe.jhuapl.edu/

be achieved through seven Venus gravity assists with orbital periods of 88–168 days. In its prime mission time 2018–2025 PSP provides 24 orbits with perihelia inside 0.25 au (Fox et al. 2015). Even its first perihelion, 93 days after launch in 2018, will take PSP to an unprecedented distance of 0.16 au (35.7 $R_\odot$). In comparison, the ESA Solar Orbiter mission with a planned launch in February 2019 will have its closest perihelia at 0.28 au (Müller et al. 2013).

The key PSP science objectives are to "trace the flow of energy that heats and accelerates the solar corona and solar wind, determine the structure and dynamics of the plasma and magnetic fields at the sources of the solar wind, and explore mechanisms that accelerate and transport energetic particles" as stated in Fox et al. (2015). To achieve these goals, PSP has four scientific instruments on board: FIELDS for the measurement of magnetic fields and AC/DC electric fields (Bale et al. 2016), SWEAP for the measurement of flux of electrons, protons and alphas (Kasper et al. 2016), IS⊙IS for the measurement of solar energetic particles (SEPs) (McComas et al. 2016) and WISPR for the measurement of coronal and inner heliospheric structures (Vourlidas et al. 2016).

The study presented in this paper is undertaken in the Coronagraphic German And US SolarProbePlus Survey (CGAUSS) project, which is the German contribution to the PSP mission as part of the Wide-field Imager for Solar PRobe (WISPR). WISPR will contribute to the PSP science goals by deriving the three-dimensional structure of the solar corona through which the in situ measurements are made to determine the sources of the solar wind. It will provide density power spectra over a wide range of structures (e.g., streamers, pseudostreamers and equatorial coronal holes) for determining the roles of turbulence, waves, and pressure-balanced structures in the solar wind. It will also measure the physical properties, such as speed and density jumps of SEP-producing shocks and their coronal mass ejection (CME) drivers as they evolve in the corona and inner heliosphere (Vourlidas et al. 2016). In order to help optimize the WISPR and PSP preplanning of the science operations, knowledge of the expected solar-wind environment is needed. For this purpose the solar-wind environment is extrapolated down to the closest perihelion of 9.86 $R_\odot$ distance to the Sun using in situ solar-wind data from the Helios probes and near 1 au data from various satellites compiled in the OMNI solar-wind database.

Generally, two types of solar wind are observed in the heliosphere – slow and fast streams (Neugebauer & Snyder 1966; Schwenn 1983). Slow solar wind has typical speeds of <400 km s^{-1} and fast solar wind has speeds >600 km s^{-1} (Schwenn 1990, p. 144). Their different compositions and characteristics indicate different sources and generation processes (McGregor et al. 2011b). Fast streams are found to originate from coronal holes as confirmed by Ulysses' out-of-ecliptic measurements (McComas et al. 1998). The source of slow wind, and its eventually different types (Schwenn 1983), is still a subject of controversial discussions because several scenarios are possible to explain its origin from closed magnetic structures in the solar corona, such as intermittent reconnection at the top of helmet streamers and from coronal hole boundaries (Kilpua et al. 2016). The occurrence frequency of these slow and fast streams varies strongly with solar activity and their interactions lead to phenomena such as stream interaction regions which may persist for many solar rotations ("co-rotating" interaction regions) if the coronal source regions are quasi-stationary (Balogh et al. 1999). Embedded in the slow and fast solar-wind streams are transient flows of CMEs – the faster ones driving shock waves ahead (Gosling et al. 1974). Their rate follows the solar activity cycle and varies in near 1 au measurements between only one CME every couple of days during solar cycle minima up to multiple CMEs observed over several days at times of solar maxima, that is, the CME-associated flow share of the solar wind raises from about 5 % up to about 50 % (Richardson & Cane 2012).

It is not known which specific solar-wind type or structure PSP will encounter at a given time during its mission, therefore we extrapolate the probability distributions of the major solar-wind parameters from existing solar-wind measurements and take solar cycle dependencies into account. As a baseline we describe the solar-wind environment through the key quantities of a magnetized plasma: magnetic field strength, density and temperature. Furthermore, the bulk flow velocity is the defining parameter of the two types of solar wind. Solar-wind quantities, like flux densities, mass flux, and plasma beta, can be directly derived from these four parameters. In the analyses, we treat the solar wind as a proton plasma – the average helium abundance is about 4.5 % and in slow wind at solar cycle minimum is even less than 2 % (Feldman et al. 1978; Schwenn 1983; Kasper et al. 2012).

Our approach is to obtain analytical representations of the shapes of the solar-wind parameter's frequency distributions in Sect. 2, of their solar activity dependence in Sect. 3 and of their solar distance scaling in Sect. 4. The solar-wind parameters' frequency distributions and solar activity dependence is derived from near-Earth solar wind and sunspot number (SSN) time series with a duration of almost five solar cycles. Their distance dependency is derived from Helios solar-wind measurements covering more than two thirds of the distance to the Sun and more than half a solar cycle. From a combination of the obtained frequency distributions, SSN dependence functions, and solar distance dependence functions, a general solar-wind model is built in Sect. 5, representing the solar activity and distance behavior. Finally, this empirical model is fed with SSN predictions and extrapolated to PSP's planned orbital positions in Sect. 6.

2. Frequency distributions of the solar-wind parameters

The solar-wind parameters are highly variable due to short-term variations from structures such as slow and fast wind streams, interaction regions, and CMEs, whose rate and properties depend on the phase of the solar activity cycle. Hence, for deriving characteristic frequency distributions for the solar-wind parameters, measurements over long-term time spans are needed. The abundance of the near-Earth hourly OMNI data set is ideally suited for this purpose, because to date it spans almost five solar cycles.

The OMNI 2 data set (King & Papitashvili 2005) combines solar-wind magnetic field and plasma data collected by various satellites since 1963, currently by WIND and by ACE. This intercalibrated multi-spacecraft data is time-shifted to the nose of the Earth's bow shock. The data is obtained from the OMNI-Web interface[3] at NASA's Space Physics Data Facility (SPDF), Goddard Space Flight Center (GSFC). In this study the whole hourly data until 31 December 2016 is used, starting from 27 November 1963 (for the temperature from 26 July 1965). The data coverage of the different parameters is in the range 67–74 %, corresponding to a total duration of 36–40 years. We note that a test-comparison of hourly averaged data with higher-time-resolution data for the available shorter time span 1981–2016 did not show significant differences in our results. According to the

[3] http://omniweb.gsfc.nasa.gov/

OMNI data precision and maximal parameter ranges we specify bin sizes of 0.5 nT for the magnetic field strength, 10 km s^{-1} for the velocity, 1 cm^{-3} for the density and 10 000 K for the temperature. The frequency distributions of the solar-wind magnetic field strength, proton velocity, density and temperature are shown in Fig. 1. The solar-wind magnetic field strength is in the range 0.4–62 nT, the velocity in the range 156–1189 km s^{-1}, the density in the range 0–117 cm^{-3}, the temperature in the range 3450–6.63×10^6 K, and the mean data values are at 6.28 nT, 436 km s^{-1}, 6.8 cm^{-3} and 1.05×10^5 K. These ranges and mean values are as statistically expected from previous analyses of near 1 au solar-wind data (e.g., Table 3.3 in Bothmer & Daglis (2007, p. 39)). Much higher or lower peak values at 1 au have been observed in extraordinary events, such as the 23 July 2012 CME with a speed of over 2000 km s^{-1} and a peak field strength of about 100 nT that was observed by STEREO A (Russell et al. 2013), or the solar-wind disappearance event observed in May 1999 with density values even down to 0.2 cm^{-3} (Lazarus 2000).

The frequency distributions of the solar-wind parameters, magnetic field strength, proton density, and temperature, can be well approximated by lognormal distributions, whereas the proton velocity's frequency has a differing shape, as shown in Veselovsky et al. (2010). We investigate how well all four solar-wind parameters' frequency distributions can be represented by lognormal functions, which we use in the process of a least squares regression fitting. The lognormal function,

$$W(x) = \frac{1}{\sigma\sqrt{2\pi}x}\exp\left(-\frac{(\ln x-\mu)^2}{2\sigma^2}\right), \tag{1}$$

depends on the location μ and the shape parameter σ. Changes in μ affect both the horizontal and vertical scaling of the function whereas σ influences its shape. The distribution's median x_{med} and mean x_{avg} (average) positions are easily interpreted and are directly calculated from μ and σ:

$$x_{\mathrm{med}} = \exp(\mu) \qquad \Longleftrightarrow \qquad \mu = \ln(x_{\mathrm{med}})\,, \tag{2}$$

$$x_{\mathrm{avg}} = \exp\left(\mu+\frac{\sigma^2}{2}\right) \qquad \Longleftrightarrow \qquad \sigma = \sqrt{2\ln\left(\frac{x_{\mathrm{avg}}}{x_{\mathrm{med}}}\right)}. \tag{3}$$

It is apparent that the mean is always larger than the median. Replacing the variables μ and σ with these relations, the lognormal function (1) becomes

$$W(x) = \frac{1}{2\sqrt{\pi\ln\left(\frac{x_{\mathrm{avg}}}{x_{\mathrm{med}}}\right)}\,x}\exp\left(-\frac{\ln^2\left(\frac{x}{x_{\mathrm{med}}}\right)}{4\ln\left(\frac{x_{\mathrm{avg}}}{x_{\mathrm{med}}}\right)}\right). \tag{4}$$

The values of x_{med} and x_{avg} obtained from fitting the individual solar-wind frequency distributions are listed in Table 1.

From visual inspection, the resulting fit curves describe the shape of the magnetic field strength, the density and the temperature distributions well, as can be seen in Fig. 1. However, for the velocity, the fit function appears not to be as good in describing the measured distribution's more complex shape around its peak and in the higher velocity range. This also can be inferred from the sum of absolute residuals (SAR) between data and fit, listed in Table 1 as a percentage of the distribution area, being almost three times larger than those from the other parameters. In order to find a better fit result for the velocity distribution, we assume that the velocity distribution can be made up of at least two overlapping branches (McGregor et al. 2011a). Therefore a compositional approach is chosen by combining two lognormal functions (4), involving more fit variables:

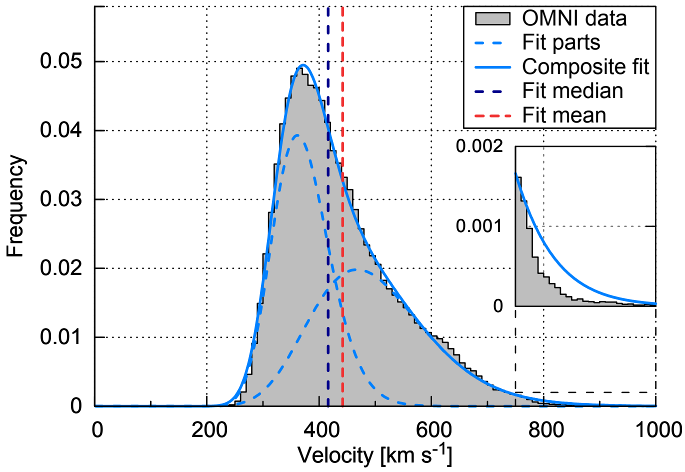

Fig. 2. Velocity frequency distribution (same as in Fig. 1) and its compositional lognormal fit. The fit's median and mean values and its two fit parts are indicated as well. The inset is a zoomed-in view of the high value tail of the distribution.

$$W_{\mathrm{II}}(x) = c \cdot W_1(x) + (1-c)\cdot W_2(x)\,. \tag{5}$$

The balancing parameter c ensures that the resulting function remains normalized as it represents a probability distribution. The fitting of $W_{\mathrm{II}}(x)$ to the velocity's frequency distribution yields the values of the now five fit parameters (c, $x_{\mathrm{med},1}$, $x_{\mathrm{avg},1}$, $x_{\mathrm{med},2}$ and $x_{\mathrm{avg},2}$) as listed in Table 1 together with the median and mean values of the composed distribution, which can be derived by solving

$$\int W_{\mathrm{II}}(x)\,\mathrm{d}x = 0 \qquad \text{and} \qquad \int x\,W_{\mathrm{II}}(x)\,\mathrm{d}x = 0\,. \tag{6}$$

This more complex fit function is more accurate in describing the velocity's frequency distribution as shown in Fig. 2. Thus in the following Sections we keep the double lognormal ansatz for all velocity frequency fits.

For the bulk of the solar wind these static lognormal functions describe the parameters' distributions well. The abnormally high parameter values in the distribution functions can be attributed to shock/CME events in agreement with the results of the OMNI solar-wind investigations by Richardson & Cane (2012). The simple lognormal fit functions underestimate the frequencies in their high-value tails, except for the temperature's tail which is overestimated, as seen in the insets of Fig. 1. This appears to be because CMEs do not come with abnormally high temperatures, but rather with temperatures lower than those of the average solar wind (Forsyth et al. 2006). The velocity's compositional lognormal fit only slightly overestimates its tail as seen in the inset of Fig. 2. The slow and fast part contribute almost equally ($c \approx 0.5$) to the long-term velocity distribution function.

3. Solar activity dependence of the solar-wind frequency distributions

In the next step we investigate how the long-term solar-wind distribution functions presented in the previous section depend on general solar activity. Therefore we examine their correlation with the SSN, being a commonly used long-term solar activity

Table 1. Resulting fit coefficients from the fitting of the lognormal function (4) to the shape of the solar-wind parameters' frequency distributions from near 1 au OMNI hourly data. For the velocity, the fit parameters of the double lognormal function (5) are also listed, as well as the median and mean values of the resulting velocity fit. The numbers in parentheses are the errors on the corresponding last digits of the quoted value. They are calculated from the estimated standard deviations of the fit parameters. For each parameter, the sum of absolute residuals between data and fit (in percentage of the distribution area) is also listed.

Parameter		Median x_{med}	Mean x_{avg}	Balance c	SAR [%]
Magnetic field [nT]		5.661(16)	6.164(18)	–	6.83
Velocity [10^2 km s^{-1}]		4.085(19)	4.183(20)	–	18.69
Density [cm^{-3}]		5.276(24)	6.484(34)	–	6.48
Temperature [10^4 K]		7.470(17)	11.301(32)	–	5.78
Velocity [10^2 km s^{-1}]	W_1	4.89(14)	5.00(14)	0.504(62)	–
	W_2	3.68(20)	3.72(20)		–
	W_{II}	4.16(14)[a]	4.42(14)[a]	–	4.20

Notes. [(a)] Error estimates derived from the individual fit part errors.

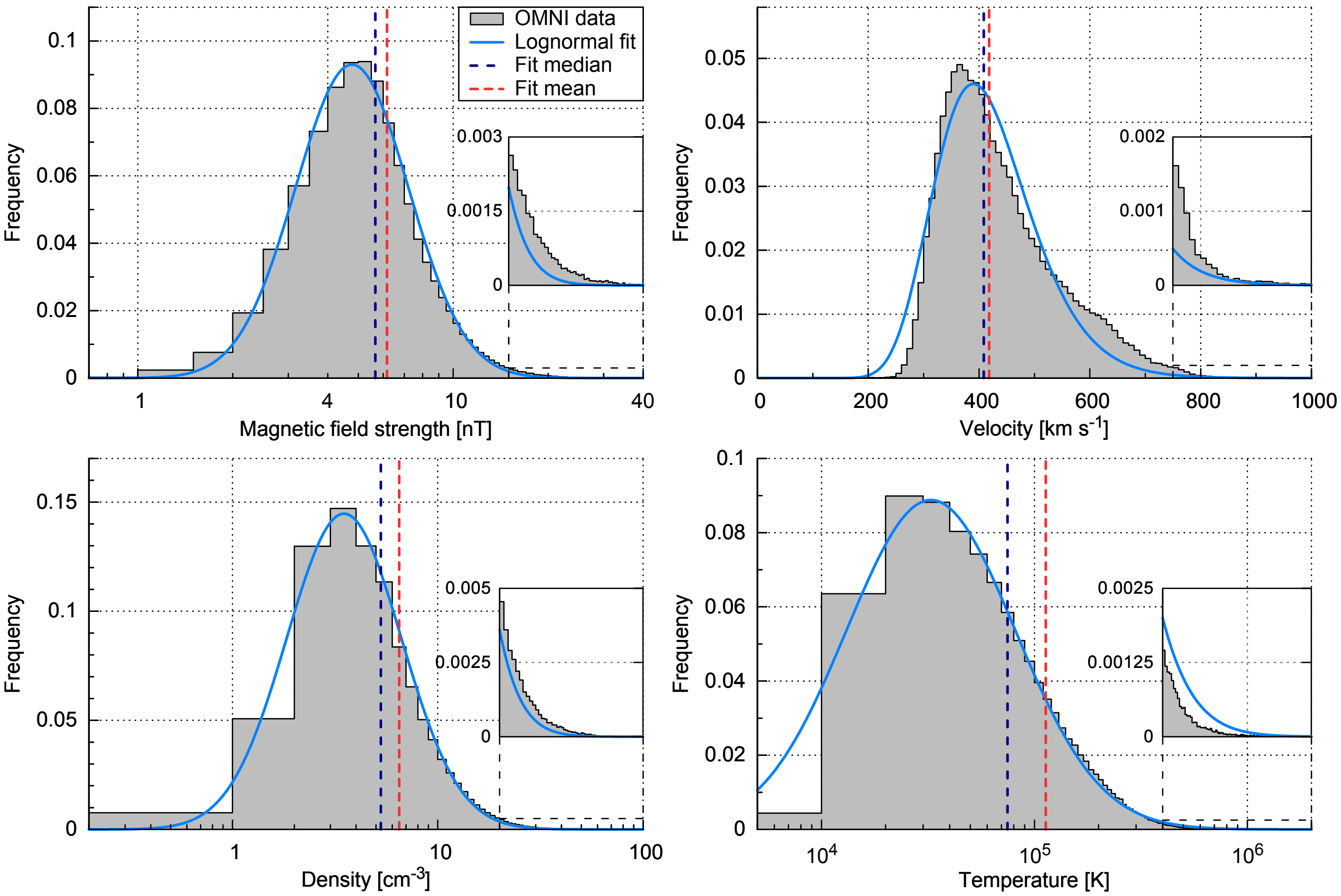

Fig. 1. Frequency distributions of the four solar-wind parameters and their lognormal fits derived from the hourly OMNI data set. The histograms have bins of 0.5 nT, 10 km s^{-1}, 1 cm^{-3} and 10 000 K. The fits' median and mean values are indicated as well. The insets show zoomed-in views of the high-value tails of the distributions.

index, and determine the time lags with the highest correlation coefficients.

For the correlations we fit lognormal functions to the frequency distributions as in Sect. 2, but implement linear relations to the yearly SSN, allowing shifting of the distribution functions with SSN. For the velocity the approach is different insofar as its two components are kept fixed and instead their balance is modified with the changing SSN. Thus we obtain solar-activity-dependent models for the frequency distributions of all four solar-wind parameters.

The international sunspot number (1963–2016) is provided by the online catalog[4] at the World Data Center – Sunspot Index and Long-term Solar Observations (WDC-SILSO), Solar Influences Data Analysis Center (SIDC), Royal Observatory of Belgium (ROB).

Yearly medians of the solar-wind parameters and the yearly SSN together with the solar cycle number are shown in the upper part of Fig. 3. The reason for correlating the SSN to the

[4] `http://www.sidc.be/silso/`

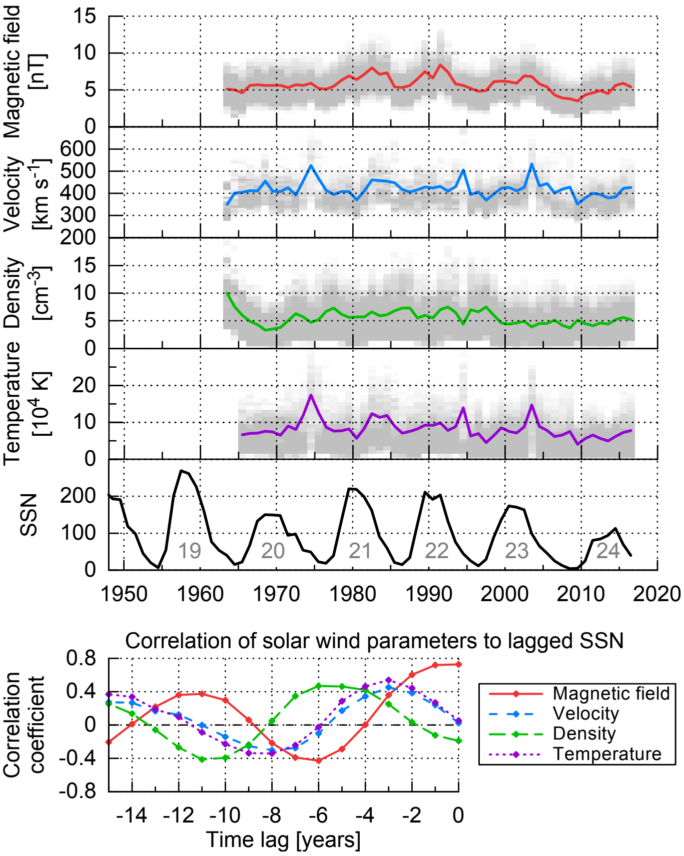

Fig. 3. Solar-wind parameter yearly frequencies (gray shading) with yearly medians (lines) derived from OMNI data and the yearly SSN from the SILSO World Data Center (1963–2016) with solar cycle number (top). Their correlation coefficients with the yearly SSN are calculated for time lags back to -15 years (bottom).

solar-wind median values is because the position of a lognormal function is defined by its median. The data are averaged to yearly values to avoid seasonal effects during the Earth's orbit around the Sun caused by its variations in solar latitude and distance. The solar-wind velocity, density, and temperature depend on the state of the solar cycle (Schwenn 1983). For instance the fast solar wind occurs at times when polar coronal holes extend to lower latitudes, a typical feature of the declining phase of the solar cycle as pointed out by Bothmer & Daglis (2007, p. 75, Fig. 3.52). Therefore the solar-wind velocity, density, and temperature maxima exhibit time lags relative to the SSN maxima.

The correlation coefficients of the solar wind parameters with the yearly SSN shown in the bottom part of Fig. 3 are calculated for time lags back to −15 years to cover a time span longer than a solar cycle. As expected, the amplitudes of the variations in the correlations of all parameters decline with increasing time lag and show a period of about 11 years. The highest correlation coefficient of 0.728 to the SSN is found for the magnetic field strength; it has no time lag. This finding is anticipated because the SSN is found to be directly proportional to the evolution of the photospheric magnetic flux (Smith & Balogh 2003). Velocity and temperature show time lags of 3 years with peak correlation coefficients of 0.453 and 0.540. The density with a correlation coefficient of 0.468 has a time lag of 6 years, which is in agreement with the density anticorrelation to the SSN reported by Bougeret et al. (1984).

Next we create solar-activity-dependent analytical representations of the solar wind frequency distributions. This is achieved

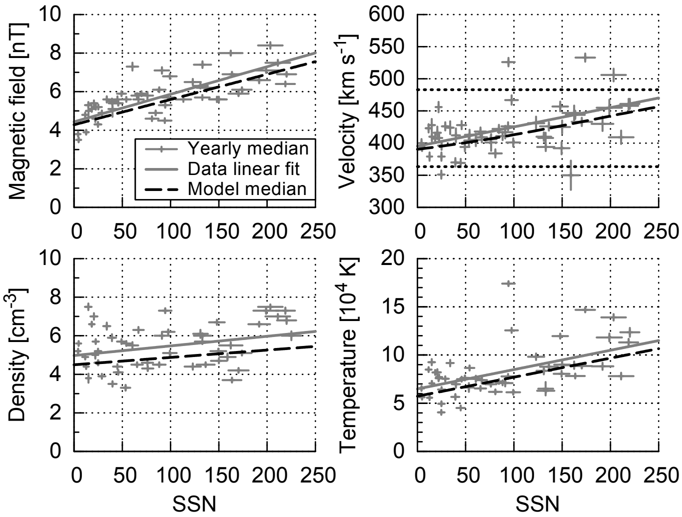

Fig. 5. Solar-wind parameter medians with respect to the lagged SSN. The yearly data medians (+) with their weighted linear fit (solid lines) are obtained from OMNI data. The error bars denote the SSN standard deviation and the relative weight from the yearly data coverage. The SSN-dependent median (dashed lines) is derived from the lognormal model fit. For the velocity the median is derived from the SSN-weighting (9) of the slow and fast model parts (dotted lines), whose magnitudes are SSN independent.

by shifting the median positions of the lognormal distributions as a linear function of the SSN. To enable these shifts, we add a linear SSN dependency to the median,

$$x_{\mathrm{med}}(ssn) = a_{\mathrm{med}} \cdot ssn + b_{\mathrm{med}}\,, \tag{7}$$

using a factor to the SSN a_{med} with a baseline b_{med}. We relate the mean with a scaling factor to the median to transfer its SSN dependency:

$$x_{\mathrm{avg}}(ssn) = \left(1 + a_{\mathrm{avg}}\right) \cdot x_{\mathrm{med}}(ssn)\,. \tag{8}$$

These relations, substituted into the lognormal function (4), lead to a new SSN-dependent function $W'(x, ssn)$. This function is then fitted to the yearly data, using the yearly SSN as input parameter. The SSN is offset with the individual time lags determined before for each parameter, to benefit from the higher correlation. The values of the three resulting fit coefficients ($a_{\mathrm{med}}, b_{\mathrm{med}}$ and a_{avg}) are presented in Table 2.

Naturally, the fit models match with the general data trends, as can be seen from Fig. 4, though single year variations are not replicated by the model (e.g., the high velocity and temperature values in 1974, 1994, and 2003). The comparison of this model with the yearly data median values with respect to the lagged SSN shows that the medians obtained from the modeling have a similar slope, as shown in Fig. 5.

Again, the solar-wind velocity needs a special treatment because of the application of the double lognormal distribution (5). Since it is well known that slow and fast solar-wind stream occurrence rates follow the solar cycle, we keep the two velocity components' positions SSN-independent ($x_{\mathrm{med}} = b_{\mathrm{med}}$) and vary instead their balance with the SSN:

$$c(ssn) = c_a \cdot ssn + c_b\,. \tag{9}$$

The fit result (see Table 2) yields a model in which three years after solar cycle minimum (SSN of zero) the contribution of slow

Table 2. Resulting fit coefficients from the OMNI data, based on the linear SSN dependencies (7) and (8). For the velocity the fit parameters from the double lognormal fit (5) and their balancing function (9) are given. The numbers in parentheses are the errors on the corresponding last digits of the quoted value. They are calculated from the estimated standard deviations of the fit parameters. The listed SSN time lags are used for the fits.

Parameter		Median		Mean	Balance		SSN lag
		SSN factor a_{med}	Baseline b_{med}	Scaling factor a_{avg}	SSN factor c_a	Baseline c_b	[years]
Magnetic field [nT]		$1.309(19) \times 10^{-2}$	4.285(17)	$8.786(78) \times 10^{-2}$	–	–	0
Density [cm^{-3}]		$3.81(25) \times 10^{-3}$	4.495(26)	$3.050(27) \times 10^{-1}$	–	–	6
Temperature [10^4 K]		$1.974(26) \times 10^{-2}$	5.729(19)	$6.541(28) \times 10^{-1}$	–	–	3
Velocity	W_1'	–	3.633(12)	$1.008(37) \times 10^{-2}$	$-1.799(95) \times 10^{-3}$	0.638(32)	3
[$10^2\,\mathrm{km\,s^{-1}}$]	W_2'	–	4.831(81)	$2.31(20) \times 10^{-2}$			

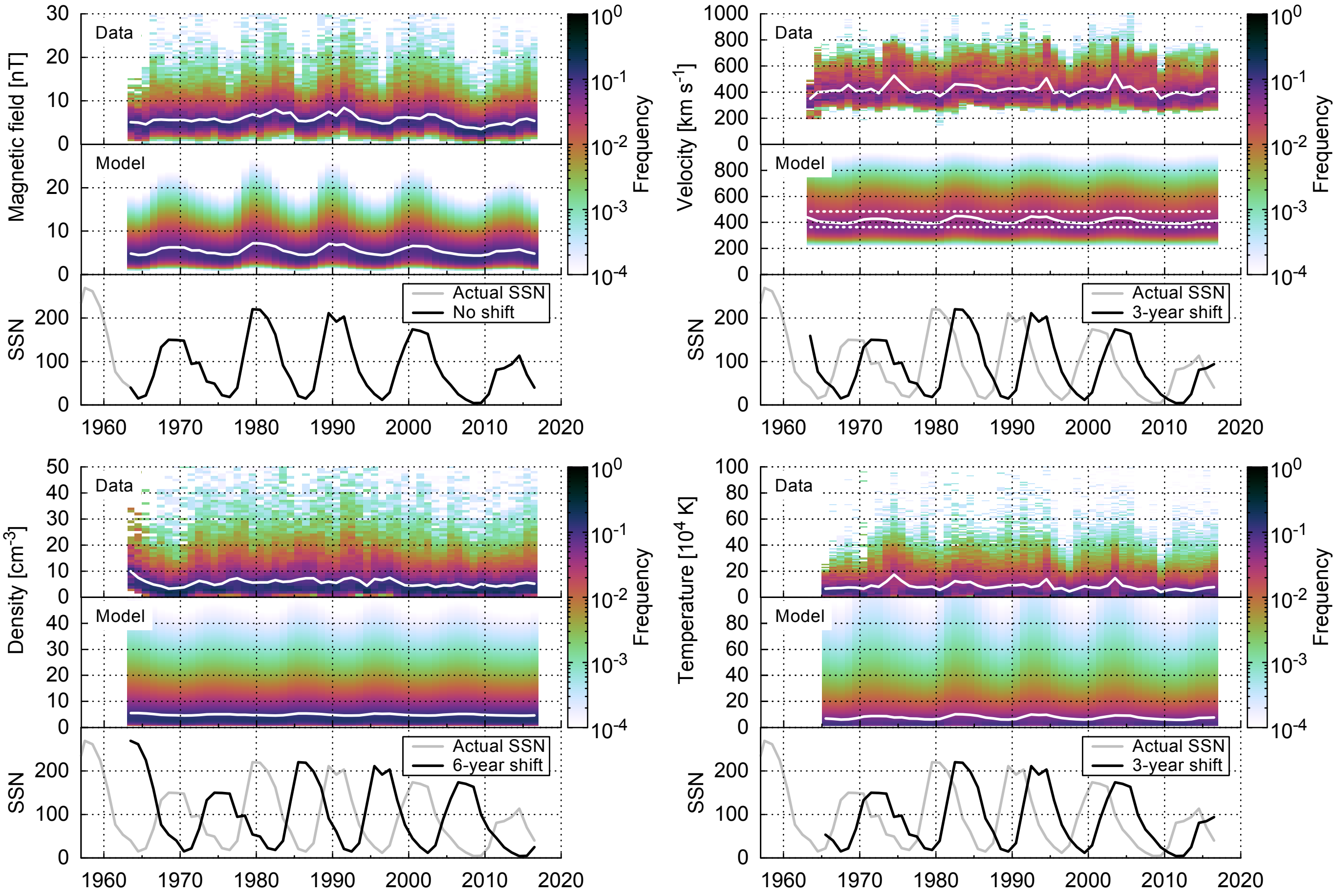

Fig. 4. Solar wind parameter yearly data frequencies and lognormal fit models, both with their median values (white lines) over the OMNI time period 1963–2016. The corresponding yearly SSN and the shifted SSN for the models are indicated by gray and black lines. The velocity median is derived from the SSN-weighted constant lognormal parts (dotted lines).

solar wind to the overall solar wind distribution reaches a maximum value (about 64 %) and decreases with increasing SSN as shown in Fig. 6.

To investigate the amount of slow and fast wind contributions depending on solar activity, we apply the commonly used constant velocity threshold of $v_{\mathrm{th}} = 400\,\mathrm{km\,s^{-1}}$ (Schwenn 1990, p. 144). The linear fit to the yearly data ratio and the derived model ratio show a good agreement (see Fig. 6). The to-some-degree steeper balance parameter of the double fit function used in this model cannot be compared directly with specific velocity thresholds between slow and fast solar wind. However, it appears to be a more realistic approach than just taking a specific velocity threshold for the slow and fast wind, in agreement with the overlapping nature of the velocity flows reported by McGregor et al. (2011a).

4. Solar distance dependency

In order to derive heliocentric distance relationships of the bulk solar wind distribution functions, we apply and fit power law dependencies to the Helios data. We then examine how the fits may be extrapolated towards the Sun and in particular in to the PSP orbit. We use the fitting methods of Sect. 2 for the distance-binned combined data from both Helios probes. Helios' highly elliptical orbits in the ecliptic covered a solar distance range of 0.31–0.98 au in case of Helios 1 and 0.29–0.98 au in case of Helios 2. Launched during solar cycle minimum, the data of both probes cover the rise to the maximum of cycle 21, covering ~6.5 years at varying distances to the Sun.

We investigate hourly averages of the Helios data in the same way as with the OMNI data. The Helios 1 merged hourly data from the magnetometer and plasma instruments (Rosenbauer

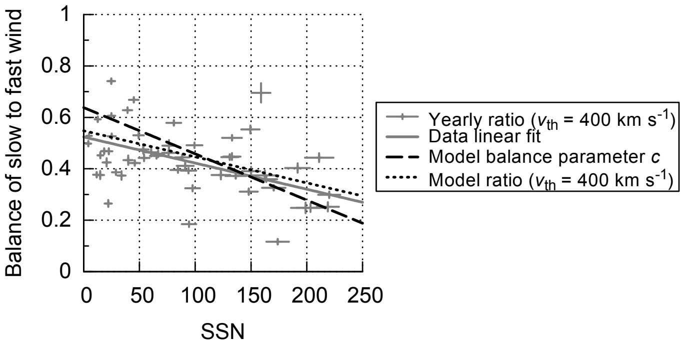

Fig. 6. Ratio of slow to fast solar wind for a SSN lagged by 3 years. The yearly ratios (+) and their weighted linear fit (solid line) are obtained from OMNI data with a threshold velocity of $v_{th} = 400\,\mathrm{km\,s^{-1}}$. The error bars denote the SSN standard deviation and the relative weight from the yearly data coverage. The model's balance parameter (9) and derived ratio (same threshold) are plotted as dashed and dotted lines.

et al. 1977) include ~12.5 orbits for the time range 10 December 1974 to 14 June 1981, and those for Helios 2 include ~8 orbits for the time span 1 January 1976 to 4 March 1980. The data are retrieved from the Coordinated Data Analysis Web (CDAWeb) interface at NASA's GSFC/SPDF[5].

The Helios 1 magnetometer data coverage for this data set is about 43 % (i.e., 2.8 years), and that of Helios 2 amounts to 54 % (i.e., 2.3 years). The plasma data coverage is 76 % (i.e., 5.0 years) in case of Helios 1 and 92 % (i.e., 3.9 years) in case of Helios 2. Thus, using this data, we point out that its time coverage is unequally distributed over the solar cycle. Considering the data gap distributions, the amount of data during solar cycle minimum up to mid 1977, that is, the transition from minimum to maximum, covers about 68 % of this period whereas during maximum of cycle 21 data are available only 38 % of the time. This Helios data bias towards solar minimum is one reason why in this study the Helios solar wind data are not used to derive long-term frequency distributions and solar-cycle dependencies for the key solar wind parameters.

The radial dependencies of the key solar-wind parameters over the distance range 0.29–0.98 au measured by both Helios probes are plotted in Fig. 7, together with their median and mean values for different solar distances, calculated for the minimal distance resolution 0.01 au of the data set. Assuming a radial solar-wind outflow, it is expected that the distance dependence of the solar-wind parameters over the Helios data range 0.29–0.98 au can be described through power law scaling. Therefore we use the power law function,

$$x(r) = d \cdot r^{e}, \qquad (10)$$

for the regression fit of the median and mean, with r being the solar distance in astronomical units, d the magnitude at 1 au and e the exponent. The fits are weighted through the different data counts per bin. The obtained coefficients for the median and mean power law fits (d_{med}, e_{med}, d_{avg} and e_{avg}) are listed in Table 3 and their corresponding curves are shown in Fig. 7.

Our derived exponents agree with those found in existing studies from the Helios observations: Mariani et al. (1978) derived the exponents for the magnetic field strength separately for the fast and slow solar wind as $B_{\mathrm{fast}} \propto r^{-1.54}$ and $B_{\mathrm{slow}} \propto r^{-1.61}$, ours is $B_{\mathrm{avg}} \propto r^{-1.55}$. The velocity exponent $v_{\mathrm{avg}} \propto r^{0.049}$ matches with the values found by Schwenn (1983, 1990), who derived the distance dependencies for both Helios spacecraft separately as $v_{\mathrm{H1}} \propto r^{0.083}$ and $v_{\mathrm{H2}} \propto r^{0.036}$. The calculated density exponent $n_{\mathrm{avg}} \propto r^{-2.01}$ agrees well with the Helios plasma density model derived by Bougeret et al. (1984) yielding $n \propto r^{-2.10}$. The temperature exponent $T_{\mathrm{avg}} \propto r^{-0.79}$ is similar to those in the studies by Hellinger et al. (2011, 2013), who also derived the exponents separately for the fast and the slow solar wind: $T_{\mathrm{fast}} \propto r^{-0.74}$ and $T_{\mathrm{slow}} \propto r^{-0.58}$.

The mean and median velocity fit exponents acquired from the Helios data are very similar, which indicates that they can be kept identical so that the basic shape of the frequency distribution does not change with distance. Conversely, the mean and median fits for the magnetic field strength cross each other at 0.339 au (see Table 3) and the mean becomes slightly lower than the median at smaller distances. Thus, below that distance the frequency distribution can no longer be well described by a lognormal function, because the mean of a lognormal function has to be larger than its median (as pointed out in Sect. 2), that is, the location of the crossing indicates that the parameter's distribution is no longer of a lognormal shape thereafter. The fits for the proton temperature show a similar behavior, having an extrapolated intersection at 0.082 au. Therefore the extrapolation of the magnetic field and temperature distribution frequencies to the PSP orbit by applying lognormal functions is limited. The crossing points limit the regions where the distribution's shapes can still be considered lognormal.

In order to still fit and extrapolate lognormal functions with the data, we assume that the shapes can be considered lognormal at all distances. For the frequency distribution fit function to be discussed in the following paragraph, we reduce the fit exponents e_{med} and e_{avg} to only one. We note that this simplification leads to slightly larger modeling errors, especially in case of the magnetic field strength.

Next we retrieve the frequency distributions of the four solar wind parameters in solar distance bins of 0.01 au, choosing the same resolution as for the OMNI data analyzed in Sect. 2 – the distributions and their median values are plotted in Fig. 8. For simplification, as mentioned before, we treat the exponents of the median and mean fit functions as being identical, using one fit parameter for both. Implementing the power law distance dependency (10) into the lognormal function (4), we get the fit parameters d'_{med}, d'_{avg} and the common exponent e'. Again, we use the double lognormal function (5) for the velocity distribution fit – resulting in $W''_{\mathrm{II}}(x, r)$. The additional fit parameters are the balancing parameter c' and for the second lognormal part $d'_{\mathrm{med},2}$ and $d'_{\mathrm{avg},2}$. The resulting fit coefficients for the four solar wind parameters are presented in Table 4.

The velocity balancing parameter $c' = 0.557$ is in good agreement with the results for the SSN dependency (9), because with a mean SSN of 59 during the Helios time period, $c(59) = 0.53$, as can be seen from Fig. 6.

The power law lognormal models and the power law double lognormal model for the velocity, which result from the fitting, are plotted in Fig. 8 together with their median values. The model's magnetic field strength is broader around values of 40 nT at the lower distance boundary than the data's frequency distribution implies. This behavior is expected because of the applied distance-independent shape approximation. The velocity and temperature models' upper values generally show a higher abundance than the actual data; see also zoom boxes in Figs. 1 and 2. The high-velocity tail that increases with distance arises from using the same exponent for both slow and fast components. This effect is not seen in the data; more specifically, not

[5] http://spdf.gsfc.nasa.gov/

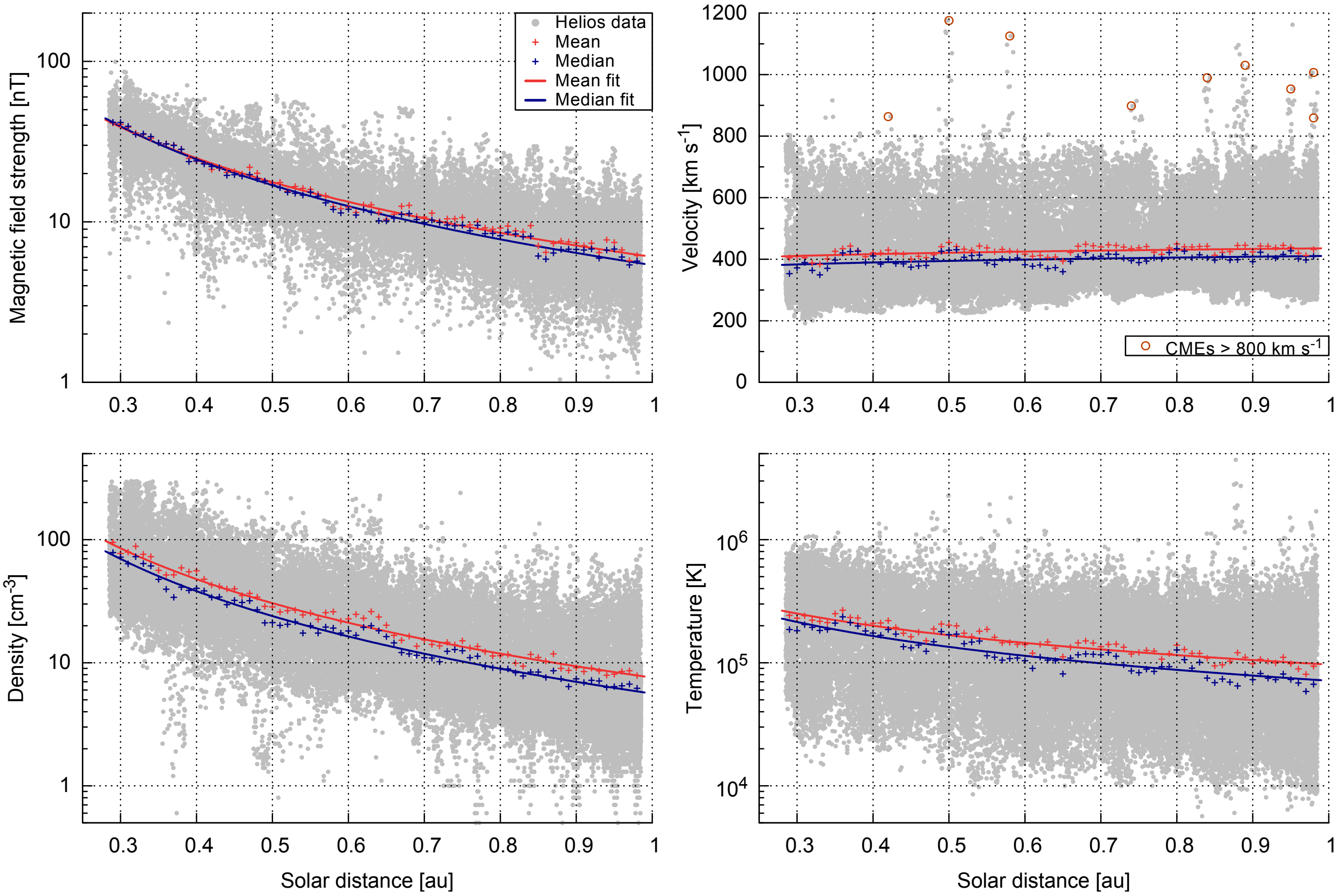

Fig. 7. Helios hourly data plots of the four solar wind parameters over solar distance. The mean and median per 0.01 au data bin and their fit curves are plotted as well. The Helios data has a native distance resolution of 0.01 au, thus, to make the distribution visible in these plots, we added a random distance value of up to ±0.005 au. The high velocity data points above 800 km s^{-1} (circled red) are identified as CME events (e.g., Sheeley et al. 1985; Bothmer & Schwenn 1996, 1998).

Table 3. Fit coefficients for the median and mean solar distance dependencies (10) of the four solar wind parameters derived from the combined Helios 1 and 2 data. The numbers in parentheses are the errors on the corresponding last digits of the quoted value. They are calculated from the estimated standard deviations of the fit parameters. The crossing distances indicate where the median and mean fits intersect each other. The yearly variation is the weighted standard deviation derived from the yearly fit exponents seen in Fig. 9.

Parameter	Median		Mean		Crossing distance	Yearly variation
	d_{med}	e_{med}	d_{avg}	e_{avg}	[au]	Δe
Magnetic field [nT]	5.377(92)	−1.655(17)	6.05(10)	−1.546(18)	0.339(11)	0.11
Velocity [10^2 km s^{-1}]	4.107(28)	0.058(13)	4.356(24)	0.049(10)	$0.7(83) \times 10^3$	0.012
Density [cm^{-3}]	5.61(27)	−2.093(46)	7.57(30)	−2.010(38)	0.027(73)	0.072
Temperature [10^4 K]	7.14(23)	−0.913(39)	9.67(21)	−0.792(28)	0.082(85)	0.050

Table 4. Fit coefficients for the distance-dependent single lognormal function, based on Equation (4) combined with (10) from the combined Helios data. Regarding the velocity, the double lognormal function (5) is used instead. The numbers in parentheses are the errors on the corresponding last digits of the quoted value. They are calculated from the estimated standard deviations of the fit parameters. The seasonal variations are calculated from Earth's orbital solar distance variation and the derived exponents.

Parameter		Median d'_{med}	Mean d'_{avg}	Exponent e'	Balance c'	Seasonal variation Δd [%]
Magnetic field [nT]		5.358(25)	5.705(28)	−1.662(11)	–	2.8
Density [cm^{-3}]		5.424(33)	6.845(47)	−2.114(20)	–	3.6
Temperature [10^4 K]		6.357(64)	10.72(14)	−1.100(20)	–	1.9
Velocity [10^2 km s^{-1}]	W''_1	3.707(13)	3.748(16)	0.0990(51)	0.557(45)	0.17
	W''_2	5.26(13)	5.42(11)			
	W''_{II}	4.13(13)^a	4.47(11)^a	–	–	–

Notes. $^{(a)}$ Velocity median and mean 1 au values for the resulting function. Error estimates derived from the individual fit part errors.

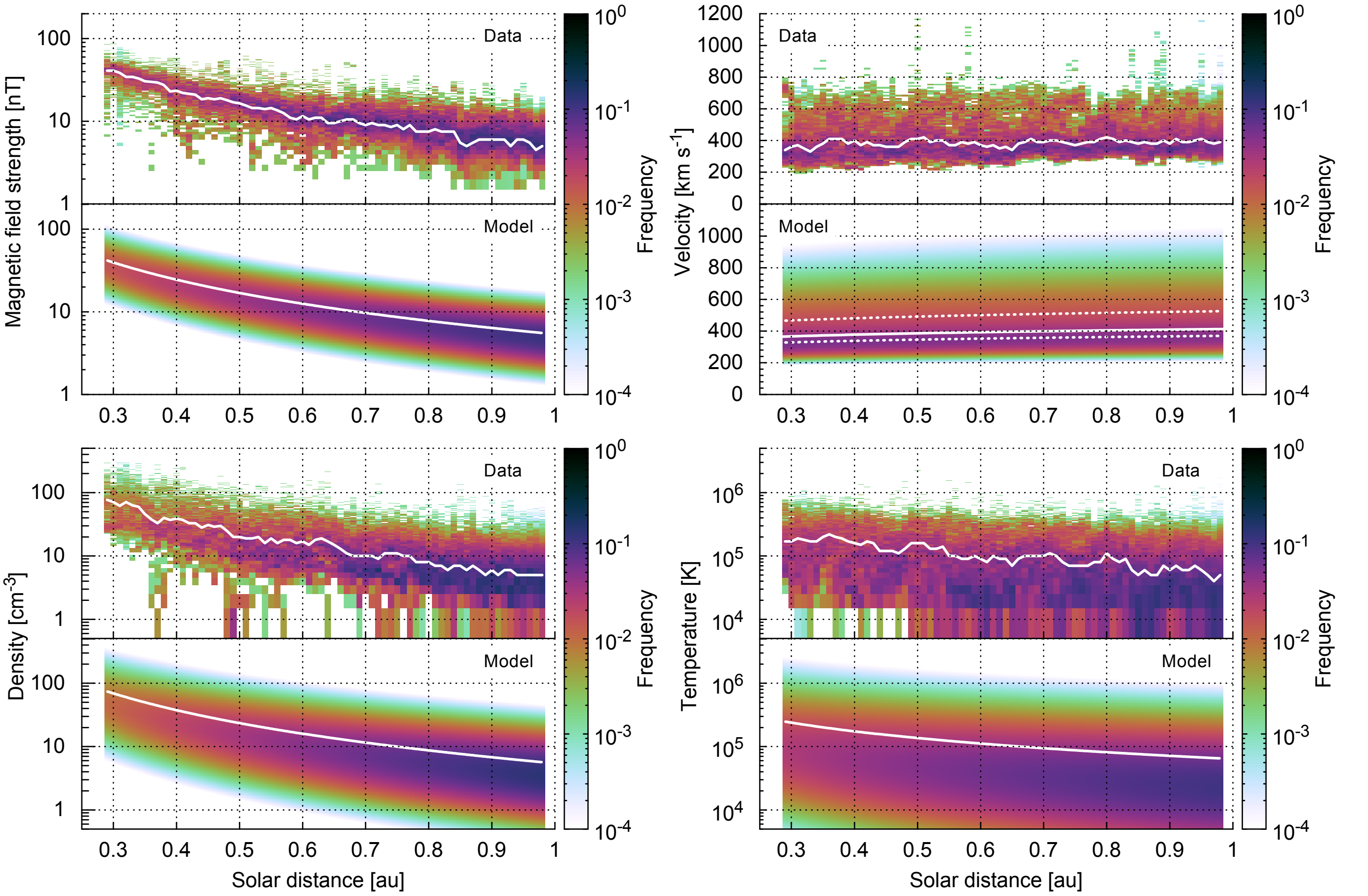

Fig. 8. Frequency distributions of the four solar wind parameters with respect to solar distance. Plotted are the binned Helios data and the power law lognormal fit models with their median values (white lines). The double lognormal model is used for the velocity, its slow and fast parts are indicated by dotted lines.

only the slowest wind but also the fastest wind is expected to converge to more average speeds (Sanchez-Diaz et al. 2016).

5. Empirical solar-wind model

In order to estimate the solar-wind environment for the PSP orbit, we combine the results from the solar-wind frequency distributions' solar-activity relationships and their distance dependencies derived from the OMNI and Helios data. The result is an empirical solar-wind model for the inner heliosphere which is then extrapolated to the PSP orbit in Sect. 6.

This solar-wind model for the radial distance dependence is representative for the time of the Helios observations around the rise of solar cycle 21. The variations of the yearly power law fit exponents from fitting the solar-distance dependency (10) are shown in Fig. 9 together with the yearly SSN for the time period 1974–1982. It can be seen that during the Helios time period there might be some systematic variation of the exponents with solar activity – at least for the velocity and temperature exponents. However, for simplicity we assume that the distance scaling laws can be treated as time independent and include the calculated exponents' yearly variations Δe, summarized in Table 3, as relative uncertainties.

Since we neglect possible variations of the distance scaling laws, we combine the frequency distribution's median solar activity dependency (7) derived for 1 au from the OMNI data with

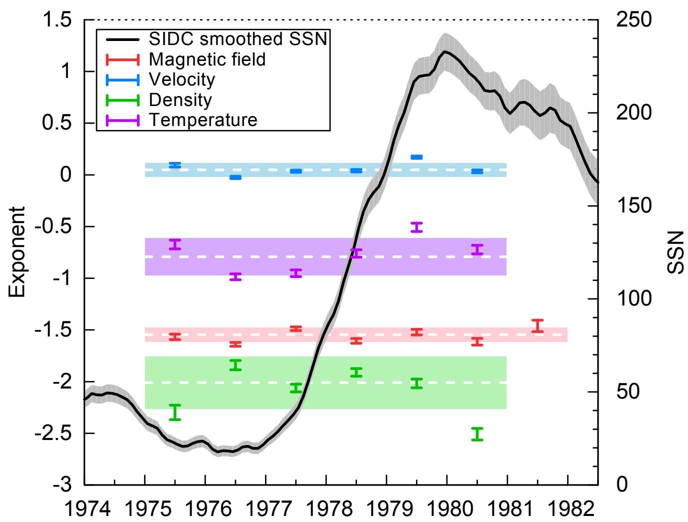

Fig. 9. Helios yearly variation of the solar wind parameter power exponents for the dependence on radial distance together with the SIDC 13-month smoothed monthly SSN. The weighted standard deviations and average values for all years are indicated by the shaded areas. In this plot, the 21 days since Helios launch in the year 1974 are omitted because a distance range of merely 0.95–0.98 au was covered that year.

the power law exponents (10) derived from the Helios data:

$$x_{\mathrm{med}}(ssn, r) = (a_{\mathrm{med}} \cdot ssn + b_{\mathrm{med}}) \cdot r^{e'} . \quad (11)$$

Thus, implementing the median and mean relations into the log-normal function (4), we obtain the combined model function $W'''(x, ssn, r)$ and for the velocity $W_{\mathrm{II}}'''(x, ssn, r)$ with the double lognormal function (5). The corresponding median and mean relations for each solar-wind parameter, based on the values resulting from our analyses, are listed below. Their numerical values are the fit parameters from Table 2 and the exponents from Table 4.

– The magnetic field strength relations, depending on solar activity and solar distance, are:

$$B_{\mathrm{med}}(ssn, r) = (0.0131\,\mathrm{nT} \cdot ssn + 4.29\,\mathrm{nT}) \cdot r^{-1.66}\,, \tag{12}$$

$$B_{\mathrm{avg}}(ssn, r) = 1.0879 \cdot B_{\mathrm{med}}(ssn, r)\,. \tag{13}$$

– The proton velocity relations for the slow and fast components, depending on solar distance, are:

$$v_{\mathrm{med}}^{\mathrm{slow}}(r) = 363\,\mathrm{km\,s^{-1}} \cdot r^{0.099}\,, \qquad v_{\mathrm{med}}^{\mathrm{fast}}(r) = 483\,\mathrm{km\,s^{-1}} \cdot r^{0.099}\,, \tag{14}$$

$$v_{\mathrm{avg}}^{\mathrm{slow}}(r) = 1.0101 \cdot v_{\mathrm{med}}^{\mathrm{slow}}(r)\,, \qquad v_{\mathrm{avg}}^{\mathrm{fast}}(r) = 1.023 \cdot v_{\mathrm{med}}^{\mathrm{fast}}(r)\,. \tag{15}$$

The share of both components balanced with solar activity is found to be:

$$c(ssn) = -0.00180 \cdot ssn + 0.64\,. \tag{16}$$

– The derived relations of the proton density are:

$$n_{\mathrm{med}}(ssn, r) = \left(0.0038\,\mathrm{cm^{-3}} \cdot ssn + 4.50\,\mathrm{cm^{-3}}\right) \cdot r^{-2.11}\,, \tag{17}$$

$$n_{\mathrm{avg}}(ssn, r) = 1.305 \cdot n_{\mathrm{med}}(ssn, r)\,. \tag{18}$$

– The derived proton temperature relations are:

$$T_{\mathrm{med}}(ssn, r) = (197\,\mathrm{K} \cdot ssn + 57\,300\,\mathrm{K}) \cdot r^{-1.10}\,, \tag{19}$$

$$T_{\mathrm{avg}}(ssn, r) = 1.654 \cdot T_{\mathrm{med}}(ssn, r)\,. \tag{20}$$

These relations average over seasonal variations because they are based on yearly data. The OMNI data are time-shifted to the nose of the Earth's bow shock; this leads to yearly solar distance variations of ±1.67 % as it orbits the Sun. The resulting maximal solar-wind parameter variation amplitudes over the year can thus be derived from the derived power law exponents. They are estimated to be smaller than 4 % as seen in Table 4. Bruno et al. (1986) and Balogh et al. (1999) have pointed out that the solar-wind parameters vary with latitudinal separation from the heliospheric current sheet. Its position in heliographic latitude is highly variable around the solar equator (Schwenn 1990) and, furthermore, the Earth's orbit varies over the course of the year by ±7.2° in latitude. Since this latitudinal separation is highly variable and requires significant effort to calculate for an extended time series, we have ignored this aspect in this analysis.

6. Model extrapolation to PSP orbit

To estimate PSP's solar-wind environment during its mission time for its orbital positions, predictions of the SSN during the mission are incorporated into the empirical solar-wind model, derived in the previous Sections, and extrapolations down to the PSP perihelion region are performed.

Parker Solar Probe is planned to launch in mid 2018. With its first Venus flyby it will swing into Venus' orbital plane, reaching a first perihelion with a distance of 0.16 au just 93 days after launch, in November 2018. Seven additional Venus flybys allow the perihelion distance to be reduced to a minimum of 9.86 $R_\odot$. This distance will be reached with the 22nd perihelion in December 2024 (Fox et al. 2015), as plotted in the top panel of Fig. 10.

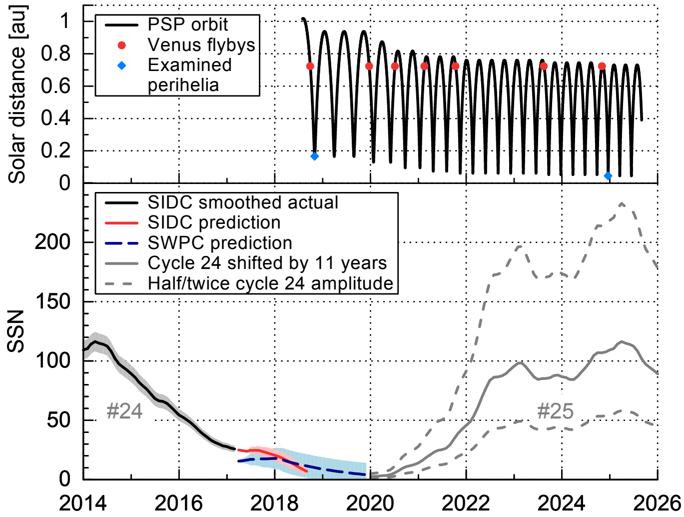

Fig. 10. PSP's solar distance during its mission time (top). Consecutive Venus flybys bring its perihelia nearer to the Sun. Actual and predicted SSN (bottom), that is, SIDC 13-month smoothed monthly actual SSN, SIDC Standard Curves Kalman filter prediction and SWPC prediction with their corresponding expected ranges (shaded areas). The SSN from previous cycle 24, shifted by 11 years, is plotted together with two alternative trends of half and twice its amplitude.

We extrapolate the derived empirical solar-wind models to PSP's orbital distance range and compare the results with those from the existing models shown in Fig. 11. The model and its extrapolation are visualized for the SSN range between solar minimum and maximum ($0 \leq ssn \leq 200$), indicated by the shaded regions in the Figure. The magnetic field strength is found to increase from median values of about 43 nT at 0.25 au to 715 nT at 0.046 au for a SSN of zero. Taking a SSN of 200 increases the values to 69 nT and 1152 nT. Our extrapolation results are slightly flatter than those derived from the analytical magnetic field model by Banaszkiewicz et al. (1998), who constructed an analytic dipole plus quadrupole plus current sheet (DQCS) model for solar minimum. We note that one cannot easily compare the absolute values of our study with the values obtained by Banaszkiewicz et al. (1998) because the DQCS model assumes solar wind originating from coronal holes at higher heliographic latitudes only, neglecting the slow solar-wind belt. We suggest that the difference in slope is due to the previously mentioned (Sect. 4) changing shape of the frequency distribution with heliocentric distance, which for smaller distances deviates more from the model's lognormal distribution. The average velocity is found to decrease from 340 km s^{-1} at 0.25 au to about 290 km s^{-1} at 0.046 au 3 years after a SSN of zero occurred, whereas using a SSN of 200 it decreases from 390 km s^{-1} to 330 km s^{-1}. Comparing the results with the measurements by Sheeley et al. (1997) and Wang et al. (2000) shows an overestimation in our extrapolated slow solar-wind velocity values for distances below approximately 20 $R_\odot$. They used LASCO coronagraph observations to track moving coronal features (blobs) in the distance range 2–30 $R_\odot$ to determine speed profiles and sources of the slow solar wind and they derived temperature and sonic point values for slow solar wind with the isothermal expansion model from Parker (1958). Therefore, it generally can be expected that

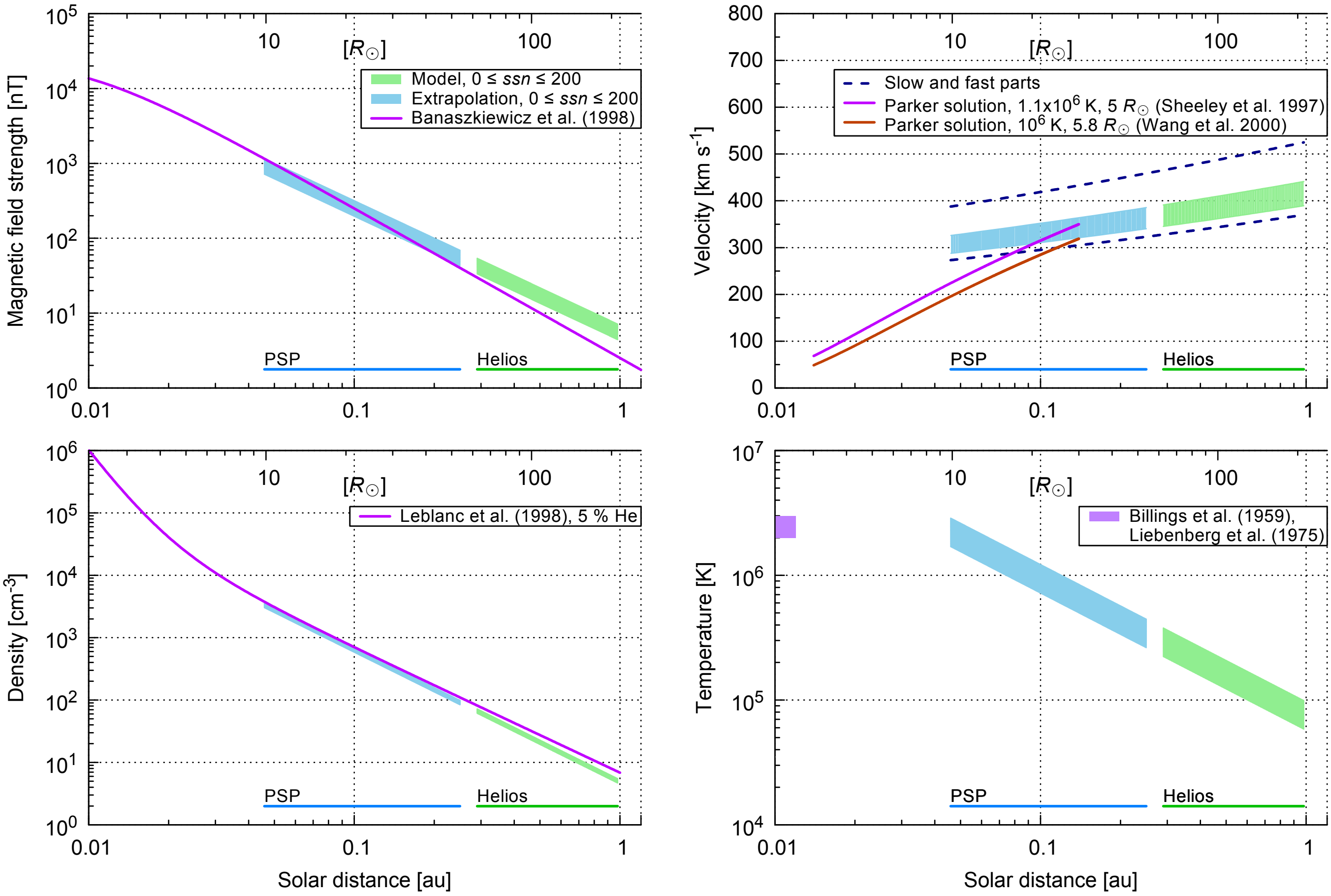

Fig. 11. Radial extrapolation of the solar-wind parameters to the PSP orbit region. The median values from the models, obtained from Helios and OMNI measurements, are extrapolated to the PSP region for SSN values between solar minimum and maximum, that is, $0 \leq ssn \leq 200$. The lower edges of the shaded areas correspond to solar minimum, the upper edges to solar maximum. Also plotted are the radial dependencies of the analytic DQCS magnetic field model for solar minimum from Banaszkiewicz et al. (1998), the slow wind velocity models from Sheeley et al. (1997) and Wang et al. (2000), the density model from Leblanc et al. (1998) and the range of temperature measurements from Billings (1959) and Liebenberg et al. (1975).

PSP will encounter a slower solar-wind environment close to the Sun than our model estimates. Thus PSP will measure solar-wind acceleration processes (McComas et al. 2008), maybe even still at 30 $R_\odot$ as the study by Sheeley et al. (1997) suggests. The proton density increases from about 84 cm^{-3} at 0.25 au to about 3018 cm^{-3} at 0.046 au 6 years after a SSN of zero occurred. Being almost independent of the SSN, the values for a SSN of 200 are only 17 % larger. The results are in good agreement with those of Leblanc et al. (1998), who derived an electron density model from type III radio burst observations. Their model shows that the density distance dependency scales with r^{-2} and steepens just below 10 $R_\odot$ with r^{-6}. We assumed a solar-wind helium abundance of 5 % to convert these electron densities to proton densities. The extrapolated proton temperature increases from about 260 000 K at 0.25 au to about 1 690 000 K at 0.046 au 3 years after a SSN of zero occurred and from 440 000 K to 2 860 000 K for a SSN of 200. Knowing that near-Sun coronal temperatures are in the range of 2–3 MK (Billings 1959; Liebenberg et al. 1975), the model overestimates the extrapolated temperatures at the PSP perihelion distance.

Aside from the solar distance, the derived solar-wind parameter models depend on the SSN. Short-term predictions of the SSN can be used for the solar-wind predictions of PSP's early perihelia and also for refining the solar-wind predictions during PSP's mission. Several sources are available for SSN short-term predictions. The SIDC provides 12-month SSN forecasts[6] obtained from different methods (e.g., Kalman filter Standard Curve method). The SSN prediction of NOAA's Space Weather Prediction Center (SWPC) for the time period until the end of 2019 follows a consensus of the Solar Cycle 24 Prediction Panel[7]. The SSN for PSP's first perihelion will be small – certainly below 20 – whereas the SSN during the closest perihelia, which will commence at the end of 2024 at the likely maximum phase of cycle 25, cannot be predicted at this time. However, Hathaway & Upton (2016) found indications that the next solar cycle will be similar in size to the current cycle 24. Therefore we simply assume a pattern similar to the last cycle for the prediction of the next solar cycle and thus shift the last cycle by 11 years. Additionally, we consider as possible alternatives SSN patterns of half and twice its amplitude as shown in the bottom panel of Fig. 10.

Implementing the SSN predictions for the PSP mission time and the orbital trajectory data, we can infer which solar-wind parameter magnitudes can be expected. Figures 12 and 13 show the median values (7) of the considered different solar-wind parameters for 12-day periods, comprising the first perihelion in

[6] http://sidc.be/silso/forecasts
[7] http://www.swpc.noaa.gov/products/solar-cycle-progression

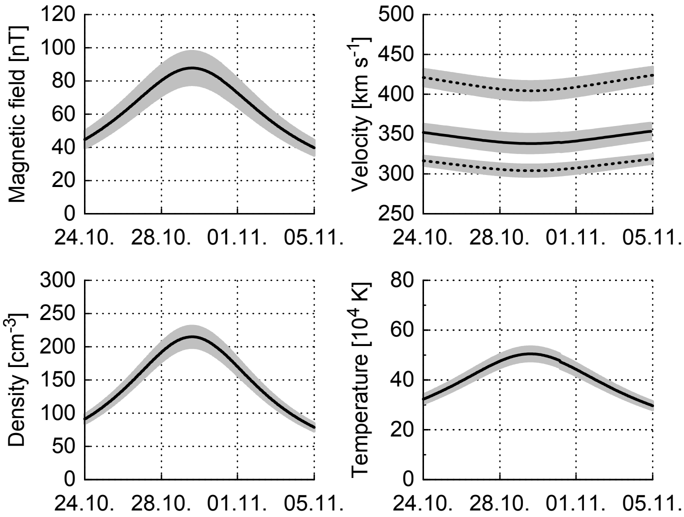

Fig. 12. Estimated solar-wind parameter medians (black lines) and their error bands (gray) during 12 days in 2018 with PSP's first perihelion at about 0.16 au. For the velocity the combined median is calculated and also the SSN-independent slow and fast parts are plotted (dotted lines).

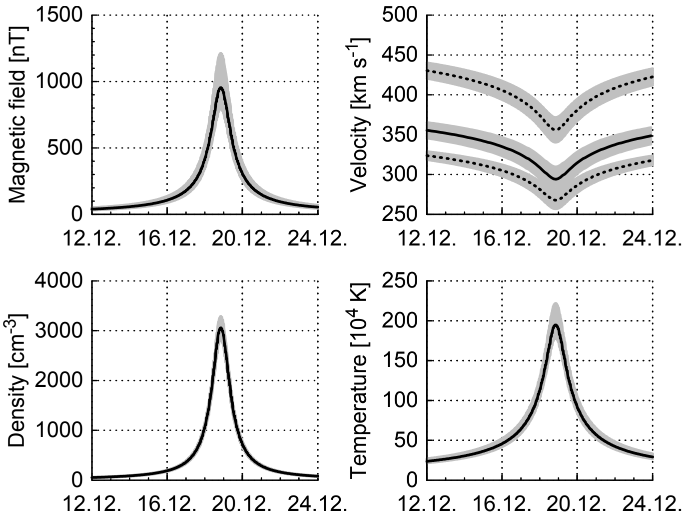

Fig. 13. Estimated solar-wind parameter medians (black lines) and their error bands (gray) during 12 days in 2024 with PSP's 22nd (the first closest) perihelion at 0.0459 au. For the velocity the combined median is calculated and also the SSN-independent slow and fast parts are plotted (dotted lines).

Novemver 2018 and the first closest perihelion in December 2024. In the beginning of the mission median values of about 87 nT, 340 km s^{-1}, 214 cm^{-3} and 503 000 K are estimated to be measured at 0.16 au, increasing to about 943 nT, 290 km s^{-1}, 2951 cm^{-3} and 1 930 000 K during the first closest approach at 0.046 au. Monthly SSNs – shifted by the time lags specific to the solar-wind parameters – are used in the calculation of the solar-wind predictions. These SSNs are either actual smoothed values from the SIDC with their reported standard deviations, short-term predictions from the SWPC with their expected ranges, or actual smoothed values from the SIDC shifted by 11 years with half/twice their values as uncertainties. The error bands given in both Figures, calculated from error propagation, include these SSN ranges and the derived fit parameter errors.

Finally the estimated solar-wind environment can be derived from the function $W'''(x, ssn, r)$. The estimated frequency distributions of the four solar-wind parameters at PSP's 1st and 22nd

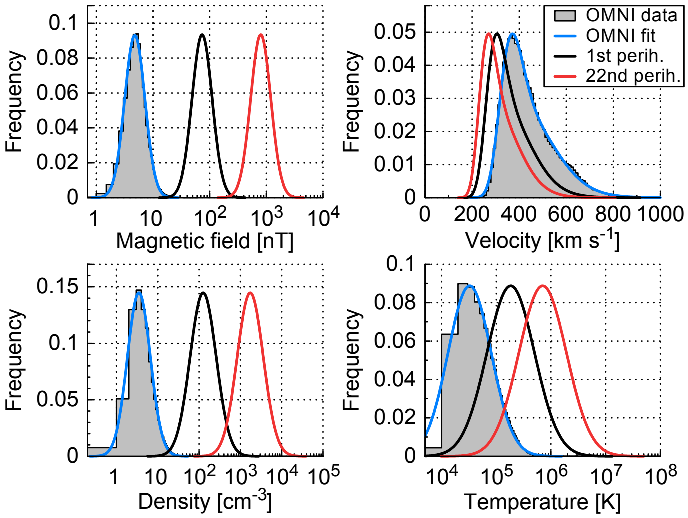

Fig. 14. Frequency distributions of the four solar-wind parameters (same as in Figs. 1 and 2) and those estimated with the solar-wind model for PSP's 1st and 22nd (first closest) perihelion. In these Figures the frequencies of both extrapolated curves are scaled for visibility to the same height as the 1 au distribution.

(first closest) perihelion are plotted in Fig. 14. Again, we point out that the velocity and temperature distributions for the 22nd perihelion are only upper limits and the actual values to be encountered by PSP are expected to be smaller.

7. Discussion and summary

The scientific objective of this study, being part of the CGAUSS project – the German contribution to the WISPR instrument – is to model the solar-wind environment for the PSP mission to be launched mid 2018. For this purpose we started the development of the empirical solar-wind environment model for the near-ecliptic PSP orbit. We derived lognormal representations of the in situ near-Earth solar-wind data collected in the OMNI database, using the frequency distributions of the key solar-wind parameters, magnetic field strength, proton velocity, density, and temperature. Throughout the different analyses in our study, the velocity's frequency distribution is treated as a composition of a slow and a fast wind distribution. Each velocity part is fitted with a lognormal function, which allows for the overlap of both velocity ranges. The OMNI multi-spacecraft solar-wind data is intercalibrated and covers almost five solar cycles. It thus represents solar wind gathered at different phases of solar activity in the ecliptic plane. In the next step we investigated the yearly variation of the solar-wind distribution functions along with the SSN over 53 years and derived linear dependencies of the solar-wind parameters with the SSN. The radial dependencies of the solar-wind distribution functions were then analyzed, using Helios 1 and 2 data for the distance range 0.29–0.98 au in bins of 0.01 au, deriving power law fit functions that were used to scale the previously calculated SSN-dependent 1 au distribution fit functions to the PSP orbit, taking into account SSN predictions for the years 2018–2025, encompassing the prime mission up to the closest approach of 9.86 $R_\odot$. The reason for performing the analysis this way is based on the fact that the OMNI solar-wind database is much larger than the Helios database.

For determining solar-activity- and solar-distance-dependent relations for the median and mean solar-wind values, we could have used the simpler approach of combining the radial dependence of averaged Helios data with averaged 1 au OMNI data scaled with the SSN. It is expected that the results of a simpler analysis would have similar distance scaling results, as can be inferred from the exponents in Tables 3 and 4. However, in our study we are not only interested in averages but rather in bulk distributions, that is, the whole range of values that might occur. For the determination of the frequency distributions the use of the more complex fit model is important, because the distance between median and mean values determines the width of the lognormal distributions.

It is clear that the calculated distribution functions only represent first-order estimates of the real solar wind to be encountered by PSP. The solar-wind environment to be encountered will depend at times of PSP on the structure of the solar corona and underlying photospheric magnetic field and on the evolution and interaction of individual solar-wind streams and superimposed CMEs and shocks. However, the derived results are in good agreement with existing studies about near-Sun solar-wind magnetic field strengths and densities as shown in Sect. 6. The extrapolation results of the velocity and the temperature differ from the direct measurements seen in existing studies. This suggests that below about $20\,R_\odot$ PSP may dive into the region where the acceleration and heating of the solar wind is expected to occur (see Fig. 11). The near-Sun solar-wind velocity at PSP perihelion is also expected to be slower than our model estimates, because the solar wind is assumed to be accelerated up to the height of the Alfvénic critical surface, which is predicted to lie on average around $17\,R_\odot$ (e.g., Sittler & Guhathakurta 1999; Exarhos & Moussas 2000), scaling with solar activity within a range of between $15\,R_\odot$ at solar minimum and $30\,R_\odot$ at solar maximum (Katsikas et al. 2010; Goelzer et al. 2014).

We have not specifically investigated the occurrences of extreme solar-wind parameters caused by CMEs or enhanced values due to stream interaction or co-rotating interaction regions. The Helios solar-wind measurements plotted over radial distance in Fig. 7 show several extreme values far above the usual solar-wind velocities, which are associated with individual CMEs. The results by Sachdeva et al. (2017) indicate that due to solar-wind drag, the speeds of fast CMEs will commonly slow down substantially from early distances of a few solar radii. Therefore, it is expected that PSP will encounter CMEs with much higher speeds than those observed during the Helios mission. Also, the magnetic field, density and temperature values are expected to be much larger than in the average solar wind in individual fast-shock-associated CME events. PSP will thus also substantially improve our understanding of the near-Sun evolution of CMEs and their expansion with radial distance.

With the resulting CGAUSS empirical solar-wind model for PSP, the following main results for the bulk solar-wind parameters and estimations for their median values at PSP's first perihelion in 2018 at a solar distance of 0.16 au and at PSP's closest perihelia beginning in 2024 at 0.046 au ($9.86\,R_\odot$) are obtained:

- The dependency of the magnetic field strength on solar activity and radial distance appears to be valid above $20\,R_\odot$, however near PSP's closest perihelia, the actual values might be found to be slightly higher.
- The estimated magnetic field strength median values obtained from relation (12) for PSP's 1st and 22nd perihelion are 87 nT and 943 nT.
- The radial dependencies of the proton velocity median values for slow and fast solar wind (14) appear to be valid above about $20\,R_\odot$ solar distance; below they overestimate the actual solar wind velocities obtained from remote measurements. The share of their frequency distributions to the overall solar-wind velocity distribution (5) depends on solar activity with their balance relation (16). Thus, at solar minimum, with a SSN of around zero, the slow-wind component contributes about 64 % and drops to 28 % during solar maximum conditions with a SSN around 200.
- The calculated median velocity values for PSP's 1st and 22nd perihelion are $340\,\mathrm{km\,s^{-1}}$ and $290\,\mathrm{km\,s^{-1}}$.
- The proton density relation appears to be valid throughout the full PSP orbital distance range, even down to about $8\,R_\odot$.
- The estimated density median values obtained from relation (17) for PSP's 1st and 22nd perihelion are $214\,\mathrm{cm^{-3}}$ and $2951\,\mathrm{cm^{-3}}$.
- The derived correlation function for the proton temperature appears to provide overly high temperature values around PSP's closest perihelion in comparison to coronal measurements.
- The estimated temperature median values obtained from relation (19) for PSP's 1st and 22nd perihelion are 503 000 K and 1 930 000 K.

The results of the modeled solar-wind environment will be useful to help optimize the WISPR and in situ instrument science plannings and PSP mission operations. This also applies for the Heliospheric Imager (SoloHI) (Howard et al. 2013) and the in situ instruments on board the Solar Orbiter spacecraft.

Acknowledgements. The authors acknowledge support of the Coronagraphic German and US SolarProbePlus Survey (CGAUSS) project for WISPR by the German Aerospace Center (DLR) under grant 50 OL 1601 as national contribution to the Parker Solar Probe mission. The authors thank the Helios and OMNI PIs/teams for creating and making available the solar wind in situ data. The Helios and the OMNI data are supplied by the NASA Space Science Data Coordinated Archive and the Space Physics Data Facility at NASA's Goddard Space Flight Center. Additional thanks for maintaining and providing the international sunspot number series goes to the World Data Center – Sunspot Index and Long-term Solar Observations at the Solar Influences Data Analysis Center, Royal Observatory of Belgium. The PSP SPICE kernel was kindly provided by Angelos Vourlidas. The authors thank the referee for the careful review of this manuscript and helpful comments and suggestions.

References

Bale, S. D., Goetz, K., Harvey, P. R., et al. 2016, Space Sci. Rev., 204, 49
Balogh, A., Bothmer, V., Crooker, N. U., et al. 1999, Space Sci. Rev., 89, 141
Banaszkiewicz, M., Axford, W. I., & McKenzie, J. F. 1998, A&A, 337, 940
Belcher, J. W., Slavin, J. A., Armstrong, T. P., et al. 1991, Mercury Orbiter: Report of the Science Working Team (Washington, United States)
Biermann, L. 1951, ZAp, 29, 274
Billings, D. E. 1959, ApJ, 130, 961
Bothmer, V. & Daglis, I. A. 2007, Space Weather – Physics and Effects (Praxis Publishing)
Bothmer, V. & Schwenn, R. 1996, Advances in Space Research, 17
Bothmer, V. & Schwenn, R. 1998, Annales Geophysicae, 16, 1
Bougeret, J.-L., King, J. H., & Schwenn, R. 1984, Sol. Phys., 90, 401
Bruno, R., Villante, U., Bavassano, B., Schwenn, R., & Mariani, F. 1986, Sol. Phys., 104, 431
Burt, J. & Smith, B. 2012, in 2012 IEEE Aerospace Conference, 1–13
Colin, L. 1980, J. Geophys. Res., 85, 7575
Domingo, V., Fleck, B., & Poland, A. I. 1995, Sol. Phys., 162, 1
Exarhos, G. & Moussas, X. 2000, A&A, 356, 315
Feldman, W. C., Asbridge, J. R., Bame, S. J., & Gosling, J. T. 1978, J. Geophys. Res., 83, 2177
Forsyth, R. J., Bothmer, V., Cid, C., et al. 2006, Space Sci. Rev., 123, 383
Fox, N. J., Velli, M. C., Bale, S. D., et al. 2015, Space Sci. Rev.
Goelzer, M. L., Schwadron, N. A., & Smith, C. W. 2014, Journal of Geophysical Research (Space Physics), 119, 115
Gosling, J. T., Hildner, E., MacQueen, R. M., et al. 1974, J. Geophys. Res., 79, 4581
Gringauz, K. I., Bezrokikh, V. V., Ozerov, V. D., & Rybchinskii, R. E. 1960, Soviet Physics Doklady, 5, 361
Gurnett, D. A., Kurth, W. S., Burlaga, L. F., & Ness, N. F. 2013, Science, 341, 1489

Hathaway, D. H. & Upton, L. A. 2016, Journal of Geophysical Research (Space Physics), 121, 10
Hellinger, P., Matteini, L., Štverák, Š., Trávníček, P. M., & Marsch, E. 2011, Journal of Geophysical Research (Space Physics), 116, A09105
Hellinger, P., TráVníček, P. M., Štverák, Š., Matteini, L., & Velli, M. 2013, Journal of Geophysical Research (Space Physics), 118, 1351
Howard, R. A., Vourlidas, A., Korendyke, C. M., et al. 2013, in Proc. SPIE, Vol. 8862, Solar Physics and Space Weather Instrumentation V, 88620H
Kasper, J. C., Abiad, R., Austin, G., et al. 2016, Space Sci. Rev., 204, 131
Kasper, J. C., Stevens, M. L., Korreck, K. E., et al. 2012, ApJ, 745, 162
Katsikas, V., Exarhos, G., & Moussas, X. 2010, Advances in Space Research, 46, 382
Kilpua, E. K. J., Madjarska, M. S., Karna, N., et al. 2016, Sol. Phys., 291, 2441
King, J. H. & Papitashvili, N. E. 2005, Journal of Geophysical Research (Space Physics), 110, A02104
Lazarus, A. J. 2000, Science, 287, 2172
Leblanc, Y., Dulk, G. A., & Bougeret, J.-L. 1998, Sol. Phys., 183, 165
Lepping, R. P., Acũna, M. H., Burlaga, L. F., et al. 1995, Space Sci. Rev., 71, 207
Liebenberg, D. H., Bessey, R. J., & Watson, B. 1975, Sol. Phys., 44, 345
Mariani, F., Ness, N. F., Burlaga, L. F., Bavassano, B., & Villante, U. 1978, J. Geophys. Res., 83, 5161
McComas, D. J., Acton, L. W., Balat-Pichelin, M., et al. 2008, Solar Probe Plus: Report of the Science and Technology Definition Team, Tech. Rep. NASA/TM-2008-214161, National Aeronautics and Space Administration, Goddard Space Flight Center, Greenbelt, MD
McComas, D. J., Alexander, N., Angold, N., et al. 2016, Space Sci. Rev., 204, 187
McComas, D. J., Bame, S. J., Barraclough, B. L., et al. 1998, Geophys. Res. Lett., 25, 1
McGregor, S. L., Hughes, W. J., Arge, C. N., Odstrcil, D., & Schwadron, N. A. 2011a, Journal of Geophysical Research (Space Physics), 116, A03106
McGregor, S. L., Hughes, W. J., Arge, C. N., Owens, M. J., & Odstrcil, D. 2011b, Journal of Geophysical Research (Space Physics), 116, A03101
Müller, D., Marsden, R. G., St. Cyr, O. C., & Gilbert, H. R. 2013, Sol. Phys., 285, 25
Neugebauer, M. & Snyder, C. W. 1966, J. Geophys. Res., 71, 4469
Ogilvie, K. W., Chornay, D. J., Fritzenreiter, R. J., et al. 1995, Space Sci. Rev., 71, 55
Parker, E. N. 1958, ApJ, 128, 664
Richardson, I. G. & Cane, H. V. 2012, Journal of Space Weather and Space Climate, 2, A2
Rosenbauer, H., Schwenn, R., Marsch, E., et al. 1977, Journal of Geophysics Zeitschrift Geophysik, 42, 561
Russell, C. T., Mewaldt, R. A., Luhmann, J. G., et al. 2013, ApJ, 770, 38
Sachdeva, N., Subramanian, P., Vourlidas, A., & Bothmer, V. 2017, Sol. Phys., 292, 118
Sanchez-Diaz, E., Rouillard, A. P., Lavraud, B., et al. 2016, Journal of Geophysical Research (Space Physics), 121, 2830
Schwenn, R. 1983, in NASA Conference Publication, Vol. 228, NASA Conference Publication
Schwenn, R. 1990, Large-Scale Structure of the Interplanetary Medium (Springer Berlin Heidelberg), 99–181
Sheeley, N. R., Wang, Y.-M., Hawley, S. H., et al. 1997, ApJ, 484, 472
Sheeley, Jr., N. R., Howard, R. A., Michels, D. J., et al. 1985, J. Geophys. Res., 90, 163
SILSO World Data Center. 1963–2016, International Sunspot Number Monthly Bulletin and online catalogue
Sittler, Jr., E. C. & Guhathakurta, M. 1999, ApJ, 523, 812
Smith, E. J. & Balogh, A. 2003, in American Institute of Physics Conference Series, Vol. 679, Solar Wind Ten, ed. M. Velli, R. Bruno, F. Malara, & B. Bucci, 67–70
Stone, E. C., Frandsen, A. M., Mewaldt, R. A., et al. 1998, Space Sci. Rev., 86, 1
Veselovsky, I. S., Dmitriev, A. V., & Suvorova, A. V. 2010, Cosmic Research, 48, 113
Vourlidas, A., Howard, R. A., Plunkett, S. P., et al. 2016, Space Sci. Rev., 204, 83
Wang, Y.-M., Sheeley, N. R., Socker, D. G., Howard, R. A., & Rich, N. B. 2000, J. Geophys. Res., 105, 25133

8 Helios radial line-up passings

have a look into Schwenn1984...

To derive the radial dependence of the solar wind parameters directly, we look at the passings when both Helios spacecraft were radially lined up. In these cases they flew through the same solar wind at different solar distances.
(This eliminates the bias of averaging over slow and fast wind streams, like the described model does.)
see also Schwenn (1990) p. 156 + p. 122...

we compare these independently derived radial fit functions to those obtained from the averaging over all solar wind types...

There were eight passings when both Helios spacecraft were radially lined-up (see Figure 8.1). These points

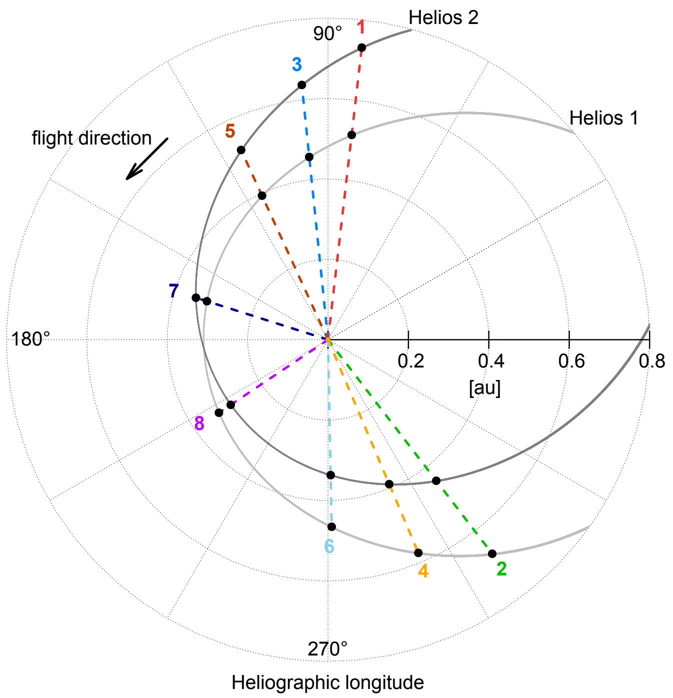

Figure 8.1 Schema of the eight spacecraft line-up positions of both Helios probes on their respective orbits. make B&W... combine with fig 5.15? calibrate text size

in time, when both probes had no separation in heliographic longitude, are derived from Helios 1 and Helios 2 daily trajectory data (for the data source see Section XX). The data is linear interpolated to get an hourly resolution. The resulting points in time together with solar distances are listed in Table 8.1.

The last two passings were merely one week apart and the Helios probes flew almost without radial separation because Helios 2 overtook Helios 1 during its perihelion. As we want to analyze the same solar wind at different solar distances, we exclude the passings 7 and 8 from further analyses.

The passing longitude is not the same as the longitude where the solar wind is detected by both spacecraft consecutively. A passing occurs shortly before the points in time when both spacecraft observe the same solar wind. For the outer probe this point in time is shifted by the solar wind's travel time. The travel time depends on the solar wind's velocity and its distance traveled.

Based on the obtained spacecraft line-up time t_0 one can calculate the offset times t_1 and t_2 when the inner and outer spacecraft pass by the same solar wind (see Figure 8.2). At the solar wind line-up longitude the

Table 8.1 Times when both Helios probes had no separation in heliographic longitude. Their solar distances (inner spacecraft r_1, outer spacecraft r_2) were in the range 0.291–0.731 au and the maximal inter-probe radial distance dr was 0.229 au. errors in au...

Passing	Date	Time	Inner s/c	r_1 [au]	r_2 [au]	dr [au]
1	1976-03-09	00:00	Helios 1	0.513	0.731	0.219
2	1976-05-02	14:00	Helios 2	0.442	0.671	0.229
3	1976-09-19	10:00	Helios 1	0.457	0.637	0.180
4	1976-10-31	11:00	Helios 2	0.390	0.576	0.186
5	1977-04-02	12:00	Helios 1	0.394	0.519	0.125
6	1977-04-30	23:00	Helios 2	0.337	0.465	0.128
7	1977-10-18	06:00	Helios 1	0.316	0.345	0.029
8	1977-10-25	19:00	Helios 2	0.291	0.327	0.035

condition

$$t_2 = t_1 + t_{sw} \tag{8.1}$$

holds. As the offset times depend on the solar wind travel time between the probes, we need knowledge of the solar wind velocity v for their calculation: $t_{sw} = \mathrm{d}r/v$, with the mean radial separation distance dr between the probes.

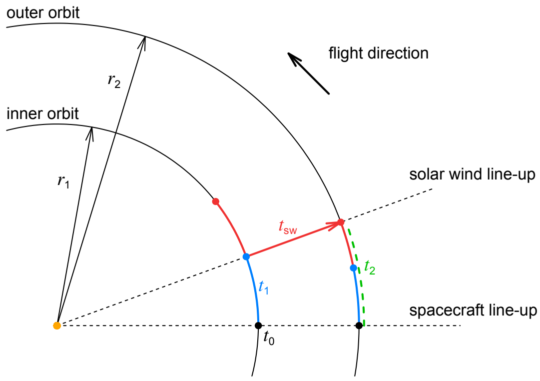

Figure 8.2 Illustration of the solar wind line-up longitude situation with the spacecraft line-up time t_0, the offset times t_1, t_2 (at which the spacecraft measure the same solar wind) and the solar wind travel time t_{sw}. combine with fig 5.14?

For the calculation of t_1 we recall the third Kepler law

$$\frac{{T_1}^2}{{T_2}^2} = \frac{{a_1}^3}{{a_2}^3} \tag{8.2}$$

with the orbital periods T_1, T_2 and the semi-major axes a_1, a_2. The assumption of circular orbits (why? what error size?) leads to

$$\frac{{t_1}^2}{(t_1 + t_{sw})^2} = \frac{{r_1}^3}{{r_2}^3}$$

$$\Leftrightarrow \qquad t_1 = t_{sw}\left(\left(\frac{r_1}{r_2}\right)^{\frac{3}{2}} - 1\right)^{-1} \tag{8.3}$$

and finally the offset time t_1 only depends on the variable solar wind travel time t_{sw}.

Due to uncertainties in the travel time t_{sw} (the solar wind speed v is obviously not a constant) the exact calculation of t_1 is imprecise. To get a reliable result we perform two iterations calculating the offset time from the average velocity $\bar{v}$ of the surrounding 2-day period. We use the velocity $\bar{v}_0$ around t_0 to calculate the offset time t'_1 as a first estimate. As the velocity $\bar{v}'_1$ at t'_1 is certainly different, we use this velocity to refine the value and obtain t_1. Hence deriving the velocity $\bar{v}_1$ enables us to calculate the solar wind travel time t_{sw}.

The average velocities are obtained from the hourly merged (mag?) and (plasma?) Helios data set (see Section XX). The resulting offset times and velocities of both iterations together with the travel times are listed in Table 8.2.

Table 8.2 The two iterations of the derived offset times and average velocities. The resulting solar wind travel times have durations of 11–28 hours. errors...

Passing	Inner s/c	v_0 [km/s]	t'_1 [h]	v'_1 [km/s]	t_1 [h]	v_1 [km/s]	t_{sw} [h]
1	Helios 1	659.3	19.6	656.9	19.7	656.9	13.9
2	Helios 2	436.4	25.1	370.9	29.5	356.7	26.7
3	Helios 1	482.6	24.0	444.0	26.1	413.8	18.1
4	Helios 2	302.3	32.2	279.9	34.8	278.3	27.8
5	Helios 1	507.3	20.0	474.8	21.4	473.5	11.0
6	Helios 2	321.2	26.6	392.6	21.7	367.8	14.5

For the solar wind line-up longitude condition (8.1) holds. For all other positions the solar wind measured by the inner spacecraft will not arrive the outer orbit position at the same time as the outer spacecraft does (see Figure 8.3).

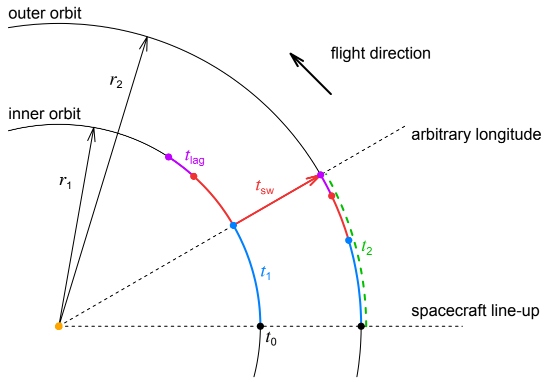

Figure 8.3 Illustration like Figure 8.2 but for arbitrary longitude situations a lag time t_{lag} comes into play. merge with fig 5.14?

Either the spacecraft (negative lag time) or the solar wind (positive lag time) already have passed this position:

$$t_2 = t_1 + t_{sw} + t_{lag}. \tag{8.4}$$

This lag time t_{lag} is the time difference at which the solar wind is probed by both spacecraft. At the spacecraft line-up longitude ($t_1 = t_2 = 0$) the lag time equals the solar wind travel time and at the solar wind line-up longitude the lag time is zero.

We choose to look at time periods (instead of points in time) around the offset times to derive average solar wind parameters. This helps reducing the influence of solar wind fluctuations.

We define the period duration boundaries as when the lag time t_{lag} is in the range ±24 h. For the outer spacecraft these periods are almost twice as long as for the inner spacecraft. The calculated period start and end hours (relative to t_0) for both spacecraft are listed in Table 8.3 together with the data coverage of these periods.

For period 3 the combined data coverage of the four solar wind parameters is only 16 % (Helios 1) and 10 % (Helios 2) respectively. We consider this as insufficient for the continuing analysis and therefore also omit period 3.

Table 8.3 Derived period start and end hours for both spacecraft in relation to the longitude line-up time t_0. The corresponding combined data coverage within that period of the magnetic field, velocity, density and temperature is listed as well. instead duration! errors...

Period	Inner spacecraft				Outer spacecraft		
	s/c	Start [h]	End [h]	Coverage [%]	Start [h]	End [h]	Coverage [%]
1	Helios 1	-14.4	53.8	73	-24.6	91.6	99
2	Helios 2	3.1	58.3	89	5.8	109.0	88
3	Helios 1	-9.2	65.1	16	-15.1	107.2	10
4	Helios 2	4.8	65.2	59	8.5	117.0	87
5	Helios 1	-25.5	68.3	89	-38.5	103.3	88
6	Helios 2	-15.3	61.7	93	-24.8	100.1	92

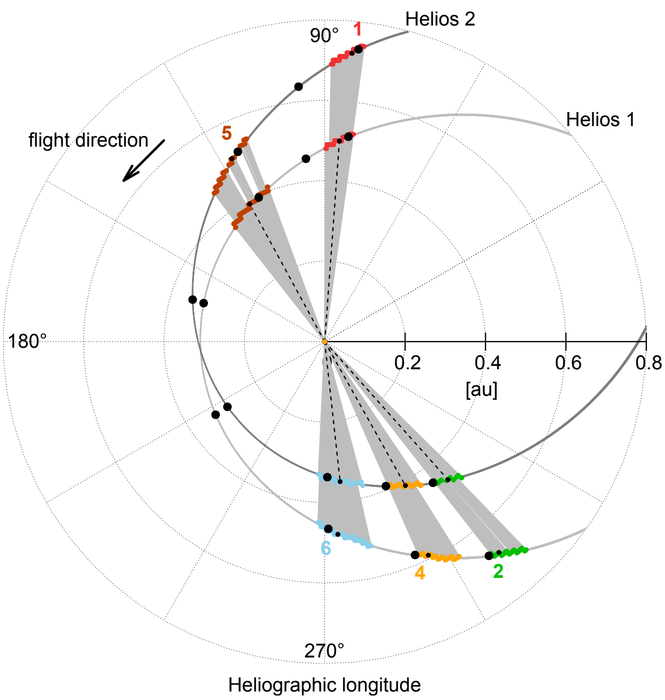

Figure 8.4 Scheme of the line-up periods of both Helios spacecraft on their respective orbits. The corresponding orbit sections which we consider in our analysis are marked in color. These sections span the positions where both spacecraft observed the same solar wind with a maximal lag time of ±24 hours. bw figure?? dotted lines?

The five remaining periods are marked in Figure 8.4.

The average values of the four parameters magnetic field B, velocity v, density n and temperature T are listed in Table 8.4.

If we compare both, the inner solar wind sections together with their outer counterparts, they indeed appear to have a similar shape apart from the time shift (see Figure 8.5) (name definite features...). This confirmes that they indeed are parts of the same solar wind structures.
maybe figures of all into Appendix?...

the comparison to the sw model's mean value at the individual distances lets us classify the solar wind types...

Period 1 HSS
Period 2 medium–LSS
Period 4 LSS
Period 5 medium–HSS
Period 6 LSS–HSS

We obtained the mean parameter values for the inner and outer solar wind sections. As with the overall radial dependency before, these two points are fitted to the exponential regression fit function $X(r) = X_0\, r^{cx}$

Table 8.4 Average values of the four solar wind parameters magnetic field, velocity, density and temperature for the individual periods and spacecraft. errors...

Period	Inner spacecraft					Outer spacecraft			
	s/c	B [nT]	v [km/s]	n [cm^{-3}]	T [K]	B [nT]	v [km/s]	n [cm^{-3}]	T [K]
1	Helios 1	17.04	646.4	12.0	367 300	8.93	602.8	6.7	244 000
2	Helios 2	15.77	356.4	38.8	122 400	12.05	390.2	17.7	117 200
4	Helios 2	15.18	281.3	108.0	46 000	10.64	298.6	46.1	30 400
5	Helios 1	28.80	521.3	45.9	337 800	18.73	530.3	24.4	282 000
6	Helios 2	29.57	402.4	82.5	271 900	14.71	432.6	35.7	199 100

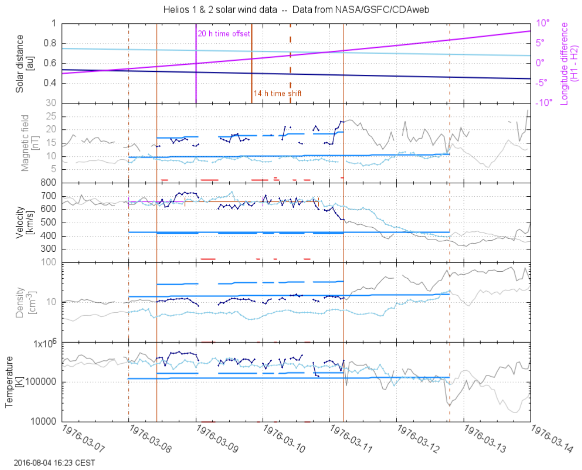

Figure 8.5 Measured solar wind parameters B, v, n, and T of both spacecraft in the period 1. Also plotted is the spacecraft's separation in heliographic longitude. offset time, time shift; expected value from the radial sw model... remove date... remove solar distance... adjust text size...

(see Section XX. The resulting fit coefficients for each period are listed in Table 8.5.
why is it better to fit the period's mean values than the whole period?...
we fit the periods' mean value rather than the whole periods, because...

Table 8.5 Radial fit functions $B(r)$, $v(r)$, $n(r)$ and $T(r)$ for each period. or only the variables into table? error sizes...

Period	$B(r) = B_0\, r^{c_B}$ [nT]	$v(r) = v_0\, r^{c_v}$ [km/s]	$n(r) = n_0\, r^{c_n}$ [cm^{-3}]	$T(r) = T_0\, r^{c_T}$ [K]
1	$4.88\, r^{-1.815}$	$564.7\, r^{-0.196}$	$3.9\, r^{-1.647}$	$166\,500\, r^{-1.148}$
2	$9.50\, r^{-0.654}$	$442.6\, r^{0.220}$	$8.9\, r^{-1.902}$	$112\,800\, r^{-0.106}$
4	$6.79\, r^{-0.900}$	$322.0\, r^{0.151}$	$15.7\, r^{-2.155}$	$18\,000\, r^{-1.047}$
5	$5.99\, r^{-1.649}$	$554.8\, r^{0.065}$	$4.6\, r^{-2.423}$	$174\,700\, r^{-0.692}$
6	$3.22\, r^{-2.108}$	$506.5\, r^{0.219}$	$5.7\, r^{-2.533}$	$101\,000\, r^{-0.941}$
weigthed by duration mean functions				
mean of sw model (update)	$6.078\, r^{-1.563}$	$435.5\, r^{0.04955}$	$7.613\, r^{-2.032}$	$97\,050\, r^{-0.8002}$

The fit curves show noticeable deviations from the model's mean fit (see Figure 8.6). maybe 4-panel figure?; maybe figures of all into Appendix?
The observed deviations are as expected from these types of solar wind. ...are they? analyze each in detail... argue from sw type; slow, medium and fast type; check their position relative to the mean curve...

results:
features of calculated line-up periods match.
their derived fit functions scatter within (acceptable?) margin around model's radial mean, backing its applicability.

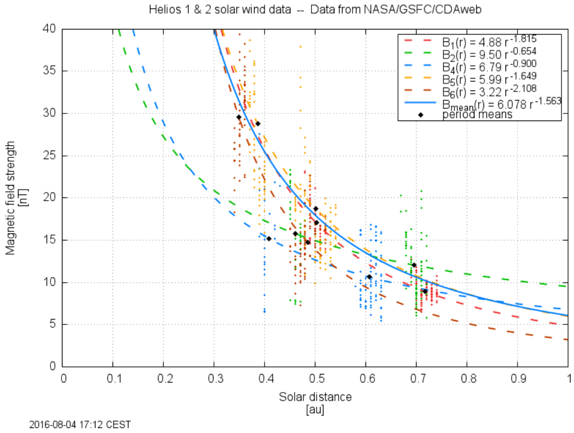

Figure 8.6 Fit curves of the radial magnetic field. The fits are based on the mean values (meanr,meanB; black points) of the line-up periods. build pdf figure... remove date... adjust text size... 4-figure?

9 Results, discussion and conclusions

already in chapters:
results
discussion
conclusions

end matter:
summary
outlook

Prediction:
Long-term solar wind parameter predictions fron SSN
Link from near-Sun solar wind measurements to Kp impact
Link from near-Sun structure (CMEs, CIRs) measurements to Kp impact

10 Summary and outlook

Outlook
DSCOVR data (advantages over ACE? gain?)
anticipated Solar Probe Plus data (near-Sun data)

other possible space weather missions: sub-L1 (earlier in situ CME magnitude warning) and L5 (early CME velocity and arrival warning)
I built an empirical solar wind model for the ecliptical inner heliosphere which accounts for variations in time (season and solar cycle) and space (solar distance).

Using the SSN prediction the model allows the forecast and extrapolation of the solar wind, which will occur during the SPP mission's first near-Sun perihela in mid-2018.

A Physics

A.1 Electromagnetism

Electromagnetism is one of the four fundamental forces at the common level of energy. In all situations examined in this thesis (sw plasma, magnetosphere) it is by far the strongest force and the others can be neglected.

The Lorentz force: $\mathbf{F} = q(\mathbf{E} + \mathbf{v} \times \mathbf{B})$

The Maxwell equations in differential notation:

$$\operatorname{div} \mathbf{B} = 0 \tag{A.1}$$
$$\operatorname{div} \mathbf{D} = \rho \tag{A.2}$$
$$\operatorname{rot} \mathbf{H} = \mathbf{j} + \dot{\mathbf{D}} \tag{A.3}$$
$$\operatorname{rot} \mathbf{E} = -\dot{\mathbf{B}} \tag{A.4}$$

With the magnetic flux density $\mathbf{B}$ (aka magnetic field), the electric displacement field $\mathbf{D}$, the charge density ρ, the magnetic field $\mathbf{H}$, the electric field $\mathbf{E}$ and the current density $\mathbf{j}$.

A.2 Solar wind pressures

The magnetic energy density w_{mag} is also the magnetic pressure p_{mag}

$$w_{\mathrm{mag}} = p_{\mathrm{mag}} \tag{A.5}$$
$$= \frac{B^2}{2\mu_0}\,. \tag{A.6}$$

dynamic pressure $p_{\mathrm{dyn}} = \rho v^2$
thermal pressure $p_{\mathrm{therm}} = nk_{\mathrm{B}}T$
magnetic pressure $p_{\mathrm{mag}} = B^2/(2\mu_0)$ (see above...)
ram pressure??

A.3 Plasma beta

In MHD the magnetic energy density behaves like an additional pressure that adds to the gas pressure of a plasma (Wikipedia; find alternative source...).

The ratio of the thermal pressure $p = nk_{\mathrm{B}}T$ to the magnetic pressure $p_{\mathrm{mag}} = \frac{B^2}{2\mu_0}$ is called plasma beta

$$\beta = \frac{p}{p_{\mathrm{mag}}} \tag{A.7}$$
$$= \frac{2\mu_0 n k_{\mathrm{B}} T}{B^2} \tag{A.8}$$

with the number density n.
$\beta \ll 1$: "cold" plasma; magnetic field contains plasma (magnetic clouds)
$\beta \geq 1$: "warm" plasma; plasma keeps magnetic field
plasma beta see (Kivelson & Russell 1995, p. 50)
typical *beta*-values for solar wind are in the range X–Y.

A.4 Alfvén waves

named after Hannes Alfvén...

There exists an incompressible wave mode which is a result of bending magnetic field lines called shear Alfvén wave.

In an ideal incompressible MHD plasma (viscosity $\mu = 0$ and electrical conductivity $\sigma = \infty$) the kinetic and magnetic energy density are of equal value:

$$\begin{aligned} w_{\mathrm{kin}} &= w_{\mathrm{mag}} \\ \frac{\rho v^2}{2} &= \frac{B^2}{2\mu_0} \end{aligned} \tag{A.9}$$

with the permeability constant

$$\mu_0 = 4\pi \cdot 10^{-7}\,\mathrm{N\,A^{-2}}$$

and the total mass density ρ of the charged plasma particles.

So waves propagate with the so-called Alfvén velocity

$$v_{\mathrm{A}} = \frac{|B|}{\sqrt{\mu_0 \rho}}\,. \tag{A.10}$$

Their phase velocity is

$$v_{\mathrm{ph}} = v_{\mathrm{A}} \cos(\theta) \tag{A.11}$$

with θ the angle between wave propagation direction (k) and magnetic field line (B). => Alfvén waves travel along magnetic field lines. Alfvén waves are characterized by periodic disturbances in the magnetic field perpendicular to its direction, in the electric field, in the plasma velocity and in the current density. They do not affect the plasma density, plasma pressure and magnetic field magnitude.

Additionally, there exist two types of compressional waves within MHD plasmas, the fast-mode wave and the slow-mode wave. The phase speeds of the three MHD waves meet $v_{\mathrm{fast}} \geq v_{\mathrm{A}} \geq v_{\mathrm{slow}}$.

Alfvén waves are dominant in regions that are open to the heliosphere.

Alfvén waves see (Kivelson & Russell 1995, pp. 51ff.)

Within average solar wind at 1 au their typical frequency is 1–4 per hour (cite?) ($v_{\mathrm{A}} = 53$ km/s for $B = 5.6$ nT and $\rho = 5.3\,\mathrm{cm}^{-3}$).

critical surfaces, solar wind acceleration...

A.5 Solar surface differential rotation

the solar rotation was first discovered from sunspots in 18XX?

Bartels (1934) set the synodic solar rotation period to 27 days for the definition of his solar rotation number. The Bartels' Rotation Number counts the solar rotations starting with 8 February 1832.

Carrington solar rotation period of 27.2753 days (Where Carrington Rotation Number is based upon, starting with November 9, 1853; Wikipedia...)

Solar surface rotation period at 16° latitude:

sidereal: 25.38 d (of 609.12 h Sun Fact Sheet...), synodic: 27.2753 d (derived)

rotation axis tilt (see next section)

The Sun's inner thermal convective circulation results in a differential rotation caused by transport of angular momentum away from the rotation axis.

The Sun's sidereal differential angular velocity best-fitting function with values as stated in (Sun Fact Sheet...)[1] is

$$\omega_\odot = A + B\sin^2(b) + C\sin^4(b) \tag{A.12}$$

[1] NASA's *Sun Fact Sheet* (`http://nssdc.gsfc.nasa.gov/planetary/factsheet/sunfact.html`, accessed 2016-08-19).

with the latitude b, the equatorial angular velocity $A = 14.37°/\mathrm{d}$, the coefficients $B = -2.33°/\mathrm{d}$ and $C = -1.56°/\mathrm{d}$ (see Figure A.1).

see Figure A.1

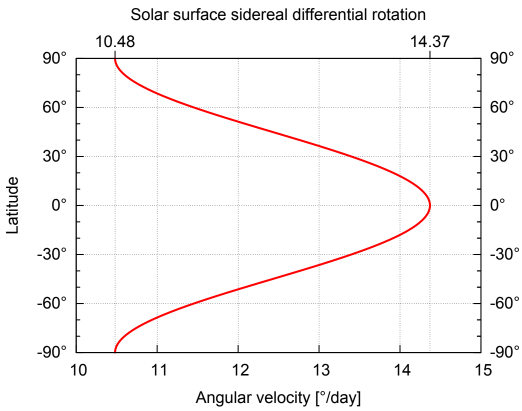

Figure A.1 Diagram of the sidereal solar surface differential rotation. It shows the angular velocity for different latitudes. remove sides...

Thus, the solar equatorial rotation period (sidereal) is

$$\begin{aligned} T_\odot^{\mathrm{eq}} &= 360°/A \\ &= 25.05\ \mathrm{d} \end{aligned} \tag{A.13}$$

and the synodic period is

$$\begin{aligned} T_\odot^{\mathrm{eq,syn}} &= 1/(1/T_\odot^{\mathrm{eq}} - 1/T_{\mathrm{Earth}}) \\ &= 26.90\ \mathrm{d} \end{aligned} \tag{A.14}$$

with the Earth's orbital rotation period $T_{\mathrm{Earth}} = 365.25$ d (1/100 Julian century).

Solar surface rotation period at equator
sidereal: 25.05 d (Sun Fact Sheet...), synodic: 26.90 d (derived)
Solar surface rotation period at poles:
sidereal: 34.35 d (diff. rot. formula), synodic: 37.92 d (derived)
are listed in Table A.1.

Table A.1 Solar surface rotation periods for equator, ±16° latitude and poles (sidereal and synodic).

	Equator [d]	±16° latitude [d]	Poles [d]
Sidereal	25.05	25.38	34.35
Synodic	26.90	27.2753[a]	37.92

[a]Carrington solar rotation period

The meridional circulation is the proposed equatorial updrift and polar downdrift - a result of Reynolds stress and convective transport (cite?).

A.6 Earth orbit geometry

orbit defines ecliptic

Earth orbit parameters (cite?):
semimajor axis: $a = 1.000001018$ au
eccentricity: $e = 0.0167086$ au
distance at perihelion: (formula cite?, accuracy?)

$$r_p = a(1 - e) \\ = 0.98329 \text{ au} \tag{A.15}$$

distance at aphelion:

$$r_p = a(1 + e) \\ = 1.0167 \text{ au} \tag{A.16}$$

for calculation of heliospheric distance see HORIZONS Web-Interface at http://ssd.jpl.nasa.gov/horizons.cgi

perihelion/aphelion times...

A.6.1 Solar distance

Sun-Earth distance over the course of the year.
In the year 2017 Earth's perihelion was on 5 January with a distance of −1.67 % from 1 au (Horizons On-Line Ephemeris System[2], Solar System Dynamics Group, Jet Propulsion Laboratory).
The cosine approximation

$$r_E(t) = 1 - 0.0167 \cdot \cos\left(2\pi\left(t - 2017 - \frac{5}{365}\right)\right), \tag{A.17}$$

with t in years, suffices for our accuracy requirements.

seasonal variation function:
$X_{avg}(t) = a\, r_E(t)^b$

A.6.2 Solar rotation axis tilt

The inclination of the solar equator to the ecliptic (tilt/obliquity) is $i_\odot = 7.25°$ (U.S. Nautical Almanac Office 2015).

the rotation axis is tilted from the ecliptic normal

Viewed from Earth the projected solar rotation axis tilt angle varies as the Earth is moving on its orbit.

At the time XX the angle is zero.

The projected tilt angle to Earth over the year is

Hapgood (1992):

$$\omega = 73.67 + 0.013\,958 * (today - 1850.0) \tag{A.18}$$

solar tilt over the year, see Figure A.2

A.6.3 Earth tilt

A.7 Coordinate systems

Coordinate systems used in this thesis:
GSE - Geocentric Solar Ecliptic
GSM - Geocentric Solar Magnetospheric

[2] http://ssd.jpl.nasa.gov/horizons.cgi

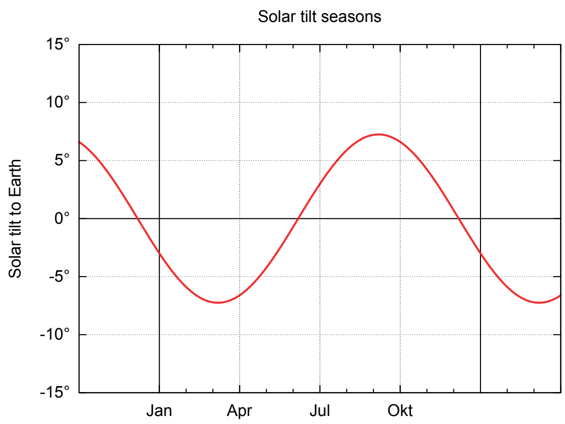

Figure A.2 Projected solar tilt angle over the year as viewed from Earth. remove sides...

HGI - Heliographic Inertial

refer to Hapgood (1992) for GSE and GSM

figures for GSE and GSM

A.7.1 Geocentric Solar Ecliptic

The Geocentric Solar Ecliptic (GSE) coordinates are
GSE - Geocentric Solar Ecliptic
X = Earth-Sun Line
Z = Ecliptic North Pole
GSE coordinates are used in ACE solar wind data, etc.

A.7.2 Geocentric Solar Magnetospheric

GSM - Geocentric Solar Magnetospheric
X = Earth-Sun Line
Z = Projection of dipole axis on GSE YZ plane

GSM is defined with a time dependent dipole axis.
the dipole axis orientation changes over time; at 1995 the northern pole was at $l = 288.59°$ and $b = 79.30°$; more recent year (2015)?... cite?

A.7.3 Heliographic Inertial

Heliographic Inertial (HGI) coordinates
HGI coordinates are Sun-centered with the z-axis directed along the solar rotation axis and directed northward of the solar equator. The solar equator plane is inclined 7.25° from the ecliptic.

HGI coordinates; latitude range $-7.25°$ to $-7.25°$
latitude variation (see Schwenn1990, p. 127)

B Math

B.1 Correlations

auto correlation
cross correlation
Pearson linear correlation
Spearman rank correlation
Correlation in Linear Regression: `http://www.stat.yale.edu/Courses/1997-98/101/correl.htm`

B.2 Lognormal distribution

This is a small summary about the lognormal probability distribution (Bronstein et al. 2000, p. 780). The lognormal distribution is the distribution of a random variable X if the logarithm of X conforms to a normal distribution. Its shape is highly asymmetric, however in a semi-log plot the Gaussian bell curve is recognizable (see the second panel of Figure B.1). Its probability density function is

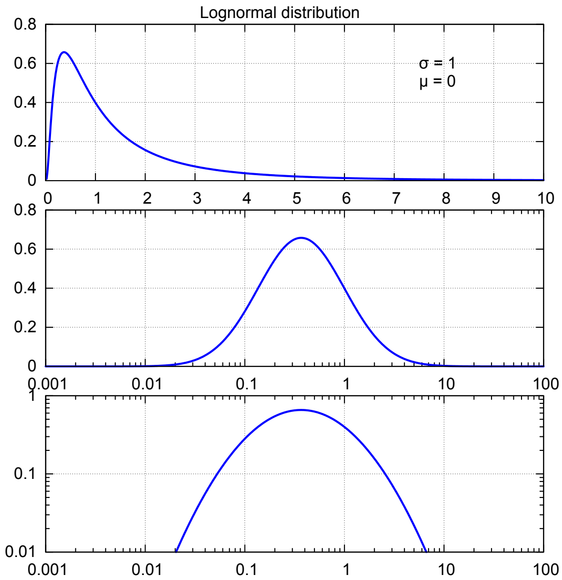

Figure B.1 The lognormal probability density function ($\sigma = 1, \mu = 0$) plotted in a linear, semi-log and log-log way. remove borders...

$$f(x) = \frac{1}{\sigma\sqrt{2\pi}x}\,\mathrm{e}^{-\frac{(\ln x-\mu)^2}{2\sigma^2}} \tag{B.1}$$

with the location (μ) and the shape parameter (σ). Changes in μ affect both the horizontal and vertical scaling of the function, whereas σ has an influence on its shape (see Figure B.2).

Because it is a probability distribution, its area is normalized

$$\int_0^\infty f(x)\mathrm{d}x = 1\,. \tag{B.2}$$

For a lognormally distributed random variable the geometric moments mean, standard deviation and variance are:

$$\mu_g = \mathrm{e}^{\mu},$$
$$\sigma_g = \mathrm{e}^{\sigma},$$
$$var_g = \mathrm{e}^{\sigma^2} \quad (!).$$

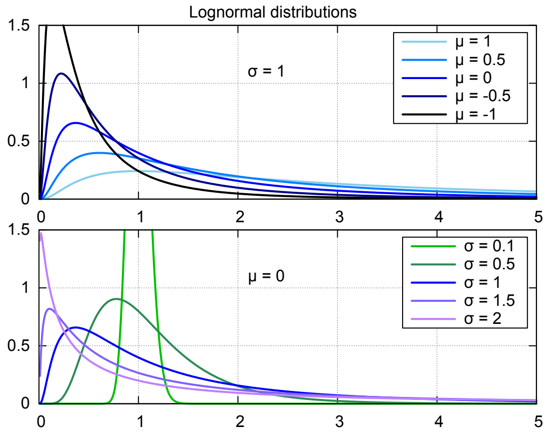

Figure B.2 Five lognormal distributions plotted with fixed σ (top) and fixed μ (bottom). remove borders...

Its arithmetic moments are:

$$\mu_\mathrm{a} = \mathrm{e}^{\mu+\frac{\sigma^2}{2}},$$
$$\sigma_\mathrm{a} = \mathrm{e}^{\mu+\frac{\sigma^2}{2}} \left(\mathrm{e}^{\sigma^2} - 1\right),$$
$$var_\mathrm{a} = \sigma_\mathrm{a}^2.$$

Other useful characteristics are the median and the mode

$$x_\mathrm{median} = \mathrm{e}^{\mu},$$
$$x_\mathrm{mode} = \mathrm{e}^{\mu-\sigma^2}.$$

Note that for the lognormal distribution its median is equal to its geometric mean.

Applications of lognormal distributions...

Most natural quantities which can only be positive are lognormally distributed. e.g. animal body sizes?, animal life expectancies, financial stock prices...; income distributions.

B.3 Goodness of fit

SSR – sum of squared residuals

$$SSR = \sum_i (y_i - f_i)^2 \tag{B.3}$$

data values y_i, fit function values f_i
SSR_red – reduced SSR, divided by number of degrees of freedom ν

$$SSR_\mathrm{red} = \frac{SSR}{\nu} \tag{B.4}$$

TSS – total sum of squares (in relation to the data mean)

$$TSS = \sum_i (y_i - \bar{y})^2 \tag{B.5}$$

with data mean $\bar{y}$

χ^2 – chi-square
χ^2_{red} – reduced chi-square, divided by number of degrees of freedom ν

R^2 – coefficient of determination
$0 \leq R^2 \leq 1$, "values can be less than zero"!. if $R^2 = 1$ -> ideal fit; if $R^2 = 0$ -> bad fit

$$R^2 = 1 - \frac{SSR}{TSS} \tag{B.6}$$

"In case of a single regressor, fitted by least squares, R2 is the square of the Pearson product-moment correlation coefficient relating the regressor and the response variable." cite from wikipedia

Kolmogorov-Smirnov K-S-Test

B.4 other

minimum variance analysis (MVA)
determining magnetic cloud configuration (Bothmer & Schwenn 1998)

hodogramm?
least-squares fit approximates mean linear regression
robust statistics
Non-parametric inferential statistical methods are mathematical procedures for statistical hypothesis testing which make no assumptions about the probability distributions of the variables being assessed. The most frequently used tests include - median - percentiles (quartiles) - Spearman's rank correlation coefficient
histogram
generalized mean http://en.wikipedia.org/wiki/Generalized_mean
normal distribution

C Glossary

C.1 Astronomical constants

Astronomical unit: 1 au = 149 597 870 700 m (U.S. Nautical Almanac Office 2015)
Solar mass: $M_\odot = 1.9884(2) \times 10^{30}$ kg (U.S. Nautical Almanac Office 2015)
Nominal solar radius (photosphere): $R_\odot = 695\,700$ km (Mamajek et al. 2015)
Sun escape velocity: $v_{\rm esc} = 617.6$ km/s (Sun Fact Sheet...)
Solar rotation axis tilt: $i_\odot = 7.25°$ (U.S. Nautical Almanac Office 2015)
Solar surface rotation period at equator, sidereal: 25.05 d (Sun Fact Sheet...)
Nominal solar effective temperature (photosphere): $T_{\rm eff\odot} = 5772$ K (Mamajek et al. 2015)

C.2 Abbreviations

Projects:

AFFECTS Advanced Forecast For Ensuring Communications Through Space
HELCATS Heliographic Cataloging, Analysis and Techniques Service
FP7 Framework Programme 7
CGAUSS Coronagraphic German And US SolarProbePlus Survey
OPTIMAP OPerational Tool for Ionospheric Mapping And Prediction

Spacecraft:
SPP – Solar Probe Plus
WISPR – Wide-field Imager for Solar Probe
ACE – Advanced Composition Explorer
MAG – Magnetometer
SWEPAM – Solar Wind Electron Proton Alpha Monitor
RTSW – Real Time Solar Wind
SDO – Solar Dynamics Observatory
SOHO – Solar and Heliospheric Observatory
STEREO – Solar TErrestrial RElations Observatory

Organizations:
NASA – National Aeronautics and Space Administration
SPDF – Space Physics Data Facility
NOAA – National Oceanic and Atmospheric Administration
SWPC – Space Weather Prediction Center
UGOE – University of Göttingen
IAG – Institute for Astrophysics Göttingen
GFZ – GeoForschungsZentrum
WDC-SILSO – World Data Center-Sunspot Index and Long-term Solar Observations

Sun:
DB – disparition brusques (disappearing filaments?; quiescent filaments?)
SSN – sunspot number

Solar wind:
IMF – interplanetary magnetic field
CME – coronal mass ejection
ICME – interplanetary coronal mass ejection
MC – magnetic cloud
HSS – high speed stream

CIR – corotating interaction region
SIR – stream interaction region
SB – sector boundary
BDE – bidirectional electrons
HCS – heliospheric current sheet
HPS – heliospheric plasma sheet

Earth:
Kp – planetare Kennziffer
Dst – Disturbance storm time

Coordinate systems:
GSE – geocentric solar ecliptic
GSM – geocentric solar magnetospheric

Theories and techniques:
MVA – minimum variance analysis
MHD – magnetohydrodynamic
GCS – Graduated Cylindrical Shell
CAT – CME Analysis Tool

References

Bahcall, J. N., Pinsonneault, M. H. & Wasserburg, G. J. 1995, *Solar models with helium and heavy-element diffusion*, Reviews of Modern Physics, 67, 781, http://adsabs.harvard.edu/abs/1995RvMP...67..781B.

Balogh, A. & Jokipii, J. R. 2009, *The Heliospheric Magnetic Field and Its Extension to the Inner Heliosheath*, Space Sci. Rev., 143, 85, http://adsabs.harvard.edu/abs/2009SSRv..143...85B.

Banaszkiewicz, M., Axford, W. I. & McKenzie, J. F. 1998, *An analytic solar magnetic field model*, Astron. Astrophys., 337, 940, http://adsabs.harvard.edu/abs/1998A%26A...337..940B.

Bartels, J. 1934, *Twenty-seven day recurrences in terrestrial-magnetic and solar activity, 1923-1933*, Terrestrial Magnetism and Atmospheric Electricity (Journal of Geophysical Research), 39, 201, http://adsabs.harvard.edu/abs/1934TeMAE..39..201B.

—. 1962, *Zur Vorgeschichte der Weltraumforschung*, Naturwissenschaften, 49, 313, http://adsabs.harvard.edu/abs/1962NW.....49..313B.

Bartels, J., Heck, N. H. & Johnston, H. F. 1939, *The three-hour-range index measuring geomagnetic activity*, Terrestrial Magnetism and Atmospheric Electricity (Journal of Geophysical Research), 44, 411, http://adsabs.harvard.edu/abs/1939TeMAE..44..411B.

Bartels, J. & Veldkamp, J. 1949, *International Data on Magnetic Disturbances, First Quarter, 1949*, J. Geophys. Res., 54, 295, http://adsabs.harvard.edu/abs/1949JGR....54..295B.

Belcher, J. W., Lazarus, A. J., McNutt, Jr., R. L. & Gordon, Jr., G. S. 1993, *Large-scale density structures in the outer heliosphere*, Advances in Space Research, 13, 41, http://adsabs.harvard.edu/abs/1993AdSpR..13...41B.

Biermann, L. 1951, *Kometenschweife und solare Korpuskularstrahlung*, Z. Astrophys., 29, 274, http://adsabs.harvard.edu/abs/1951ZA.....29..274B.

Billings, D. E. 1959, *Distribution of Matter with Temperature in the Emission Corona.*, Astrophys. J., 130, 961, http://adsabs.harvard.edu/abs/1959ApJ...130..961B.

Bothmer, V. 1993, *Die Struktur magnetischer Wolken im Sonnenwind: Zusammenhang mit eruptiven Protuberanzen und Einfluß auf die Magnetosphäre der Erde*, PhD thesis, Georg-August-Universität Göttingen, http://hdl.handle.net/11858/00-001M-0000-0014-F2C4-2.

Bothmer, V. & Daglis, I. A. 2007, *Space Weather – Physics and Effects* (Praxis Publishing), http://adsabs.harvard.edu/abs/2007swpe.book.....B, doi:10.1007/978-3-540-34578-7.

Bothmer, V. & Schwenn, R. 1998, *The structure and origin of magnetic clouds in the solar wind*, Annales Geophysicae, 16, 1, http://adsabs.harvard.edu/abs/1998AnGeo..16....1B.

Bronstein, I. N., Semendjajew, K. A., Musiol, G. & Mühlig, H. 2000, *Taschenbuch der Mathematik* (Verlag Harri Deutsch), https://books.google.de/books?id=zCKyuQAACAAJ.

Cane, H. V. & Richardson, I. G. 2003, *Interplanetary coronal mass ejections in the near-Earth solar wind during 1996-2002*, Journal of Geophysical Research (Space Physics), 108, 1156, http://adsabs.harvard.edu/abs/2003JGRA..108.1156C.

Carrington, R. C. 1859, *Description of a Singular Appearance seen in the Sun on September 1, 1859*, Mon. Not. R. Astron. Soc., 20, 13, http://adsabs.harvard.edu/abs/1859MNRAS..20...13C.

Christensen-Dalsgaard, J., Gough, D. O. & Thompson, M. J. 1991, *The depth of the solar convection zone*, Astrophys. J., 378, 413, http://adsabs.harvard.edu/abs/1991ApJ...378..413C.

Christensen-Dalsgaard, J., Dappen, W., Ajukov, S. V. et al. 1996, *The Current State of Solar Modeling*, Science, 272, 1286, http://adsabs.harvard.edu/abs/1996Sci...272.1286C.

Clark, D. H. & Stephenson, F. R. 1978, *An Interpretation of the Pre-Telescopic Sunspot Records from the Orient*, Quart. J. R. Astron. Soc., 19, 387, http://adsabs.harvard.edu/abs/1978QJRAS..19..387C.

Cranmer, S. R. & van Ballegooijen, A. A. 2005, *On the Generation, Propagation, and Reflection of Alfvén Waves from the Solar Photosphere to the Distant Heliosphere*, Astrophys. J., Suppl. Ser., 156, 265, http://adsabs.harvard.edu/abs/2005ApJS..156..265C.

Danziger, I. J. 1970, *The Cosmic Abundance of Helium*, Ann. Rev. Astron. Astrophys., 8, 161, http://adsabs.harvard.edu/abs/1970ARA%26A...8..161D.

Elliott, H. A., Jahn, J.-M. & McComas, D. J. 2013, *The Kp index and solar wind speed relationship: Insights for improving space weather forecasts*, Space Weather, 11, 339, http://adsabs.harvard.edu/abs/2013SpWea..11..339E.

Exarhos, G. & Moussas, X. 2000, *An estimation of the shape and temporal variation of the solar wind sonic, Alfvénic and fast magnetosonic surfaces*, Astron. Astrophys., 356, 315, http://adsabs.harvard.edu/abs/2000A%26A...356..315E.

Gringauz, K. I., Bezrokikh, V. V., Ozerov, V. D. & Rybchinskii, R. E. 1960, *A Study of the Interplanetary Ionized Gas, High-Energy Electrons and Corpuscular Radiation from the Sun by Means of the Three-Electrode Trap for Charged Particles on the Second Soviet Cosmic Rocket*, Soviet Physics Doklady, 5, 361, http://adsabs.harvard.edu/abs/1960SPhD....5..361G.

Gurnett, D. A., Kurth, W. S., Burlaga, L. F. & Ness, N. F. 2013, *In Situ Observations of Interstellar Plasma with Voyager 1*, Science, 341, 1489, http://adsabs.harvard.edu/abs/2013Sci...341.1489G.

Hapgood, M. A. 1992, *Space physics coordinate transformations - A user guide*, Planet. Space Sci., 40, 711, http://adsabs.harvard.edu/abs/1992P%26SS...40..711H.

Hathaway, D. H. 2015, *The Solar Cycle*, Living Reviews in Solar Physics, 12, 4, http://adsabs.harvard.edu/abs/2015LRSP...12....4H.

Hathaway, D. H. & Upton, L. A. 2016, *Predicting the amplitude and hemispheric asymmetry of solar cycle 25 with surface flux transport*, Journal of Geophysical Research (Space Physics), 121, 10, http://adsabs.harvard.edu/abs/2016JGRA..12110744H.

Joint Committee for Guides in Metrology. 2008, *JCGM 100: Evaluation of Measurement Data - Guide to the Expression of Uncertainty in Measurement*, Tech. rep., JCGM, https://www.bipm.org/en/publications/guides/gum.html.

King, J. H. & Papitashvili, N. E. 2005, *Solar wind spatial scales in and comparisons of hourly Wind and ACE plasma and magnetic field data*, Journal of Geophysical Research (Space Physics), 110, 2104, http://adsabs.harvard.edu/abs/2005JGRA..110.2104K.

Kivelson, M. G. & Russell, C. T. 1995, *Introduction to Space Physics* (Cambridge University Press), http://adsabs.harvard.edu/abs/1995isp..book.....K.

Leitner, M., Farrugia, C. J., Möstl, C. et al. 2007, *Consequences of the force-free model of magnetic clouds for their heliospheric evolution*, Journal of Geophysical Research (Space Physics), 112, 6113, http://adsabs.harvard.edu/abs/2007JGRA..112.6113L.

Lem, S. & Kandel, M. 1984, *His Master's Voice* (Houghton Mifflin Harcourt), http://books.google.de/books?id=nzgLf4zKph0C.

Liebenberg, D. H., Bessey, R. J. & Watson, B. 1975, *Coronal emission line profile observations at total solar eclipses. II - 30 May 1965 results, deconvolution and interpretation*, Solar Phys., 44, 345, http://adsabs.harvard.edu/abs/1975SoPh...44..345L.

Lockwood, M., Nevanlinna, H., Barnard, L. et al. 2014, *Reconstruction of geomagnetic activity and near-Earth interplanetary conditions over the past 167 yr - Part 4: Near-Earth solar wind speed, IMF, and open solar flux*, Annales Geophysicae, 32, 383, http://adsabs.harvard.edu/abs/2014AnGeo..32..383L.

Machol, J. L., Reinard, A. A., Viereck, R. A. & Biesecker, D. A. 2013, *Identification and replacement of proton-contaminated real-time ACE solar wind measurements*, Space Weather, 11, 434, http://adsabs.harvard.edu/abs/2013SpWea..11..434M.

Mamajek, E. E., Prsa, A., Torres, G. et al. 2015, *IAU 2015 Resolution B3 on Recommended Nominal Conversion Constants for Selected Solar and Planetary Properties*, ArXiv e-prints, arXiv:1510.07674, http://adsabs.harvard.edu/abs/2015arXiv151007674M.

Maunder, E. W. 1890, *Prof. Spoerer's researches on Sun-spots*, Mon. Not. R. Astron. Soc., 50, 251, http://adsabs.harvard.edu/abs/1890MNRAS..50..251S.

—. 1904, *Note on the distribution of sun-spots in heliographic latitude, 1874-1902*, Mon. Not. R. Astron. Soc., 64, 747, http://adsabs.harvard.edu/abs/1904MNRAS..64..747M.

McComas, D. J., Ebert, R. W., Elliott, H. A. et al. 2008, *Weaker solar wind from the polar coronal holes and the whole Sun*, Geophys. Res. Lett., 35, L18103, http://adsabs.harvard.edu/abs/2008GeoRL..3518103M.

Miesch, M. S. 2005, *Large-Scale Dynamics of the Convection Zone and Tachocline*, Living Reviews in Solar Physics, 2, 1, http://adsabs.harvard.edu/abs/2005LRSP....2....1M.

Neugebauer, M. & Snyder, C. W. 1966, *Mariner 2 Observations of the Solar Wind, 1, Average Properties*, J. Geophys. Res., 71, 4469, http://adsabs.harvard.edu/abs/1966JGR....71.4469N.

Newell, P. T., Sotirelis, T., Liou, K., Meng, C.-I. & Rich, F. J. 2007, *A nearly universal solar wind-magnetosphere coupling function inferred from 10 magnetospheric state variables*, Journal of Geophysical Research (Space Physics), 112, A01206, http://adsabs.harvard.edu/abs/2007JGRA..112.1206N.

Newell, P. T., Sotirelis, T., Liou, K. & Rich, F. J. 2008, *Pairs of solar wind-magnetosphere coupling functions: Combining a merging term with a viscous term works best*, Journal of Geophysical Research (Space Physics), 113, A04218, http://adsabs.harvard.edu/abs/2008JGRA..113.4218N.

Opher, M., Drake, J. F., Swisdak, M. et al. 2011, *Is the Magnetic Field in the Heliosheath Laminar or a Turbulent Sea of Bubbles?*, Astrophys. J., 734, 71, http://adsabs.harvard.edu/abs/2011ApJ...734...71O.

Opher, M., Drake, J. F., Zieger, B. & Gombosi, T. I. 2015, *Magnetized Jets Driven By the Sun: the Structure of the Heliosphere Revisited*, Astrophys. J., Lett., 800, L28, http://adsabs.harvard.edu/abs/2015ApJ...800L..28O.

Ossendrijver, M. 2003, *The solar dynamo*, Astron. Astrophys. Rev., 11, 287, http://adsabs.harvard.edu/abs/2003A%26ARv..11..287O.

Owens, M. J. & Forsyth, R. J. 2013, *The Heliospheric Magnetic Field*, Living Reviews in Solar Physics, 10, 5, http://adsabs.harvard.edu/abs/2013LRSP...10....5O.

Parker, E. N. 1958, *Dynamics of the Interplanetary Gas and Magnetic Fields.*, Astrophys. J., 128, 664, http://adsabs.harvard.edu/abs/1958ApJ...128..664P.

Pizzo, V. J. 1991, *The evolution of corotating stream fronts near the ecliptic plane in the inner solar system. II - Three-dimensional tilted-dipole fronts*, J. Geophys. Res., 96, 5405, http://adsabs.harvard.edu/abs/1991JGR....96.5405P.

Planck Collaboration, Ade, P. A. R., Aghanim, N. et al. 2016, *Planck 2015 results. XIII. Cosmological parameters*, Astron. Astrophys., 594, A13, http://adsabs.harvard.edu/abs/2016A%26A...594A..13P.

Richardson, I. G. & Cane, H. V. 2010, *Near-Earth Interplanetary Coronal Mass Ejections During Solar Cycle 23 (1996 - 2009): Catalog and Summary of Properties*, Solar Phys., 264, 189, http://adsabs.harvard.edu/abs/2010SoPh..264..189R.

—. 2012, *Near-earth solar wind flows and related geomagnetic activity during more than four solar cycles (1963-2011)*, Journal of Space Weather and Space Climate, 2, A2, http://adsabs.harvard.edu/abs/2012JSWSC...2A..02R.

Richardson, I. G., Cliver, E. W. & Cane, H. V. 2000, *Sources of geomagnetic activity over the solar cycle: Relative importance of coronal mass ejections, high-speed streams, and slow solar wind*, J. Geophys. Res., 105, 18203, http://adsabs.harvard.edu/abs/2000JGR...10518203R.

Richardson, J. D., Paularena, K. I., Lazarus, A. J. & Belcher, J. W. 1995, *Radial evolution of the solar wind from IMP 8 to Voyager 2*, Geophys. Res. Lett., 22, 325, http://adsabs.harvard.edu/abs/1995GeoRL..22..325R.

Richardson, J. D. & Smith, C. W. 2003, *The radial temperature profile of the solar wind*, Geophys. Res. Lett., 30, 1206, http://adsabs.harvard.edu/abs/2003GeoRL..30.1206R.

Rotter, T., Veronig, A. M., Temmer, M. & Vršnak, B. 2012, *Relation Between Coronal Hole Areas on the Sun and the Solar Wind Parameters at 1 AU*, Solar Phys., 281, 793, http://adsabs.harvard.edu/abs/2012SoPh..281..793R.

Russell, C. T. 2007, *The coupling of the solar wind to the Earth's magnetosphere*, ed. V. Bothmer & I. A. Daglis, Space Weather- Physics and Effects, 103, http://adsabs.harvard.edu/abs/2007swpe.book..103R.

Russell, C. T., Mewaldt, R. A., Luhmann, J. G. et al. 2013, *The Very Unusual Interplanetary Coronal Mass Ejection of 2012 July 23: A Blast Wave Mediated by Solar Energetic Particles*, Astrophys. J., 770, 38, http://adsabs.harvard.edu/abs/2013ApJ...770...38R.

Sánchez Almeida, J., Bonet, J. A., Viticchié, B. & Del Moro, D. 2010, *Magnetic Bright Points in the Quiet Sun*, Astrophys. J., Lett., 715, L26, http://adsabs.harvard.edu/abs/2010ApJ...715L..26S.

Schatten, K. H. & Sofia, S. 1987, *Forecast of an exceptionally large even-numbered solar cycle*, Geophys. Res. Lett., 14, 632, http://adsabs.harvard.edu/abs/1987GeoRL..14..632S.

Schatten, K. H., Wilcox, J. M. & Ness, N. F. 1969, *A model of interplanetary and coronal magnetic fields*, Solar Phys., 6, 442, http://adsabs.harvard.edu/abs/1969SoPh....6..442S.

Schröder, W., ed. 2004, Some aspects of the earlier history of solar-terrestrial physics: Zur Entstehung der solar-terrestrischen Physik.

Schwenn, R. 1983, *The average solar wind in the inner heliosphere: Structures and slow variations*, in NASA Conference Publication, Vol. 228, NASA Conference Publication, http://adsabs.harvard.edu/abs/1983NASCP.2280.489S.

Schwenn, R. 1990, *Large-Scale Structure of the Interplanetary Medium*, ed. R. Schwenn & E. Marsch, Physics of the Inner Heliosphere I, 99, http://adsabs.harvard.edu/abs/1990pihl.book...99S.

Sittler, Jr., E. C. & Guhathakurta, M. 1999, *Semiempirical Two-dimensional MagnetoHydrodynamic Model of the Solar Corona and Interplanetary Medium*, Astrophys. J., 523, 812, http://adsabs.harvard.edu/abs/1999ApJ...523..812S.

Temmer, M. & Nitta, N. V. 2015, *Interplanetary Propagation Behavior of the Fast Coronal Mass Ejection on 23 July 2012*, Solar Phys., 290, 919, http://adsabs.harvard.edu/abs/2015SoPh..290..919T.

Thompson, M. J., Christensen-Dalsgaard, J., Miesch, M. S. & Toomre, J. 2003, *The Internal Rotation of the Sun*, Ann. Rev. Astron. Astrophys., 41, 599, http://adsabs.harvard.edu/abs/2003ARA%26A..41..599T.

U.S. Nautical Almanac Office. 2015, *Astronomical Almanac for the Year 2016 and Its Companion, the Astronomical Almanac Online* (United States Department of Defense), https://books.google.de/books?id=Mc_VuQN_gVsC.

Vaquero, J. M. 2007, *Letter to the Editor: Sunspot observations by Theophrastus revisited*, Journal of the British Astronomical Association, 117, 346, http://adsabs.harvard.edu/abs/2007JBAA..117..346V.

Venzmer, M. S. & Bothmer, V. 2017, *Solar-wind predictions for the Parker Solar Probe orbit*, ArXiv e-prints, arXiv:1711.07534, http://adsabs.harvard.edu/abs/2017arXiv171107534V.

Vršnak, B., Temmer, M. & Veronig, A. M. 2007, *Coronal Holes and Solar Wind High-Speed Streams: I. Forecasting the Solar Wind Parameters*, Solar Phys., 240, 315, http://adsabs.harvard.edu/abs/2007SoPh..240..315V.

Zhao, J., Bogart, R. S., Kosovichev, A. G., Duvall, Jr., T. L. & Hartlep, T. 2013, *Detection of Equatorward Meridional Flow and Evidence of Double-cell Meridional Circulation inside the Sun*, Astrophys. J., Lett., 774, L29, http://adsabs.harvard.edu/abs/2013ApJ...774L..29Z.

Acknowledgments

I thank
my supervisor Volker Bothmer
the comittee (Ansgar Reiners, second?)
the proofreaders
The author like to thank the proofreaders for very helpful comments and suggestions.
the 'Büro' for cozily accomodating me all the long hours

for creating and making scientific data available:
- SWS list (see Acknowledgements in Elliott2013; directly Ian Richardson)
- OMNI data (see paper)
- ACE data
- Helios data (see paper)
- Kp data
- SSN data

I acknowledge the financial support from the projects
AFFECTS: Solar wind correlation with magnetosphere
CGAUSS: Solar wind model and extrapolation
HELCATS: Minimum variance analyses of magnetic clouds
OPTIMAP: Solar wind ACE time series

This work was done within the scope of the CGAUSS project, funded by the German Aerospace Center (grant number...).
The authors thank the Helios and OMNI teams for creating and making availabe the solar wind in situ data. The Helios and the OMNI data sets were supplied by the Space Physics Data Facility at NASA's Goddard Space Flight Center.
We thank the 'referees' for /important comments and suggestions. /careful review of this paper.

facilities/persons which made available the Helios and OMNI data
"Ian Richardson and Hilary Cane for making their Interplanetary Coronal Mass Ejection list readily available"
"Joseph King and Natalia Papitashvili for creating the combined OMNI data set"
The OMNI data were downloaded from NASA's Space Physics Data Facility ...
"We thank the reviewers for the careful review of this paper"
The Authors extend their thanks to the referee for important comments and suggestions.
This work was supported by the DLR CGAUSS project
We would like to thank XX for reading drafts of this manuscript...
This work has been done in the frame of the CGAUSS project (url), funded by the DLR
We would like to thank the Helios team and NASA's SPDF for supplying the plasma and magnetic field data (url)

The results presented in this thesis rely on the *Kp* index, calculated and made available by the German Research Centre for Geosciences in Potsdam from data collected at magnetic observatories. We thank the involved national institutes, the INTERMAGNET network and ISGI (isgi.unistra.fr).

Curriculum vitae

Malte Venzmer, born 5 February 1984 in Bremerhaven, Lower Saxony, Germany, finished secondary school (Abitur) at the Gymnasium Ganderkesee in 2003. Subsequently he performed his civilian service working in a care home for disabled persons in Westerland, Sylt.

In 2004 he began to study physics at the University of Konstanz. During his studies, in summer 2008, he did an internship at the Ångström Laboratory, Uppsala University, Sweden, working in the field of materials physics. In 2010/2011 he wrote his diploma thesis in the *Radio- and X-ray astronomy* group of Dr. Jürgen Kerp at the Argelander-Institute for Astronomy, University of Bonn. There, following his diploma in physics, he continued working under a scholarship until end of 2011.

In 2012 he started as a PhD candidate in the *Solar, heliospheric and space weather research* group of Dr. Volker Bothmer at the Institute for Astrophysics, University of Göttingen. During his doctoral studies he worked as a research assistent for several national and international projects. Most of his main results are described in this very thesis.

notes

Fragen:
- references vol # fett drucken?
- references journal kursiv drucken?
- maybe style references different. like in space science reviews?
- page # oben lassen?
- A5 format?

nice phrases:
...this leads to the question wh... . The answer to this question is developed in the course of the next section.

write basics without third persons view “we”

define if using astronomical symbols...
...and use style consistently

Letzte Änderungen:
Genehmigungen für die Abb. besorgen!!
check for topic sentences!
Am Anfang der Arbeit den folgenden logischen Aufbau der Kapitel erlaeutern.
Am Anfang jedes Kapitels den folgenden logischen Aufbau der Abschnitte erlaeutern.
Beides auf Aenderungen ueberpruefen.
print figures to check look of colors
adjust figure width to textwidth...
complete pdfinfo text...

Abkuerzungen CME, usw. konsequent nutzen und beim ersten Auftauchen ausschreiben.

englische Kommasetzung beachten!
schauen, ob Kommata oder Punkte durch Semikolon ersetzt werden koennen
Pruefen, ob Ueberschriften den Inhalt des Kapitels gut beschreiben/gut zum Kapitel passen.
check if AE spelling consistently, search and replace: analyse, etc.
check for thin spaces in numbers with 5 digits and more

Header und footer fuer notes, seitenzahl, Thema und Kapitel einfuegen
check gnuplot plot text sizes and finish figures

check for changed links and update access date

sinnlosen Satz irgendwo einfügen
76 %, ACME irgendwo einfügen (ACME is good...)
comic strip aus thesis extrahieren
put movie in header or footer

create hyperref version including bibtex links
adjust link colors and remove boxes... (hyperref package options)
remove google-books links!
maybe adjust References like in Hathaway2010

LaTeX commands:
block commenting: strg+d
srtg+shift+d

$$N_{mean_0} = æe\,e\,e\,e\,e \quad e \qquad e\;\; e \tag{C.1}$$
$$N_{median_0} = \|\,|\,|\,|\,| \quad | \qquad |\;\; | \tag{C.2}$$

Provides generic commands °, °C, ‰, µ and Ω which work both in text and maths mode.

Lem & Kandel (1984), (Lem & Kandel 1984), "citep[see][page 45]Lem1984" => (see Lem & Kandel 1984, page 45)
included persons via citations: Volker Bothmer, Rainer Schwenn, Eckhard Bosman, Russel Howard, Manuela Temmer, Angelos Vourlidas, Craig DeForest, Tim Howard, Rodney Viereck

Style rules:
the Sun's/solar rotation period
Earth's/terrestrial
the Sun, sunspots; near-Sun measurements, near-relativistic electrons, in situ measurements without hyphen
64 s data; but 64-second data
Therefore, a comma is set after certain adverbs at the beginning of a sentence.
lognormal or log-normal, not log normal

A&A style:
Italics should never be used for units
italics should be avoided for the following: mathematical signs such as "d" (total differential), "e" (base of natural logarithm), "i" (imaginary unit), "pi"
Physical constants such as the speed of light, the Boltzmann constant, the Hubble constant and the solar mass are also set in regular italics.

$$\mathrm{e}^x = 10\,\mathrm{km\,s^{-1}} \tag{C.3}$$

$$\mathrm{e}^x = 10\,\mathrm{km{\cdot}s^{-1}} \tag{C.4}$$

$$\mathrm{e}^x = 10\,\mathrm{km/s} \tag{C.5}$$

$$k_\mathrm{B} \tag{C.6}$$

Sample input: 20 000 km, 1 000 000 s, HD 174 638 1950–1985, p. 11–21, this – written on a computer – is now printed, this—written on a computer—is now printed, signal-to-noise ratio, early-type, metal-poor, non-relativistic −30 K, −5 °C Dr. h.c. Rockefeller-Smith and Prof. Dr. Mallory

Nützliche Beispiele für LaTeX-Kommandos:
Autobahn
X-Ray
X-Ray
Dr. Huber
100 000 V
100 000 V
The food—which was delicious—reminded me of home.
Red, white, and blue—these are the colors of the flag.

$U = 20\,000\,\mathrm{V}$
solar radius: $R_\odot = 696\,000$ km

10 °C
10 °C
10 °C
Ein Winkel von 10°.

$$\frac{T_\mathrm{D}}{[\mathrm{K}]} = 21,8 \cdot \left(\frac{\Delta v^\mathrm{LMC}_\mathrm{FWHM}}{[\mathrm{km\,s^{-1}}]}\right)^2 \tag{C.7}$$

$$\frac{T_\mathrm{D}}{[\mathrm{K}]} = 21,8 \cdot \left(\frac{\Delta v^{\scriptscriptstyle\mathrm{LMC}}_{\scriptscriptstyle\mathrm{FWHM}}}{[\mathrm{km\,s^{-1}}]}\right)^2 \tag{C.8}$$

$$k = 3.56\,\mathrm{e{-}6} \tag{C.9}$$

$$k = 3.56 \cdot 10^{-6} \tag{C.10}$$

$$k = 3.56 \times 10^{-6} \tag{C.11}$$

1. CM LMC Longitude

drei CM LMC Latitude

Volume in $(^\circ)^2 \mathrm{m\,s^{-1}}$. Summe aller Voxel des Objektes.

Volume in $(^\circ)^2 \mathrm{m\,s^{-1}}$. Summe aller Voxel des Objektes.

- Volume

sdgffs CM GSR Velocity

label

asdf Volume

drei CM LMC Latitude

[1] oder [2]

$$a^2 + b^2 = c^2 \tag{C.12}$$

Formel zitieren: (Siehe Formel C.12, Formel (C.12), Seite 100)

package siunitx:
20.5×10^{-3} kg
20.5×10^{-3} kg
20.5×10^{-3} kg

width defines the width of the resulting box as seen from the outside (This means it can be $\boxed{\text{smaller}}$ than the material inside the box. You can even set the width to 0pt so that the text inside the box will be typeset without influencing the surrounding boxes). Besides the length expressions, you can also u

semi-log plots:
log-lin: logarithmic scale on the y-axis, and a linear scale on the x-axis
lin-log: logarithmic scale on the x-axis, and a linear scale on the y-axis
the naming is output-input (y-x), the opposite order from (x, y)

my common language errors:
hyphen for adjectives
solar wind
solar-wind parameters
high-value tail

serial comma (it is an american thing and optional)
a, b, c and d.
a, b, c, and d.

comma if object is at beginning of sentence
In the case of A, B is C.
In order to A, B can C.

BE vs AE
catalogue

[1]All listed websites were existent on 2008-09-15.
[2]All listed websites were existent on 2008-09-15.

catalog

grey
gray